

# **InP Segmented Mach-Zehnder Modulators with Advanced EO Functionalities**

vorgelegt von

M.Sc. in Nanotechnology for ICT Engineering  
Alessandro Aimone  
geboren in Turin, Italien

Von der Fakultät II - Mathematik und Naturwissenschaften  
der Technischen Universität Berlin  
zur Erlangung des akademischen Grades

Doktor der Ingenieurwissenschaften  
- Dr.-Ing. -

genehmigte Dissertation

Promotionsausschuss:

- Vorsitzender: Prof. Dr. M. Lehmann  
1. Gutachter: Prof. Dr. rer. nat. M. Schell  
2. Gutachter: Prof. Dr. A. Bogoni (Scuola Superiore Sant'Anna, Pisa, Italien)

Tag der wissenschaftlichen Aussprache: 12. September 2016

Berlin 2016



---

# Zusammenfassung

Thema dieser Arbeit sind segmentierte Indium Phosphid (InP) Mach-Zehnder Modulatoren (SEMZMs). Diese elektro-optischen Komponenten werden verwendet um Digital-Analog-Wandler (DACs) und digitale Signalverarbeitung zu implementieren, ohne jedoch die herkömmlichen dafür vorgesehenen platzraubenden elektronischen Komponenten mit hoher Leistungsaufnahme zu verwenden. Der hier vorgeschlagene und umgesetzte Ansatz adressiert hauptsächlich die Thematik des kleineren Platz- und Leistungsbedarf. Von den zu ersetzenden Einsatzmöglichkeiten des DAC werden hier drei näher untersucht: Frequenzentzerrung (frequency equalization), Nyquist spektrale Profilformung (spectral shaping) und Digital-zu-Analog-Konversion.

Als Erstes wird ein segmentierter Modulator mit Bandbreitenerhöhung präsentiert. Diese wird verwendet um eine möglichst hohe elektro-optische Übertragungsbandbreite zu erzielen bei gleichzeitiger Verwendung von elektrischen Komponenten mit niedriger Bandbreite. Konkret wurde ein Transmitter mit Bandbreite von 30 GHz realisiert und für eine fehlerfreie Übertragung bei 56 Gbd OOK genutzt, obwohl die elektrischen Komponenten maximal 22 GHz Bandbreite besitzen, dies entspricht einer Bandbreitenerhöhung von 36%. Die Vergleichsmessung unter Verwendung eines Lithiumniobat Modulators statt eines SEMZM zeigt die Vorteile des SEMZM bezüglich der Bit-Fehler-Rate (BER).

Als Zweites wird der SEMZM verwendet, um die spektrale Bandbreite eines modulierten 40 Gbd 4-Niveau Signals zu halbieren. Dank der spektral-formenden Eigenschaften des SEMZM können zwei Dual-Polarisations modulierte Subträger, mit einem Abstand von nur 50 GHz, fehlerfrei über 80 km Standard Einmoden-Faser (SSMF) übertragen werden. Mit einer genutzten spektralen Bandbreite von insgesamt 100 GHz beträgt die spektrale Effizienz 3,2 b/s/Hz. BER Messungen zeigen keinen Einfluss der beiden eng beieinanderliegenden Subträger aufeinander.

Im letzten Abschnitt der Arbeit werden segmentierte Modulatoren für die optische digital-analog Konversion betrachtet. Zwei verschiedene InP SEMZM Bauelemente wurden entwickelt, für den Einsatz mit BiCMOS oder CMOS Elektronik. Der SEMZM in Intensität-Quadratur-Konfiguration mit BiCMOS Treiber zeigt eine fehlerfreie Übertragung über 80 km SSMF mit einem Dual-Polarisation 64-Symbol Quadratur-Amplituden modulierten Signal bei einer Symbolrate von 32 Gbd. Diese Symbolrate zusammen mit einem Leistungsverbrauch von nur 1.5 W ergibt eine totale Datenrate von 384 Gb/s und eine Energie pro Bit von 7,8 pJ/b. Unter Verwendung des CMOS Treibers zeigte der entwickelte SEMZM fehlerfrei transmittierte amplituden- und phasenmodulierte Signale bei 15 Gbd.



---

# Abstract

This work covers indium phosphide (InP) segmented Mach-Zehnder modulators (SEMZMs). These electro-optical components are proposed as a means to implement digital-to-analog converters (DACs) and digital signal processing functionalities without the need of bulky and power-hungry dedicated electrical components. The proposed approach shows its advantage in terms of reduced area and power consumption. Among the different DAC-enabled features, bandwidth enhancement by frequency equalization, Nyquist-space spectral shaping, and optical-DAC are identified and discussed.

First, a segmented modulator with bandwidth enhancement capability is presented. When the modulator is driven by electronics of 22 GHz bandwidth, the electro-optical bandwidth of the complete transmitter is measured to be 30 GHz. Hence, a bandwidth broadening of 36 % is measured. With this setup, error-free transmission of a 56 GBd on-off keying signal is demonstrated. The experiment is repeated by replacing the SEMZM with a lithium niobate modulator driven by the same electronics. Bit error ratio (BER) measurements show the SEMZM performs better, both in presence of chromatic dispersion and in presence of noise.

Afterwards, a Nyquist-space spectral shaping SEMZM is used to halve the occupied bandwidth of a 40 GBd 4-level modulated signal. Thanks to this shaping, two dual-polarization modulated subcarriers, spaced at only 50 GHz, are transmitted error-free over 80 km of standard single mode fiber (SSMF). With an overall occupied bandwidth of 100 GHz, the overall measured gross spectral efficiency is 3.2 b/s/Hz. BER measurements show no influence of the closely spaced adjacent subcarrier.

Lastly, optical digital-to-analog conversion by segmented modulators is demonstrated. Two different InP devices are developed to be driven by either BiCMOS or CMOS dedicated electronics. For the first time, error-free transmission of a 32 GBd dual-polarization 64-symbol quadrature amplitude modulated (64-QAM) signal over 80 km of SSMF without the use of a DAC is demonstrated. The speed of 32 GBd and the low power consumption of 1.5 W translate to a total gross data rate of 384 Gb/s and energy per bit of 7.8 pJ/b. Alternatively, using a CMOS driver, the developed segmented modulator is shown to transmit error-free a 15 GBd 4-ASK-2-PSK signal with a power consumption of 1 W and corresponding energy per bit of 22.2 pJ/b.



---

# Table of Contents

1.	Introduction .....	1
1.1.	Motivation .....	1
1.2.	Methodology.....	3
1.3.	Thesis Organization .....	3
2.	InP MZM Fundamentals.....	5
2.1.	General Aspects of Mach-Zehnder Modulators .....	5
2.2.	IQ-MZ Modulator .....	11
2.3.	Segmented Mach-Zehnder Modulator .....	12
3.	Resonant SEMZM.....	17
3.1.	Introduction .....	17
3.2.	Resonant SEMZM Design.....	22
3.3.	Bandwidth Enhancement by Frequency Equalization.....	44
3.4.	Nyquist-space Spectral Shaping.....	48
4.	SEMZM for Optical-DAC .....	57
4.1.	Introduction .....	57
4.1.	SEMZM driven by BiCMOS IC.....	60
4.2.	SEMZM driven by CMOS IC .....	63
4.3.	Segmented Mach-Zehnder Linearization .....	68
5.	Discussion and Conclusions .....	73
5.1.	Outlook .....	74
6.	Acknowledgments .....	I

## Table of Contents

---

7. List of Abbreviations.....	III
8. List of Symbols .....	V
9. Published Work.....	VII
10. Bibliography .....	IX

# 1. Introduction

## 1.1. Motivation

Data transmission has profoundly transformed our world in the last few decades. The creation of an interconnected network has revolutionized millions of people's lives in many respects. The author himself, being born in the late 80s, remembers how different it was to live before the invention of the internet. This extraordinary revolution did not just appear all of a sudden, but has instead been supported over the years by a dramatic increase in connection speed: the times when the download of a few MB large song would take all night are long gone. This swift speed growth has been enabled since the late 90s by the rise of dedicated technologies, such as Digital Subscriber Line (DSL), which quickly attracted millions of customers [1]. DSL, today employed by hundreds of millions of users connected by copper wires, is supported by advanced information transmission techniques that aim to increase the transmitted and received data rate. Thanks to these, copper wire DSL-based communication links have been recently shown to be capable of speeds in the Gb/s range [2]. However, the need for higher throughputs, either for clients or for the backbones of the network, found its sweet spot in optical fiber communication. The use of light pulses in place of electrical ones and the emergence of technologies in which the phase and the amplitude of the transmitted signal are simultaneously modulated, opened the way to today's networks. Data-hungry habits such as the streaming of high-resolution videos and cloud services have thus become possible.

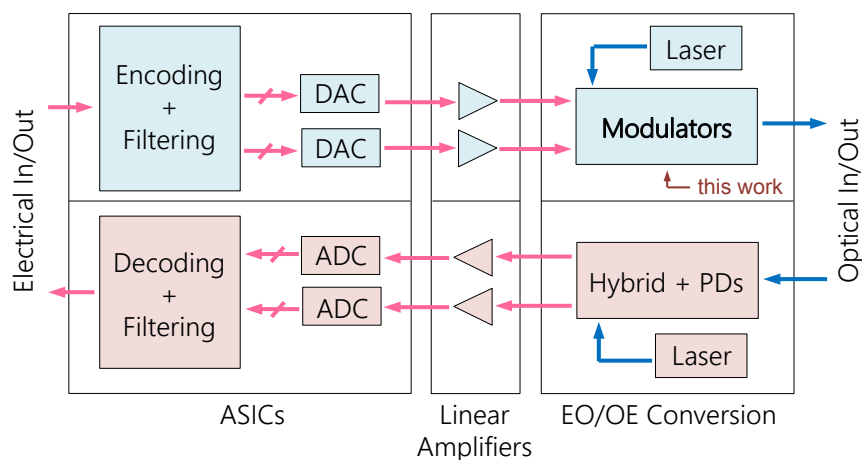


**Figure 1-1:** Coherent transceiver block diagram. Magenta arrows represent electrical signals and blue arrows optical signals. Blue blocks constitute the transmitter path and red ones the receiver one.

Optical communications did not, however, completely replace electrical links, but rather complemented them in those areas where optics offers particular advantages, e.g. in long distance scenarios. To switch from the electrical to the optical domain, and vice versa, new components are required. These components, namely electro-optical (EO) modulators and photodetectors (PD), are to be integrated into optical transceivers, which contain all the hardware required to transmit and receive the data (Figure 1-1). The transmitting part of an optical coherent transceiver starts with an application specific integrated circuit (ASIC) that encodes and filters the incoming data according to the foreseen application. This binary data is converted into an analog signal by digital-to-analog converters (DACs). The analog signals are afterwards amplified to the desired level by RF linear drivers and fed into the EO modulators, which are responsible for the conversion to the optical domain. The receiving part follows a similar topology, except the signal enters this time from the optical side and undergoes opto-electrical (OE) conversion by high-speed PDs (lower half of Figure 1-1). The analog electrical signals are once more amplified and converted into the digital domain by analog-to-digital converters (ADCs). Lastly, the signals are decoded and the data is ready to be processed.

This work focuses on *EO modulators* and their surrounding components in an optical transmitter. EO modulators are powerful components that are widely employed in optical telecommunication networks all over the world. Applications of EO modulators range from short range transmission to submarine transcontinental links. Tens of years of research made modulators increasingly reliable and efficient devices, to the point that they now represent only a small portion of the transceiver space and power consumption. Modulators are a key component in data transmitters and have a strong influence on the overall link quality. With the arrival of the digital era, modulators have been aided by DACs and digital signal processing (DSP) algorithms, enabling a performance boost impossible in the analog domain [3], [4], [5]. DACs and DSP, first introduced into optical transmission in 2005 [6], are today widely employed in long distance communication links where the available channel bandwidth is limited and can be better exploited thanks to their usage [7]. Additionally, such components allow for compensation of most distortions that the light signal undergoes while traveling through the data channel. Due to their capabilities, these components represent an irreplaceable part of long haul links. Unfortunately, their size and energy consumption is non-negligible, making these solutions inappropriate for those scenarios where these parameters are limiting factors [7], [8]. The integrated circuit (IC) power consumption required for signal processing contributes significantly to the overall energy requirements in today's transceivers, with this portion expected to grow beyond the 50 % of the total in next generation devices [9]. Because of these reasons, ways to reduce DACs requirements are of great interest.

The target of the present work is the development of a novel kind of EO modulator, which will relax the demands on the related electrical components, in particular on the DAC performance. Specific attention will also be given to the question whether these EO modulators could eventually operate without the need of any DAC at all. The focus of the thesis will be on Indium Phosphide (InP)-based Mach-Zehnder Modulators (MZMs) and, in particular, segmented Mach-Zehnder modulators (SEMZM). These have recently been shown to enable additional optical functionalities and simultaneously relax intrinsic design trade-offs of traditional MZMs. SEMZMs of a specific kind, the resonant SEMZM, are proposed as a means to address three specific functions: i) bandwidth enhancement, ii) Nyquist-space pulse shaping, and iii) optical-DAC. Currently, these are accomplished using electronic DACs, and optical SEMZM-based solutions are expected to bring advantages in terms of lower costs, smaller footprints and reduced energy consumption. For each of these applications, theoretical background is provided and a real-world scenario is found.

## 1.2. Methodology

In the following chapters, a number of results, both simulated and measured, will be presented and discussed. The work starts with the development of a valid SEMZM model. To this goal, analytical and electrical analysis of the device is performed with the help of different computer-aided design (CAD) tools. The analytical modeling is performed with Mathworks MATLAB, which is also employed for support routine scripts. 3D electromagnetic simulations are carried out with Ansys HFSS and the high-frequency circuit ones with Keysight Advanced Design System. Photon Design's FIMMWAVE is the tool used for the optical level investigations.

The various measurement results presented in this work are obtained with different setups. For this reason, a dedicated paragraph is reported each required time. The model outputs are compared with the measured ones at several steps along the thesis, in order to continuously validate the former as prediction tool.

## 1.3. Thesis Organization

After this introduction, this work is organized as follows. Chapter 2 provides the Mach-Zehnder modulators theoretical background, which is necessary for the understanding of the rest of the thesis. The chapter starts with an overview of the basic working principles of the MZM and the derivation of its transfer function. It then introduces IQ MZ-modulators (IQ-MZM) and their application. The second part of the chapter focuses on the segmented MZM. The differences between this component and its travelling-wave electrode (TWE) modulator counterpart are discussed. Advantages and drawbacks of the segmented

topology are highlighted. This chapter includes an up to date review of the state of the art SEMZMs.

Chapter 3 addresses the design and development of the resonant segmented MZM. This chapter opens with the introduction of bandwidth enhancement by frequency equalization and Nyquist-space spectral shaping. It continues with the modeling of a modulator's segment, its frequency response, and the identification of its main design parameters. A study on the variations of these parameters and their effect on the resonators properties is performed. Electrical and optical level simulation tools are introduced and employed in order to study the segmented structures. The obtained results are presented and discussed. Chapter 3 continues with the measurement of the fabricated structures. Insight on both DC and RF characterization of these components is provided. The measurement setups are described and the results are compared with what was previously simulated. The performance of the resonant SEMZMs is evaluated in multiple large-signal setups, which emulate the application scenarios for which they are developed.

Chapter 4 focuses on the use of a non-resonant SEMZM as an optical digital-to-analog converter. After an introduction of this functionality, the design process of the SEMZM for optical-DAC is presented. This chapter presents the work developed with two different approaches. First a BiCMOS then a CMOS driver is employed for the SEMZM drive. The measurements results of the fabricated structures and a conclusion on their optical-DAC capability is provided. In addition, the development of a high-yield hybrid integration process for large capacity transmitters is presented. Chapter 4 closes with a section on how to linearize the modulator transfer function.

This work ends with Chapter 5. Here the results are summarized and a discussion over the performance of the developed SEMZMs and their capability to relax and finally replace electrical DACs in current and future optical communication networks is reported.

---

## 2. InP MZM Fundamentals

### 2.1. General Aspects of Mach-Zehnder Modulators

Multiple techniques have been developed over the years in order to encode information into the amplitude or phase of an optical signal. Among the topologies that are broadly implemented today, it is possible to find directly modulated lasers (DMLs), electro-absorption modulated lasers (EMLs), ring resonators, and interferometer-based Mach-Zehnder modulators (Figure 2-1). The choice of either modulation technology depends on multiple factors, starting with the requirements derived from the application scenario. DMLs and EMLs represent valid EO components to be employed for light communications. However, DMLs and EMLs are used for amplitude modulation only and are thus no suitable choice when phase modulation is desired. Ring modulators exhibit advantages such as a very small footprint, but are very sensitive to temperature and can be employed only at a specific optical wavelength. Mach-Zehnder modulators are a widely employed class of EO converters that boast a variety of advantages, which make them the preferable choice in a range of applications. Simultaneous modulation of both the phase and the amplitude of a light beam over the whole C-, L- or O-band is possible with MZMs. MZMs have been developed and have become commercially available based upon different technologies. Small, chirp-free modulators with concurrent low optical losses and low driving voltages are achievable with III-V based MZMs. In particular, InP modulators exhibit a smaller footprint and a lower driving voltage with respect to their polymer and LiNbO<sub>3</sub> counterparts [10].

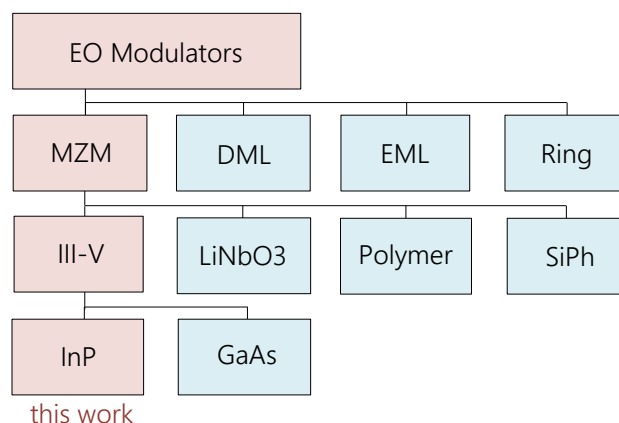


**Figure 2-1:** Overview of EO modulators' solutions and materials. This work focuses on InP Mach-Zehnder modulators, in particular its segmented version.

In contrast with these mature technologies, today's most emerging one is Silicon Photonics (SiPh) [11]. The large scientific community interest on SiPh originates from its expected lower chip costs and from its compatibility with the IC CMOS processes. However, despite great efforts, SiPh is currently encountering its fundamental limits, which prevent it from achieving simultaneous low driving voltage, low optical losses and large EO bandwidth [12]. On the other hand, InP outcompetes today's state of the art market [13] and research [14] SiPh in all these fields and represents therefore still a valid candidate for future communication links. Lastly, in opposition to SiPh, III-V technologies enable the possibility of integration with the laser source with consequent reduction of size and coupling losses.

In InP-based MZMs, light modulation is obtained by means of various EO effects. Pockels and Kerr effects play a role together with quantum phenomena, e.g. the quantum-confined Stark effect. The full description of the physics that takes place in these devices is beyond the scope of this thesis, but can be found in literature [15], [16], [17]. In the following sections of this work, a component-level understanding of InP MZMs is provided.

A standard InP MZ modulator consists of an optical interferometer in which the phase difference between the two arms is controlled by an external electrical signal (Figure 2-2) [18, pp. 173-203]. In more detail, a beam of light is coupled into the input waveguide of the modulator. Here, a spot-size converter (SSC) can be implemented in order to ease the optical coupling by increasing the mode field diameter of the chip waveguide. The coupled light is then divided into equal parts and routed into two waveguides with the use of a splitter: either a Y-junction or a multi-mode interferometer (MMI) [19]. These two waveguides constitute the interferometer arms. The two beams of light travel through the so-called active areas of the modulator, where the interaction between the electrical signal and the optical wave takes place.

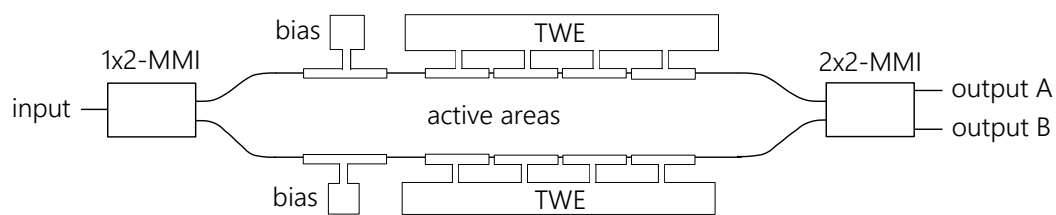


**Figure 2-2:** Mach-Zehnder modulator's block diagram. The input waveguide is split in two by means of an input MMI. The light beams travel through the active areas and are then recombined at the output MMI, where interference takes place and amplitude modulation occurs.

At the end of the active region, the light is recombined by a 2x2 MMI. In this MMI, the two incoming beams of light interfere with each other and, depending on their relative phase difference, the resulting optical signal is routed to a specific output or split between the two. Looking at a single output, the light is thus switched on and off and amplitude

modulation is therefore obtained. One of the MMI outputs is taken as the modulator's output and the other is usually sent to a diode for monitoring purpose. An additional SSC can be inserted at the output facet to lower coupling losses. The core of high speed MZM can be inserted at the output facet to lower coupling losses. The core of high speed MZM consists of multiple isolated active sections. One of these sections can be dedicated to the selection of the MZM working point and connected to a DC voltage or current. The others are instead driven with the RF electrical input signal containing the data to be transmitted. In these regions, the electro-optic interaction takes place, i.e. the travelling optical wave and the electrical field induced by the external electrical stimulus overlap. It is here that the phase difference between the two MZM arms is generated. The active InP waveguides are deeply etched and structured as vertical pin junctions (Figure 2-3). The light beam travels along the intrinsic region of the junction, where a multiple quantum well (MQW) core is located. The waveguide structure is specifically designed to best improve the EO effects' efficiency and maximize the overlap between the electric and the optical fields. The two modulator's arms share a common n-doped InP layer that is employed to provide proper direct-current (DC) biasing of the two junctions and set them in reverse operation [20]. The radio frequency (RF) signal is provided through the p-contacts, which are metalized on top. The different active areas of the waveguides are electrically connected together through a common conductive line, the so-called Traveling-Wave Electrode. TWE-MZMs are the current standard when it comes to semiconductor-based MZMs and are based on concepts developed in the early 70s from the work of White [21]. The TWE forms a transmission line that distributes the driving voltage to the different active areas of the modulator. The modulation data is applied in the form of RF voltage at the TWE inputs. The electrical wave moves along the TWE alongside the optical wave, which travels in the parallel InP waveguide. As the optical wave moves from one MZM active area to the next, the electrical wave is required to travel with the same speed to provide a constant electric field and satisfy the so-called velocity match condition. This condition, which is met by means of proper TWE and electrode design, is critical for the achievement of high EO bandwidth, i.e. high modulation speed [10].

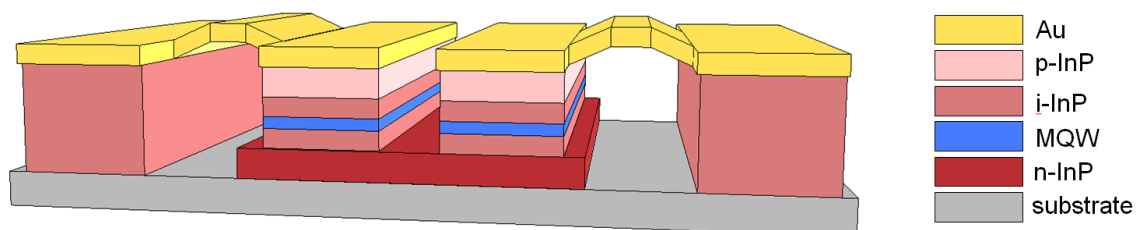


**Figure 2-3:** 3D cut of a TWE-MZM active area. The InP optical waveguides constitute a pin junction in the vertical direction. MQWs are grown in the middle of the intrinsic region to enhance the quantum EO effects.

The field transversally applied on the InP waveguides induces a change of the material refractive index. This change is proportional to the field amplitude and therefore to the applied voltage  $V$  at the TWE input. The relationship between this voltage and the correspondent phase shift  $\varphi$  after an active area of unitary length is expressed by the empirical relationship [22]

$$\varphi = p_A V + p_B V^2 \quad , \quad (2-1)$$

where  $p_A$  and  $p_B$  are parameters that depend on the specific design and on the operating condition. For small amplitudes of the applied voltage  $V$ , the phase dependency can be approximated as linear, due to the negligible influence of the quadratic term. This approximation introduces an error that is negligible for the purpose of this work and is therefore utilized in the following chapters. The induced phase difference  $\Delta\varphi$  can be expressed as

$$\Delta\varphi \cong \pi \cdot \frac{V}{V_\pi} \cdot \frac{L}{L_a} \quad (2-2)$$

as a function of the active area length  $L_a$  and the switching voltage  $V_\pi$ . This is the voltage that, when applied on a single interferometer arm, induces a phase shift of  $\pi$ , i.e. switches the MZM output light on or off. Both the switching voltage  $V_\pi$  and the active length over which this voltage is applied  $L_a$  are fundamental design parameters of the MZM and are extensively discussed in the rest of this thesis. It is possible to derive the overall MZM transfer function, that is to say the field  $E_{out,i}$  at the output  $i$  of the device depending on the field fed at its input  $E_{in}$ , as a function of the induced phase shift. For a 2-output modulator, a scattering matrix can be associated with each of the building blocks of the diagram in Figure 2-2:

$$\begin{pmatrix} E_{out,A} \\ E_{out,B} \end{pmatrix} = \underbrace{\frac{1}{\sqrt{2}} \begin{pmatrix} 1 & -j \\ -j & 1 \end{pmatrix}}_{2 \times 2\text{-MMI}} \cdot \underbrace{\begin{pmatrix} e^{j\varphi_1} & 0 \\ 0 & e^{j\varphi_2} \end{pmatrix}}_{\text{Active Area}} \cdot \underbrace{\frac{1}{\sqrt{2}} \begin{pmatrix} 1 \\ 1 \end{pmatrix}}_{1 \times 2\text{-MMI}} \cdot E_{in} \quad (2-3)$$

where  $\varphi_1$  and  $\varphi_2$  are the phase shifts induced in the two interferometer arms. The two phase-shifts are expressed as function of their sum and difference, namely  $\varphi_1 = \varphi_0 + \Delta\varphi/2$  and  $\varphi_2 = \varphi_0 - \Delta\varphi/2$ , with  $\varphi_0$  being the phase shift when no voltage is applied. These relationships are valid as long as the phase shift dependency on the voltage is considered linear, simplifying equation (2-1). The whole modulator's transfer function  $H_{MZM}$  at the output A is thus in this approximation written as a function of the voltages  $V_1$  and  $V_2$  applied on the different arms:

$$H_{\text{MZM}}(V_1, V_2) = \cos\left(\frac{\pi}{2V_\pi}(V_1 - V_2)\right) e^{j\frac{\pi}{2V_\pi}(V_1 + V_2)} . \quad (2-4)$$

The cosine term of this expression is linked to the amplitude of the output field and is a function of the difference of the applied voltages. The exponential term is instead associated to the output field's phase, thus to the chirp of the modulator [23]. Chirp-free modulation is often required in order not to degrade the transmission performance. For this reason MZMs are commonly driven in the so-called push-pull configuration [20], [24]. When  $V_1$  equals  $-V_2$ , the phase of the optical output is constant. However, when other driving schemes are chosen or a purely differential drive is not practically achievable, chirp can become a limiting factor. This is particularly true when complex modulation formats are transmitted. Chirp becomes critical in the case of simultaneous modulation of amplitude and phase, discussed in more detail in the following section. It is common to find equation (2-4) reported as its squared absolute value, because PDs measure the field intensity  $I_{\text{out}}$  rather than its amplitude and phase:

$$I_{\text{out}}/I_{\text{in}} = \cos^2\left(\frac{\pi}{2V_\pi}(V_1 - V_2)\right) . \quad (2-5)$$

The power transfer function of the MZM does not contain information about the field's phase. Although the squared cosine provides cyclic intensity with sweeping voltage, the rising and falling regions of the characteristic are associated with a different signal phase. This relative phase change, equal to  $\pi$ , occurs at the 'on' and 'off' states of the MZM and arises from the change of sign of the cosine term in equation (2-4). The MZM power characteristic is non-linear (Figure 2-4). Consequently, the behavior of the modulator is dependent on the selected working point, the appropriate choice of which can be different in accordance with the desired modulation format [24]. For amplitude modulation, the MZM is typically biased in the middle of the linear region, the 3-dB point, and driven with an electrical signal of limited amplitude. This ensures that the non-linear extremities of the transfer function are not reached and no distortion of the modulated signal is introduced. A deeper discussion on the MZM transfer function and ways to linearize it is the topic of chapter 4.3.

The modulator's performance is quantified with a set of parameters that have been historically employed. Together with the switching voltage  $V_\pi$ , the Insertion Loss (IL) and Extinction Ratio (ER) are commonly reported in literature. The IL of an MZM is defined as the ratio between the maximum optical power guided to the output  $P_{\text{max}}$  and the optical power fed at the input  $P_{\text{in}}$ . It is a measure of how much light is lost within the chip and at the facets. The ER instead expresses the modulation depth of the device and is defined as  $P_{\text{max}}/P_{\text{min}}$ , where  $P_{\text{min}}$  is the optical power level seen at the output when the MZM is in the 'off' state.

A quantity frequently used for the comparison of different designs is the switching voltage-length product. This constitutes an intuitive way to express the modulation efficiency, i.e. how much phase shift can be induced over a given length with a specific voltage. It is expressed as

$$(V_{\pi} \cdot L_a) = k \quad (2-6)$$

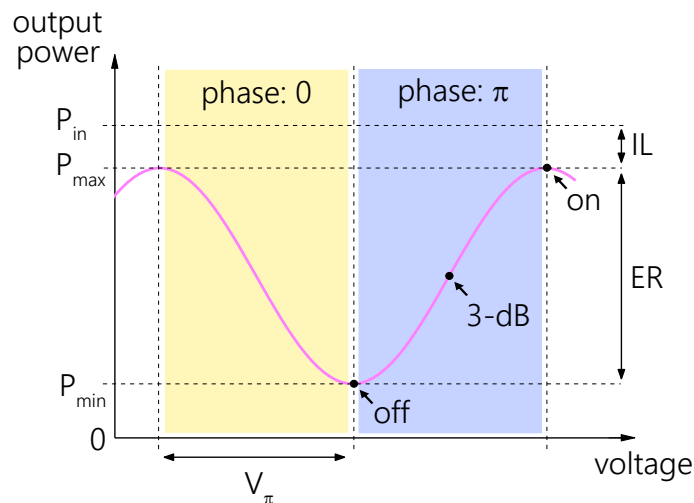


**Figure 2-4:** MZM power transfer function and most common evaluation parameters. Depending on the selected modulation format, the modulator is biased in either the 3-dB or the off state.

This voltage-length product depends on several design parameters including those that directly affect the overlap between the optical and the electrical mode, e.g. the intrinsic region thickness and the junction materials. Its simplicity and the large number of design variables it includes are the reasons why this macroscopic quantity is widely reported in literature [20], [25], [26]. According to formula (2-6), an efficient MZM requires a shorter active length than a less efficient one, for the same switching voltage. Similarly, when the active length has already been fixed, a more efficient modulator will require a lower drive voltage to achieve full modulation depth. Recently, another figure of merit has been proposed as a replacement for the  $(V_{\pi} \cdot L_a)$  product. This new quantity, defined as the multiplication of  $(V_{\pi} \cdot L_a)$  by the optical propagation losses of the active MZM regions, provides a clearer understanding of how the modulator choice affects the overall communication system [27]. In this work, both the modulation efficiency and a  $(V_{\pi} \cdot IL)$  product are provided for the characterized devices. Compared to the one including the propagation losses, this figure of merit, calculated at best biasing conditions, represents a more straightforward choice as it includes only parameters that directly express the performance of the modulator.

## 2.2. IQ-MZ Modulator

A single Mach-Zehnder modulator can be used to modulate the amplitude of optical pulses. In addition, phase values of zero and  $\pi$  can be attributed to this output signal, as previously described. The most straightforward modulation scheme that can be achieved with a single MZM is amplitude-shift keying (ASK), based on amplitude modulation only. On-off keying (OOK) is the simplest format of the ASK family: it encodes a '1' when light is transmitted at the output of the MZM and a '0' when no light is present. Similarly, phase-shift keying (PSK) is achieved if only the phase of the optical signal is modulated. When both amplitude and phase modulation is realized, formats such as M-ASK-N-PSK are obtained, where M and N are the number of transmitted amplitude and phase levels. For a single MZM, N can only take values of 1 and 2, depending on the drive condition. A single MZM can also be employed to transmit multiple amplitude levels, each of them encoding more than a single bit. This result in an increase of data throughput for the same occupied bandwidth. These modulation schemes are called pulse-amplitude modulation (PAM) and are commonly implemented with either 4 (4-PAM) or 8 (8-PAM) different levels. The limit to the number of levels that can be successfully transmitted in PAM signals comes from the reduced spacing between them, which increases the receiver sensitivity requirements.

Schemes that are more complex require for the concurrent modulation of multi-level amplitude and multi-level phase. For this goal, a MZ modulator can be aided by phase modulators in a set of different topologies. Among the several possible choices, the employment of the so-called IQ-modulator benefits from high versatility and reduced electrical-level complexity [28, pp. 42-47]. An IQ-modulator is composed of two parallel Mach-Zehnder modulators sharing a single optical input and a single optical output (Figure 2-5).

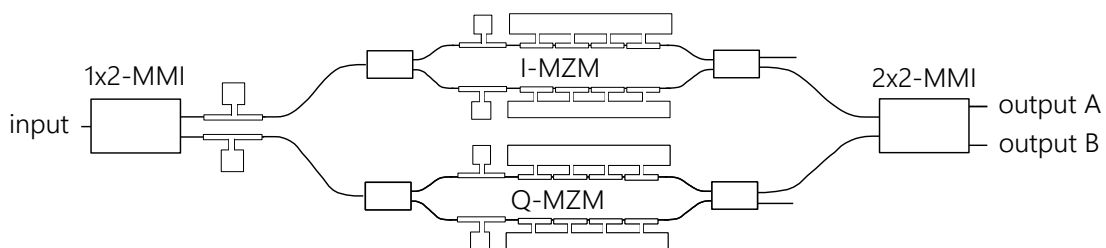


**Figure 2-5:** Schematic of an IQ Mach-Zehnder modulator. Two children modulators are nested in the parent IQ-MZM. Additional MMIs are inserted at the input and at the output of the device to route the light in the I- and Q-MZMs and ensure their orthogonality.

The two modulators are referred to as the children, or as the in-phase (I-) and quadrature (Q-) MZMs. The IQ-modulator ensemble is instead referred to as the parent. Before and after each of the children, additional MMIs are inserted to serve as splitters and

couplers, respectively. The input MMI splits the signal in two halves and routes them into the I- and the Q-MZM. These two signals are then recombined at the output 2x2-MMI into an IQ signal. In addition, this MMI introduces a phase shift of  $\pi/2$  for one of its inputs and thus ensures orthogonality between the two children signals. Residual undesired phase differences between the two children signals are compensated thanks to an additional biasing section inserted at parent level. The IQ signal transports information in both its amplitude and phase without requiring additional bandwidth, effectively increasing the spectral efficiency [28, pp. 18-21]. The information conveyed in this signal can be represented on the complex plane originating the constellation diagram. In this diagram, the information contained in the I- and the Q-signals is combined and gives rise to a set of points that represent the transmitted symbols. Higher-order modulation schemes are associated to diagrams that are more crowded with a larger amount of information conveyed in each constellation point, i.e. the number of bits per symbol. The constellation for four-symbol quadrature-amplitude modulation (4-QAM) data is constructed starting from the two children 1-ASK-2-PSK signals (Figure 2-6). The same procedure is performed for any other IQ modulated signal: if the children MZMs outputs are both M-ASK-2-PSK signals, the IQ output is  $M^2$ -QAM modulated.

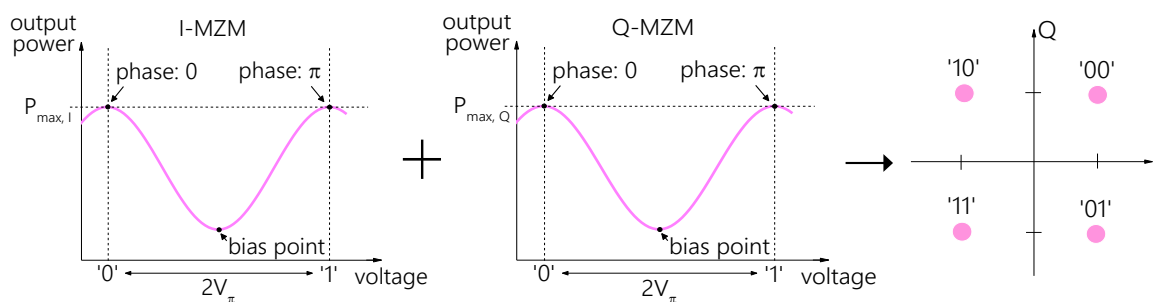


**Figure 2-6:** Construction of a 4-QAM modulated signal with an IQ-MZM. Two electrical binary signals drive the I- and Q-MZMs in 1-ASK-2-PSK mode. The resulting constellation symbols transmit two bits each. 4-QAM modulation ideally requires children MZMs to be driven with  $2V_{\pi}$ .

### 2.3. Segmented Mach-Zehnder Modulator

Traveling-wave MZ modulators have several practical shortcomings that are strictly related to their electrode design. The velocity match condition translates into a limitation to the portion of the interferometer arms that can be metallized, i.e. the active areas. The demand for MZMs with lower switching voltage drives the need for longer modulators, according to equation (2-6). However, due to their increased length, a precise match between the velocities of the electrical and optical waves becomes more critical. In addition, high baud rate operation makes the pattern bit duration comparable with residual time

mismatch and quickly degrades the modulated signal quality. Lastly, high frequency signals suffer from larger losses while travelling through longer TWEs. These issues together result in a limit on the maximum achievable operating frequency, i.e. the EO bandwidth of the modulator. The inverse relationship between the TWE length and its bandwidth, together with the direct proportionality between the TWE length and the modulator's switching voltage, gives rise to the well-known trade-off between these fundamental quantities [29].

A way to overcome the voltage-bandwidth trade-off is a different arrangement of the modulator's electrodes. Segmented-electrode Mach-Zehnder Modulators have been recently proposed as a way to address this issue. These modulators and their applications have been first discussed in 1980 by Papuchon [30], but just recently re-discovered with the first high-speed working devices presented in 2011 [31]. In a segmented MZ modulator, the different active sections of the TWE are detached and made electrically independent from each other (Figure 2-7). Each of the segments is provided with dedicated input pads, all on one side of the SEMZM, where the electrical voltage is connected. Small gold bridges are used in order to reach both SEMZM arms from the pads, thus easing electrical routing. The optical level design of the modulators, both single or in an IQ configuration, stays the same.

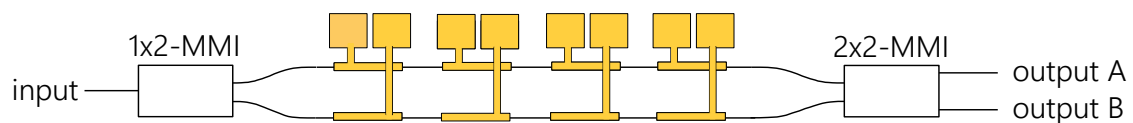


**Figure 2-7:** Segmented Mach-Zehnder modulator with 4 sections. The optical level of the MZM does not change with respect to a TWE-MZM. The TWE is however divided in multiple independent segments with dedicated input pads, all placed on one chip's side. Biasing sections are here omitted.

The change of electrode topology has multiple consequences that greatly affect the development of the SEMZM:

1. A number of electrical drivers, equal in number and pitch to the SEMZM sections, is required. IC driver chips with arrayed output stages are employed for this task. The segmented driver needs to be designed and adapted to the specific SEMZM it is developed for. Similarly, the development of the segmented modulator and its sections, thoroughly discussed in chapters 3 and 4, is itself closely bound to the driver capabilities.
2. These new dedicated drivers not only deliver the high frequency voltage, but are also required to manage the correct timing between the signals applied on the different segments. A better timing between the segments can be in practice implemented

thanks to dedicated stages that are easily included in the IC. A combination of passively loaded transmission lines and clocked arrayed logic has been proposed as a way to ensure a broad range of fine tuning possibilities [32]. The repositioning of the TWE in the driver chip also allows for periodic re-amplification of the high frequency data signal that has been attenuated during its travel. This results into a lower effective switching voltage. Moving the TWE to the electronics, the voltage-bandwidth trade-off is removed. The voltage-length product of equation (2-6) is still a valid figure of merit in the case of the SEMZM, but assumes a different form. In the case of a modulator with N segments, the equation can be rewritten as

$$\left( V_{\pi} \cdot \sum_{i=1}^N l_{e,i} \right) = k \quad (2-7)$$

with  $l_{e,i}$  being the length of the  $i$ -th segment electrode. If all the segments share the same length  $l_e$  then the equation simplifies to

$$(V_{\pi} \cdot N \cdot l_e) = k \quad (2-8)$$

In these formulations, the role of the number of segments and its relation to the switching voltage is highlighted. Due to the repositioning of the TWE to the IC, different choices of these product terms do not affect the EO achievable bandwidth of the modulator. However, different sets of  $V_{\pi}$ ,  $N$  and  $l_e$  values strongly influence the IC requirements and are thus not to be considered equivalent.

3. New driver topologies can be employed. In fact, because of the small dimensions of the SEMZM sections, the segments constitute spatially-small electrical loads. This is different than the case of the TWE-MZM, where a 50 Ohm driver is employed to drive the modulator transmission line. The SEMZM segments constitute lumped loads that are best driven by specific driver topologies, which allow for a reduction of the consumed power. CMOS inverter-based drivers are currently the most explored solution for this application, since they are expected to achieve lower power requirements by suppressing the static contribution of the power consumption [32], [33], [34], [14].
4. Different driving voltages, i.e. data streams, can be delivered to each of the different segments of the same interferometer arm. In this configuration, the driver-modulator assembly is no longer only a way to transfer information in the optical domain, but becomes capable of new functionalities, such as digital-to-analog conversion.

The segmented MZM together with its different applications is the topics of this work. Its proposed functionalities, i.e. optical digital-to-analog conversion, linearization, bandwidth enhancement, and spectrum shaping, are discussed in detail in the following chapters of this thesis.



---

## 3. Resonant SEMZM

### 3.1. Introduction

Most recent literature publications present the use of Segmented MZ modulators in order to obtain complex modulation formats without the use of a DAC to generate the required multilevel electrical signals. When used in this way, the SEMZM and its dedicated driver take on the task of digital-to-analog conversion and thus enable all DAC functionalities and DSP, provided sufficiently high bit resolution [14], [34], [35], [36]. This SEMZM usage is discussed in detail in chapter 4. In this chapter, a resonant version of the SEMZM is used to implement specific DAC-enabled functionalities in an analog fashion. This approach does not utilize DSP and does not introduce the concept of bit resolution. In particular, bandwidth enhancement by frequency equalization and Nyquist-space spectral shaping are here presented. The sections of the SEMZMs developed for these tasks are brought to resonance. The associated resonance, which gives rise to a peak in the modulator's transfer function, is engineered and employed in a range of different application scenarios.

#### **Bandwidth Enhancement by Frequency Equalization**

As the demand for data increases, optical communication channels with higher throughput must be developed. Complex modulation schemes such as PAM and QAM are very efficient and well-established ways of increasing the data rate without raising the bandwidth requirements. However, the current implementation of high order modulation schemes requires extra DACs and DSP. In addition, IQ-modulators and coherent detectors are necessary for the transmission of simultaneously phase and amplitude modulated signals. All this leads to higher complexity on both the transmitter and receiver side. In short reach scenarios such as in mega-datacenters, thousands of servers communicate over parallelized data channels. The large number of these channels typically makes the available bandwidth not a limiting factor. On the other hand, because of the large number of components, energy-efficient and simple system architectures are required [37]. A high symbol rate and a simple modulation scheme, e.g. OOK, is therefore the preferable choice. Unfortunately, the need for speed in electronics translates into growing costs, both in initial investment and power consumption.

In this chapter, the resonant SEMZM is proposed as a way to relax the speed requirements of the driving electronics, which may or may not include a DAC. The peaked

transfer function of the SEMZM is exploited in order to compensate for the high-frequency attenuation of bandwidth-limited drivers. This frequency equalization results into a bandwidth boost entirely performed by the SEMZM. Thus, electronics with a 3 dB-bandwidth lower than half the transmitted baud rate can be used. On one hand, this enables the use of slower and cheaper components in order to reach the same data rate. On the other hand, the SEMZM bandwidth boosting can also be used in order to reach record transmission rates, currently limited by the maximum available electronics' bandwidth. The possibilities offered by the peaking SEMZM are not only of interest for short reach scenarios. The usage of DACs and drivers with lower requirements for high data rates becomes appealing for any transmission link, including long reach applications. More than just lowering the electronics speed requirements, the peaking of the resonant modulator can be designed to perform frequency equalization and allow for lower resolution DACs to be employed. The segmented modulators presented in this thesis are designed to work in a 56 GBd OOK communication link. As a way to show the advantage of the resonant modulators compared to traditional MZMs, an OOK signal is transmitted at 56 GBd employing only driving electronics with a bandwidth lower than half the transmitted symbol rate. The specific design of these devices and their measurement results are reported in section 3.3.

#### **Nyquist-space Spectral Shaping**

The transmission of high data rate signals over a real-world communication channel means degradation of the signal itself. This degradation originates from multiple link-induced effects and becomes more and more critical as the link length increases. For an optical signal transmitted through a fiber, chromatic and modal dispersion plays a strong role in the occurring distortion and translates into a temporal spreading of the pulses that are launched at the fiber input. This ultimately causes detection errors in the received signal. In fact, because of the temporal spreading, subsequent symbols interfere with each other generating the so-called intersymbol interference (ISI). In presence of ISI, the transmitted symbols exceed their allocated time and act as noise on the adjacent ones. This results in a less reliable data link.

When multiple data channels are transmitted along the same fiber, it is possible that interference of one channel onto the adjacent ones occurs. This effect is the more pronounced the closer the channels are spaced. This is common in wavelength division multiplexing (WDM) links, where the full usage of the channel bandwidth is crucial in order to maximize the data throughput and the different channels are thus closely spaced. Interchannel interference (ICI) severely degrades the transmission performance, whose dependence on the ICI can be analytically modeled under some approximations [38]. To

intuitively understand it, one can look at the baseband spectrum of a typical non-return to zero (NRZ) pseudorandom binary sequence (PRBS). In the time domain, the voltage  $V(t)$  switches between a positive and a negative value. In the frequency domain, this corresponds to a signal power spectrum  $P(f)$  with a rectified sinc envelope with zeros at the baud rate  $BR$  and a 3 dB-bandwidth close to  $BR/2$  (Figure 3-1) [39]. The main frequency lobe is flanked by several sidebands that broaden the occupied bandwidth. Because of this broad signal spectrum, multiple data channels cannot be packed arbitrarily close together without overlapping, and thus not without interfering with each other, when transmitted simultaneously.

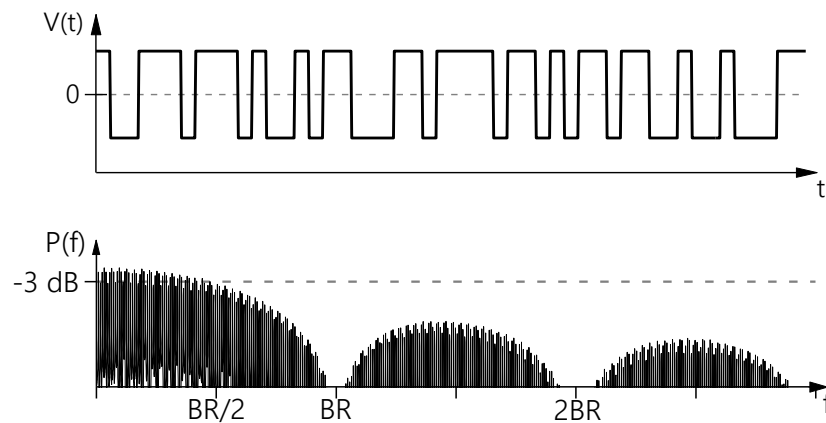


**Figure 3-1:** Time and frequency domain representation of a sufficiently random electrical NRZ signal. Square shaped time pulses translate in a frequency spectrum with rectified sinc envelope. The main frequency lobe goes to zero at  $BR$  and has a 3-dB bandwidth equal to  $BR/2$ .

Of the multiple ways to counteract ISI and ICI, Nyquist pulse shaping constitutes a well-implemented and powerful means to minimize their effects. The Nyquist pulse-shaping criterion gives the condition that a communication channel must satisfy in order to suppress ISI [40]. In practice, this condition is satisfied with baseband filters that shape the signal spectrum to a raised cosine (RC) spectrum. The frequency characteristic  $H(f)$  of these filters is given by:

$$H(f) = \begin{cases} T, & |f| \leq \frac{1-\beta}{2T} \\ \frac{T}{2} \left[ 1 + \cos \left( \frac{\pi T}{\beta} \left[ |f| - \frac{1-\beta}{2T} \right] \right) \right], & \frac{1-\beta}{2T} < |f| \leq \frac{1+\beta}{2T} \\ 0, & \text{otherwise} \end{cases} \quad (3-1)$$

where  $\beta$  is called the roll-off factor of the spectrum and  $T$  is the reciprocal of the symbol rate. The roll-off factor of the shaping takes values in the range  $0 \leq \beta \leq 1$  and expresses the

steepness of the edges of the signal spectrum. The time and frequency appearance of a Nyquist shaped signal for three different values of  $\beta$  is depicted in Figure 3-2.

Signals with smaller  $\beta$  show a steeper edge in frequency domain. For the particular case of  $\beta = 0$  the signal spectrum becomes a rectangular window with sideband width equal to  $BR/2$ . This is the minimum required bandwidth in order to avoid ISI, according to the Nyquist criterion [41]. The effect of the frequency domain spectrum shaping is thus to narrow the occupied bandwidth, reducing it to a compact envelope with no additional sidebands. Small values of  $\beta$  are optimal in WDM applications, as they minimize the ICI and enable the transmission of closely spaced independent signals without the need for broad guard bands in between them. Spectral efficiency is a key quantity in these scenarios as it expresses how much information is contained in a given bandwidth. By means of Nyquist shaping, the spectral efficiency can be maximized. In parallel with the suppression of the frequency components above half the symbol rate, an ideally Nyquist shaped signal shows a flat top. The emphasis of the frequency components just before  $BR/2$  maximizes the energy transmitted within the channel and lowers the noise enhancement that is otherwise induced by frequency equalization at the receiver side.

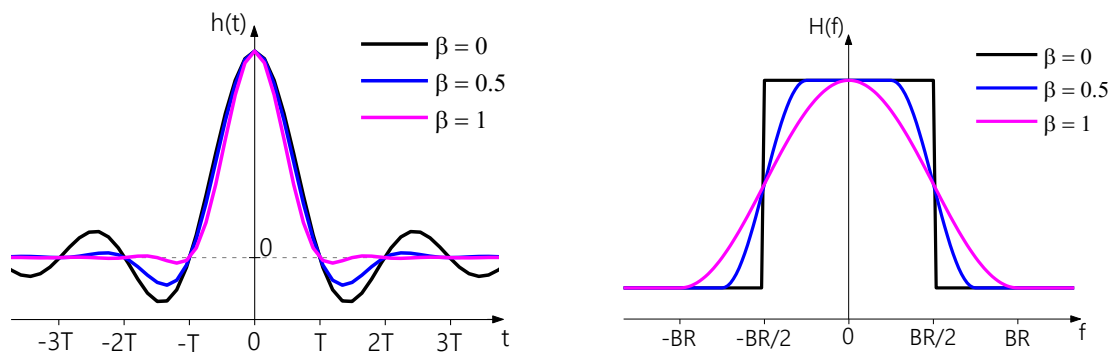


**Figure 3-2:** Time domain pulse and frequency spectrum of a Nyquist shaped signal for three roll-off factors  $\beta$ . A time-limited impulse response translates into a broad frequency occupation.

In the time domain, the eye diagrams of Nyquist shaped signals show a characteristic envelope that is also dependent on the roll-off factor. Simulated eye diagrams with different  $\beta$  show how a lower roll-off value translates into an eye with increased jitter (Figure 3-3). Additionally, a lower roll-off value also reduces the eye aperture along with the acceptable sampling interval. Because of the spectrum narrowing, the transitions between adjacent eyes exhibit an increasing amplitude overshoot and a related increase of the peak-to-average power ratio (PAPR). As a consequence, real transmission links face a trade-off between eye quality and occupied signal bandwidth. Offline DSP algorithms are a way to compensate the link-induced degradation and can therefore relax this tradeoff, as they reduce the requirements on the eye quality.

Current networks implement Nyquist shaping by means of DSP by pre-distorting the electrical signal or by using dedicated hardware filters. These pulse-shaping filters can be inserted at the transmitter, the receiver, or at both sides using a root-raised cosine (RRC) matched filter pair [39].

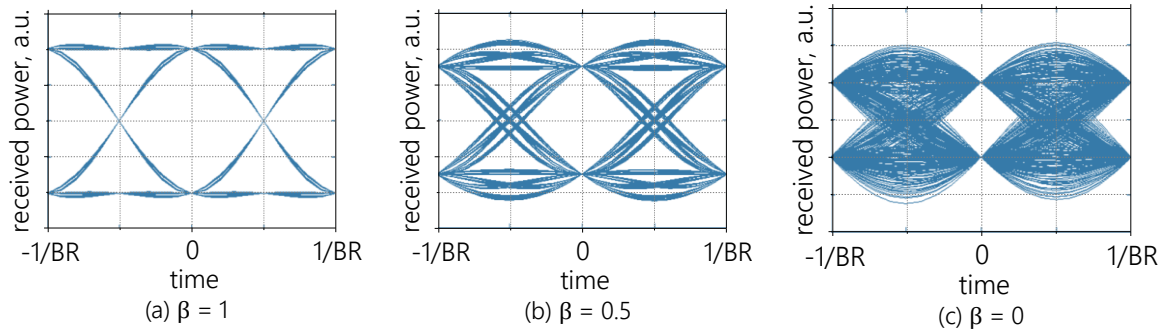


**Figure 3-3:** Eye diagrams of a Nyquist shaped signal for three roll-off factors  $\beta$ . Lower  $\beta$  values result in reduced bandwidth allocation but increased jitter and PAPR (adapted from [39]).

The resonant SEMZM presented in this work is proposed as a mean to achieve the spectrum shaping without the use of any DAC, DSP, or additional electronics on the transmitter side. The proposed shaping is performed completely in the analog domain through the frequency response of the resonant modulator. Both enhancement and suppression of specific frequency components is accomplished by the SEMZM in such a way that the output signal spectrum is close to that of a Nyquist-shaped signal. The proposed component is of particular interest for short reach links, e.g. within and between data centers. In such scenarios, a large number of parallel data links is implemented and the cost restrictions are more relevant than in long-haul applications. Typically, DACs are not present in these systems due to their price and energy consumption. Additionally, due to the short transmission distance, advanced DAC functionalities such as the compensation of channel-induced effects are not mandatory. Nyquist 4 level PAM has been shown to be a suitable candidate to transmit  $100 \text{ Gb/s}/\lambda$  over short distances [42]. Recent works address this issue by performing the shaping of the signal spectrum in the optical domain [43], [44]. However, the proposed solutions require dedicated external components and therefore add complexity to the system, which is undesired in these communication links. The presented resonant SEMZM enables the implementation of spectral shaping while bypassing the DACs drawbacks and, in contrast to the recently proposed solutions, adding little design complexity to the modulator itself with no need of any dedicated additional components. Although channel bandwidth availability is not the bottleneck in today's short-reach scenarios, the transmission of multiple closely spaced signals allows the simultaneous detection of different wavelengths with the use of a single broadband coherent receiver. Thus, the number of hardware components can be reduced. The modulator developed in the following sections is designed for a short reach 40 GBd data link. For this goal, a

rectangular spectrum with sideband width of 20 GHz is targeted. The device is employed in order to transmit up to a gross data rate of up to 320 Gb/s in a 4-PAM dual-carrier dual-polarization setup over a bandwidth of 100 GHz only. The design and measurements are discussed in section 3.4.

#### 3.2. Resonant SEMZM Design

The design of resonant SEMZMs includes a multitude of degrees of freedom. The choice of a specific set of design variables is strongly related to the intended application. In particular, the shape of the optical signal spectrum at the modulator's output is dependent on the specific design. This is in fact an optical domain combination of the input electrical signal and the SEMZM transfer function. In this process, the frequency response of each individual section of the modulator and the way these are combined plays the main role. The modulator's output MMIs also contribute to the modulated spectrum shape as they introduce harmonic distortions. Yet, the MMIs non-linearity becomes negligible in the first approximation if the modulator is driven in its linear region. In this situation, the optical output spectrum becomes an accurate reproduction of the overall segments' transfer functions. For this reason, the design of a single resonating segment is the core and the starting point for resonant SEMZMs development. The following section provides the theory behind a sections' resonance and presents a general design approach. Several design steps, down to the characterization of fabricated devices, are discussed, highlighting the main design parameters. Sections 3.3 and 3.4 address instead the design of SEMZMs for the applications discussed above.

##### 3.2.1. Segment Equivalent Model

The SEMZM sections constitute the load of its dedicated IC driver output stages. This driver is brought as close as possible to the modulator and is typically bonded with short gold bondwires. As discussed in section 2.3, the small dimensions of the segments and of the interconnections to the IC make wave propagation effects negligible. Each individual section can be therefore modelled with a lumped electrical circuit. There is no strict delimitation between the lumped and distributed regime for an electrical circuit. In order to ensure the validity of this model, the circuit characteristic length  $L_c$  must be smaller than the shortest operating wavelength. As a rule of thumb, a fraction of the shortest signal wavelength  $\lambda_{min}$  is considered and the critical dimension is calculated as

$$L_c = \frac{1}{8} \cdot \lambda_{min} = \frac{1}{8} \cdot \frac{c}{n_e \cdot (0.7 \cdot BR)} \quad (3-2)$$

where  $c$  is the speed of light in vacuum,  $BR$  the baud rate of the transmitted signal, and  $n_e$  the effective refractive index experienced by the electrical wave. The estimation of  $n_e$ , and therefore of the electrical wave speed, is not trivial due to the complex geometry of the electrodes. The electrical wave propagates on the chip partially in air and partially in InP, the latter being the slowest medium. A cautious estimation is thus obtained by substituting  $n_e$  with  $n_{InP}$ . The operating frequency is instead derived from the maximum operating data rate as follows. The Nyquist rate expresses the minimum required bandwidth for the case of a noiseless channel in order to successfully transmit a signal, and is equal to  $BR/2$  [45]. Because of the noise degradation in real channels, 70 % of the symbol rate is used here instead. The highest data rate transmitted in this work is 56 Gb/s for which a critical length of about 300  $\mu\text{m}$  is calculated. For the case of slower operation, this limit has to be recalculated accordingly. The lumped condition translates, in practice, to a maximum boundary on the segments' and interconnects' lengths. When this condition is met, a lumped circuit models the two branches of a modulator's segment, together with assembly-derived components (Figure 3-4).

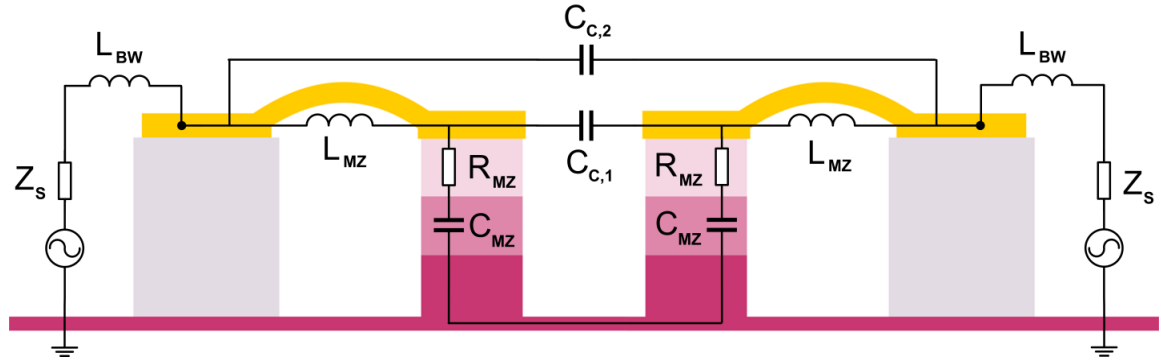


**Figure 3-4:** Cross-section of a SEMZM segment with its equivalent lumped model. The intrinsic area of the pin junction is modeled by the capacitors  $C_{MZ}$ , the contact resistance by  $R_{MZ}$ , and the parasitic inductance by  $L_{MZ}$ . Additional capacitors  $C_{C_i}$  model the coupling between adjacent segments' branches. Last, the external bondwire inductance  $L_{BW}$  and the source impedance  $Z_s$  model the interconnections and the drive load.

In this symmetric circuit, a number of capacitors, inductors, and resistors are employed to faithfully represent the segments' physical structure and model its frequency characteristic. The segment's capacitors  $C_{MZ}$  take into account the junction capacitance of the reversely biased pin diodes. Because of their geometry, these capacitors can be thought of as parallel plates, where the doped InP layers represent the capacitor plates and the junction depletion regions constitute the dielectric. The capacitance  $C_{MZ}$  is thus evaluated as:

$$C_{MZ} = \epsilon_0 \epsilon_r \cdot \frac{l_e w_w}{x_d} = \epsilon_0 \epsilon_r \cdot \frac{l_e w_w}{IRT} \quad (3-3)$$

where  $\epsilon_0$  and  $\epsilon_r$  are the permittivity of free space and the InP dielectric constant, respectively,  $l_e$  is the electrode length,  $w_w$  the waveguide width, and  $x_d$  the depletion region thickness. Due to the strong doping of the junction p- and n-layers in the employed InP technology, the depletion region does not extend significantly into these areas and is thus approximated by the physical intrinsic region thickness IRT. The junction capacitance is consequently assumed to be independent from the voltage applied on the diode. The resistors  $R_{MZ}$  represent the overall series resistance seen from the segment's inputs. The largest contributions to these resistance come from the p- doped layers of the junctions and their contact resistances. Even though the resistance of the gold contacts is small for DC and low frequencies, its contribution increases in the gigahertz range. In fact, to properly model the segment structure, the frequency dependence of the resistors  $R_{MZ}$  must be considered. The distribution of high-frequency alternating current is concentrated within the skin depth  $\delta$ , which is given, for good conductors, by [46]:

$$\delta = \sqrt{\frac{2\rho}{\omega\mu}} \quad (3-4)$$

where  $\omega$  is the operating pulsation,  $\rho$  the material conductivity, and  $\mu$  its magnetic permeability. The resulting resistance is evaluated starting from this expression for  $\delta$  by calculating the effective conduction area. Although the electrodes of the segment have complex geometries, they share a thickness and width for most of their length. Average values are therefore used to keep the model complexity to a minimum. The inductors  $L_{MZ}$  represent the parasitic inductances of the segment's electrodes and of the gold bridges used to connect them to the input pads. In addition to the modulator's parasitics, a part of the overall inductance arises from the interconnections, i.e. the bondwires, employed to interface the SEMZM sections to the outside world. The bondwire inductance  $L_{BW}$  is typically one to two orders of magnitude larger than the one of the segment, and is therefore the most relevant contribution to be considered during the design phase. Furthermore, the segment's lumped model includes two capacitors  $C_{c,i}$ . These are to model the coupling effects between the two adjacent pads and the two facing electrodes. With proper design choices, the value of these coupling capacitors can be brought into the fF range, therefore making their influence negligible for operating frequencies, i.e. below 40 GHz. The last building block of the lumped model is the source impedance  $Z_S$ . This impedance, seen at the driver output, becomes the load of the RLC resonator and, even though not part of it, has to be considered during the design phase. The overall model of the SEMZM segment can be halved due to its symmetry. The shared n-layer is biased at a constant voltage and is therefore grounded for the RF signal. Taking into account the possible simplifications, the

lumped model becomes a simple RLC series circuit (Figure 3-5). This segment's model is precise enough to properly describe a wide range of resonating segments, keeping the number of lumped components to a minimum. This model is hereafter employed for the development of different segments.

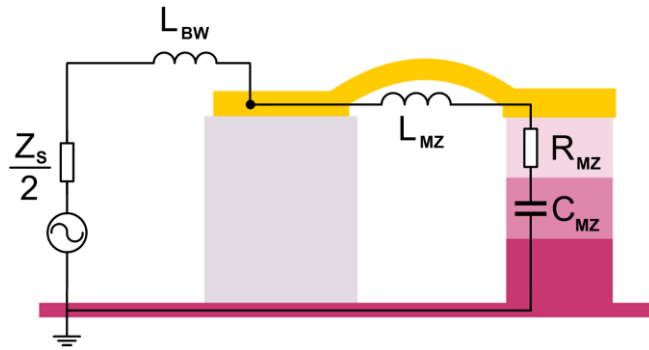


**Figure 3-5:** Simplified RF model of the SEMZM segment single branch. The equivalent circuit is a series RLC resonator with  $L = L_{MZ} + L_{BW}$ . The source impedance  $Z_S$  is divided between the two arms of the segment.

The unloaded series RLC circuit resonates at its natural resonance frequency

$$f_o = \frac{1}{2\pi\sqrt{L \cdot C_{MZ}}} \quad (3-5)$$

where  $L$  is the sum of  $L_{MZ}$  and  $L_{BW}$  [47]. Because of the resonance, the impedance seen at the segment's input  $Z_{in}$  is strongly non-linear. This impedance constitutes the load of the IC driver employed to drive the SEMZM and therefore represents an important property of the section. Furthermore, the segment's input impedance is the quantity that can be most easily measured with a standard electrical network analyser.  $Z_{in}$  represents the simplest way to electrically characterize the different sections and extract the resonators' RLC parameters, which on the contrary are non-directly measurable.

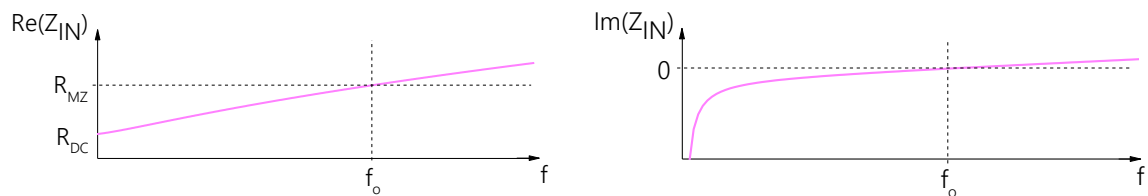


**Figure 3-6:** Real and imaginary parts of the segment  $Z_{IN}$ . The real part gives insight on the section resistance, whereas the imaginary part can be used to determine the segment's resonance frequency  $f_o$ .

Both the real and imaginary parts of  $Z_{in}$  provide useful information on the SEMZM segment (Figure 3-6). The resonance frequency  $f_o$ , in the formulation of equation (3-5), is most commonly defined as the frequency for which the reactance of the inductor equals, with opposite sign, the one of the capacitor, i.e.  $X_L = -X_C$ . At this frequency,  $\text{Im}(Z_{in}) = 0$  i.e.

the segment's impedance is purely resistive and equal to  $R_{MZ}$ . At frequencies lower than  $f_o$ , the segment constitutes a capacitive load and beyond the resonance the load becomes inductive. The wide range in which  $Z_{in}$  changes gives rise to a challenge when these structures are to be driven.

At the resonance frequency, the overall circuit impedance  $Z_{in}$  is less than the single capacitive or inductive reactance. As a consequence, the voltage  $V_C$  across the capacitor is magnified and becomes larger than what is provided by the driving source (Figure 3-7). The amplitude of  $V_C$  is equal to  $Q$  times the one provided at the resonator input,  $Q$  being the quality factor of the resonating circuit [48]. This voltage drops over the intrinsic region of the InP waveguide, i.e. where the light propagates. As a consequence of the larger voltage applied on the active area of the modulator, the electro-optical effect is improved and a larger phase shift is induced according to equation (2-1). The effect of the resonance is a peak that is clearly observed in the modulator's transfer function.

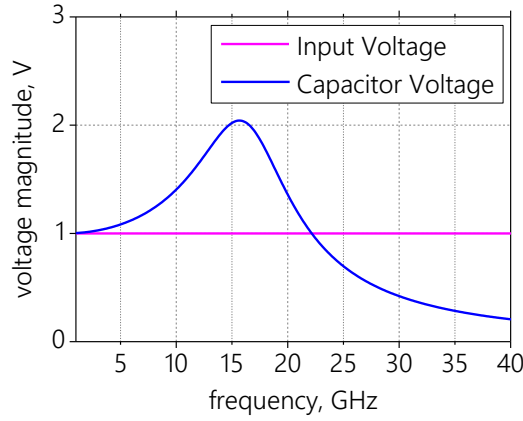


**Figure 3-7:** Voltage at the input of the segment and over the junction capacitance for a resonator with  $f_o = 16$  GHz and  $Q = 2$ . Voltage peaking is observed at the resonance, where the capacitor voltage is magnified  $Q$  times the value at the segment's input.

Alternative definitions of the circuit resonance frequency, although less common, exist. Because of the frequency dependency of the damping resistor, the condition of a purely real  $Z_{in}$  does not directly translate to a minimum magnitude. A different formulation of the resonance frequency can thus be derived, which differs from the former as it depends on the circuit resistance [49], [50]. Considering the purpose of this work, a meaningful way to define the segment's resonance frequency is the frequency  $f_{eo}$  for which the voltage drop over the reactive components is at its maximum:

$$\frac{d}{d\omega}|V_C| = 0 \quad . \quad (3-6)$$

This resonance frequency definition closely relates to the quantity of interest of the SEMZM

design, i.e. the voltage over the junction capacitor. An analytical formulation of  $f_{eo}$  is not a trivial derivation when the number of lumped components in the segment equivalent circuit is large. In the case of the simplified model, the exact formulation of the resonance frequency as function of the RLC parameters is possible. This relationship is calculated starting from equation (3-6), and expressing the voltage  $V_C$  as function of the circuit impedances. With omitted subscripts:

$$\frac{V_C}{V_{in}} = \frac{\frac{1}{j\omega C}}{R + j\omega L + \frac{1}{j\omega C}} \quad (3-7)$$

In this formulation, the source impedance  $Z_S = (R_S + j \cdot X_S)$  is assumed to be purely real for the sake of simplicity and is included in the overall damping resistance  $R = (R_{MZ} + Z_S)$ . In addition, both  $Z_S$  and  $R_{MZ}$  are considered constant over frequency with negligible introduced error. By setting the derivative with respect to  $w$  equal to zero, the voltage magnitude on the junction is maximized for

$$\omega_{eo} = \sqrt{\frac{1}{LC} - \frac{R^2}{2L^2}} \quad \text{and} \quad f_{eo} = \frac{1}{2\pi} \cdot \sqrt{\frac{1}{LC} - \frac{R^2}{2L^2}} \quad (3-8)$$

Compared to  $f_o$  as defined in equation (3-5), the maximum of  $V_C$  occurs at a lower frequency  $f_{eo}$ . In case of low damping, the term  $R^2/2L^2$  tends to zero, and  $f_{eo}$  approaches  $f_o$ . On the other hand, large values of  $R$  cause a non-negligible shift in the resonance frequency. Above the limiting value of  $R = \sqrt{2L/C}$  the square root argument becomes negative and the voltage is no longer enhanced. This case corresponds to the one of a resonance with quality factor  $Q = 1$ . The exact value of  $Q$  can be calculated starting from the voltage transfer function  $V_C/V_{in}$ . Evaluating it at the resonance by introducing the  $\omega_{eo}$  formulation from equation (3-8):

$$Q = \frac{1}{\omega_{eo} C \cdot \sqrt{\left(\omega_{eo} L - \frac{1}{\omega_{eo} C}\right)^2 + R^2}} = \frac{2L}{R \cdot \sqrt{C(4L - R^2C)}} \quad (3-9)$$

As expected, the effect of the loading resistor is to lower the quality factor of the RLC circuit. With respect to alternative definitions of the  $Q$  factor [51], the one of equation (3-9) provides the exact magnitude of the voltage magnification effect not only at the resonance frequency, but also above and below it. It is also valid for circuits with high loading resistances, i.e. when the quality factor approaches unity. However, in contrast to the case of the resonance frequency  $f_{eo}$ , the dependency of the series resistance  $R$  on the frequency cannot be neglected if high precision in the estimation of  $Q$  is required. Instead, the value

of the resistance has first to be evaluated at the desired frequency and then inserted into equation (3-9).

Expressions (3-8) and (3-9) are used to derive the resonator properties  $f_{e0}$  and  $Q$  starting from the lumped RLC parameters. For a particular set of  $R$ ,  $L$  and  $C$  a specific resonance frequency and quality factor exist. However, these parameters are linked not only to the resonator properties in the electrical domain, but also to the modulator's ones on the optical level. For this reason, the SEMZM designer has to select the junction capacitance  $C_{MZ}$ , keeping in mind that degrees of freedom such as the electrodes length, the waveguide width and the intrinsic region thickness also influence the component's EO behavior. Similarly, the resonator inductance and resistance can be both engineered by modifying the electrodes and junction design, with analogous consequences. By using the analytical expressions of  $f_{e0}$  and  $Q$ , the resonator properties are represented in a three-dimensional RLC space.

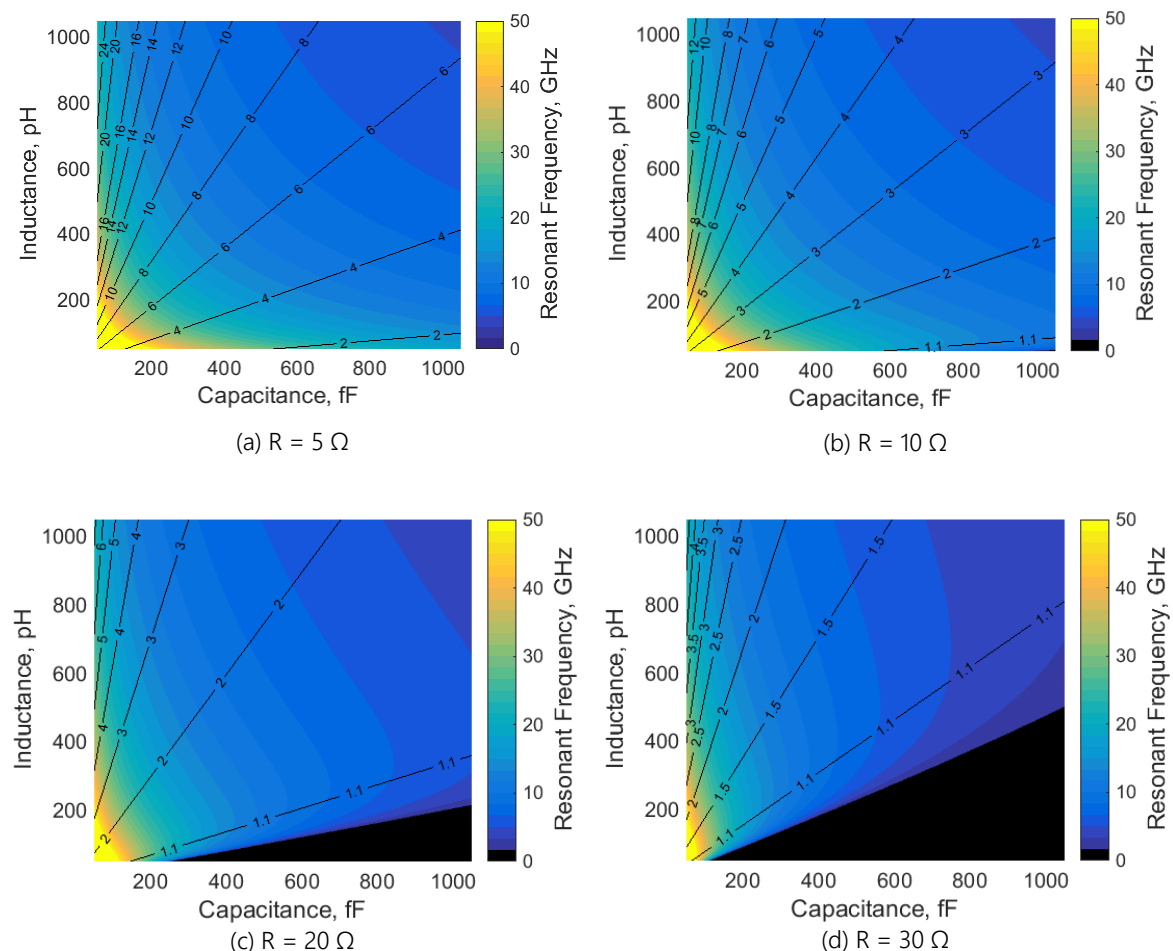


**Figure 3-8:** Resonator properties in LC space for different loading  $R$ . The resonance frequency is plotted in the color map and the  $Q$ -factor is represented by contour lines. The over-damped areas are given in black.

These maps constitute a useful mean to help the designer keep track of the effects of a different choice of a parameters set. The graphs are built by plotting the calculated values

of  $f_{e0}$  on color maps and the associated  $Q$  on contour lines in the LC bi-dimensional space for different loading resistance values (Figure 3-8). The areas corresponding to over-damped resonators, i.e. those with  $Q < 1$ , are blacked out. These plots are obtained for reasonable ranges of the LC parameters. Similarly, the selected values of the series resistance are representative of what is physically achievable in real segments,  $5 \Omega$  being the absolute minimum. As outlined in more detail below, within these limits some dependencies become immediately visible. For any value of  $R$ , higher quality factors are achieved with low capacitive loads and high inductive ones. Resonators with large capacitors require large inductance values in order to show an appreciable resonance peak, if any. Because of the inverse proportionality of the quality factor with the loading resistance, the maximum achievable  $Q$  quickly decreases as the resistance grows.

### RLC Limits

The bounds on the achievable resonance frequencies and associated quality factors are derived from the ones on the RLC parameters. In practice, these parameter values are limited by a number of design-derived and technology constraints. An overview of these boundaries and limitations is summarized in Table 3-2. These different constraints, specific for the aforementioned topology of the segment, limit the accessible portion of the RLC space and are thus to be considered together.

Concerning the section resistive load  $R_{MZ}$ , a challenge arises when it has to be minimized. Through optimization of the layout of the segment and interfaces, the DC p-layer and p-contact resistances can be brought down to the few  $\Omega$  range. This is also valid for the contributions of the electrodes and interconnects. However, their frequency dependency increases this value in the GHz range, where resonance occurs. In the case of the experiments described in this work, the main contribution to the loading resistance  $R$  comes from the source impedance  $R_S$ . The two arms of the segments are driven by a  $50 \Omega$  amplifier and thus an additional  $25 \Omega$  load on the single-ended segment's branch must be taken into account. The identification of an upper bound to the damping resistance is not of interest for the foreseen SEMZM applications.

Concerning the resonator inductance, of the two contributions  $L_{MZ}$  and  $L_{BW}$ , the latter limits both the minimum and maximum feasible values. For a gold bondwire of constant diameter,  $L_{BW}$  is proportional to the bondwire length. Its maximum achievable value is once again related to the lumped condition of equation (3-2), this time with  $n_e$  approaching unity. Under this condition, an inductance as high as 1 nH can be practically implemented. On the lower side, short and broad wires, as well as alternative integration method such as flip-chip, can be employed to minimize  $L_{BW}$ . However, this inductance cannot be brought

down to zero. An optimized design bonded with a ribbon wire as short as 200  $\mu\text{m}$  translates into a minimum L value in the range of 100 pH.

The optical wave travels through the InP waveguide, in the region correspondent to the dielectric of the junction equivalent capacitor. The value of  $C_{MZ}$  is for this reason strictly related to the EO modulation efficiency of the segment. Equation (3-3) highlights the main design parameters that affect the pin capacitor: the electrode length  $l_e$ , the waveguide width  $w_w$ , and the junction intrinsic region thickness IRT. The electrode length is limited in its maximum value by the SEMZM operating frequency, as in equation (3-2). On the other hand, the lowest acceptable value of  $l_e$  is related to the derived switching voltage  $V_\pi$  through the number of segments N, according to equation (2-7). The InP waveguide width  $w_w$  has an impact on the number of optical modes that are allowed to propagate through the modulator's active areas and is therefore constrained in the range of a few  $\mu\text{m}$  when single-mode operation is desired. However, a very small  $w_w$  value brings significant technological challenges and larger optical losses due to the increased overlap of the optical mode with the waveguide surfaces. Lastly, the IRT has a strong impact on the EO efficiency, the electric field over the capacitor being approximated by  $V/\text{IRT}$ . Whereas the maximum IRT value is related to maximum acceptable  $V_\pi$ , the lower bound to the intrinsic region thickness comes from the increased optical losses that arise when a significant portion of light propagates in the p-doped InP layer. Considered together, these bounds translate into a feasibility range for the segment's capacitance from an arbitrarily small 100 fF up to 350 fF, in the case of 20 GHz operation with  $L_c \approx 500 \mu\text{m}$ . If the single mode propagation of light in the active areas can be sacrificed, this upper limit can be reasonably increased to 1 pF.

Parameter	Limit	Source
R	Min: 30 $\Omega$	segment's parasitics, 50 $\Omega$ environment
L	Min: 100 pH	segment's parasitics, interconnects' inductance
	Max: 1 nH	lumped condition
C	Min: 100 fF	modulation efficiency
	Max: 350 fF	lumped condition, single-mode waveguide
	Max: 1 pF	lumped condition, multi-mode active waveguide

**Table 3-1:** RLC parameters limitations with their principal sources.

### RLC Variations

Technology not only imposes boundaries to the RLC parameters' range, but also introduces a limit to the precision that can be achieved on the target parameters

themselves. Fabrication tolerances, together with imperfections of modelling and simulation tools, are the main source of variations between fabricated structures parameters and their target values. These sources of uncertainties can be divided into systematic and random ones [52, pp. 93-97]. The systematic errors are predictable deviations and are typically constant or proportional to the true value. These errors can be overcome through a process of optimization of device modelling and development tools. The improvements of the simulation models and the correction of technological offsets are uncertainty sources that are part of this category. On the contrary, random errors distribute around the zero value and cannot be neither predicted nor corrected a priori. Imprecisions in processing steps performed by hand or instrument fluctuations enter this class. Each of the RLC parameters is affected by specific sources of both kinds of errors that together give rise to tolerance intervals in which they are expected to be included. The impact of the tolerances of the circuit parameters on the resonator properties can be investigated mathematically. The derived expressions for the segments' resonance frequency (3-8) and quality factor (3-9) can be differentiated under the simplification that the RLC parameters are independent and the error on each of them is sufficiently small. The maximum uncertainty is then given by [52, pp. 73-79]

$$\Delta g(x_1 \dots x_k) = \sum_{j=1}^k \left| \frac{\partial g}{\partial x_j} \right|_{x_j=x_{j0}} \Delta x_j \quad (3-10)$$

where  $g(x_1 \dots x_k)$  is a general function of the  $x_i$  variables and  $\Delta g$  its uncertainty. For equation (3-8) this results in

$$\Delta f_{e0} = \frac{1}{8\pi^2 f_{e0,0}} \cdot \left( -\frac{1}{C^2 L} \cdot \Delta C - \frac{R}{L^2} \cdot \Delta R + \left( \frac{R^2}{L^3} - \frac{1}{CL^2} \right) \cdot \Delta L \right) \quad , \quad (3-11)$$

$f_{e0,0}$  being the resonance frequency calculated for zero uncertainty. The absolute error on the resonator quality factor is similarly derived by differentiation of equation (3-9). Both the obtained uncertainty expressions are evaluated numerically due to their complex formulation. To estimate the maximum variations over  $f_{e0}$  and  $Q$ , the largest uncertainties expected for the RLC parameters are inserted in the formulas. These include both systematic and random errors (Table 3-2). The individual impact of each of these errors is dependent on the originally targeted value. The uncertainty propagation is thus evaluated for the specific design considered. A segment of interest to the aforementioned applications is considered here, as a case study. The resonator is designed for a resonance frequency of 20 GHz and a quality factor equal to 2.

The RLC parameters uncertainty contributions to the  $\Delta f_{e0}$  and  $\Delta Q$  uncertainties are separated and independently investigated (Figure 3-9). Bigger absolute deviations are to be

expected for segments with higher resonance frequencies and quality factors. The largest contribution to the propagated error on the resonance frequency comes from both the capacitance and the inductance uncertainties. The maximum  $f_{e0}$  deviation for high frequency resonators can be larger than 10 % the target value. Over the whole frequency range, the impact of  $\Delta R$  on the resonance frequency is small. The absolute uncertainty on the segment's quality factor  $\Delta Q$  is dominated by the error on this resistance value. The  $\Delta L$  impact on  $\Delta Q$  is small.

Parameter	Expected Variation	Source
R	$\pm 5 \Omega$	modeling doping variations contacts' quality
L	$\pm 60 \text{ pH}$	modeling bondwires' length
C	$\pm 30 \text{ fF}$	modeling electrodes' shape

**Table 3-2:** Expected uncertainty on the RLC parameters with their principal sources.

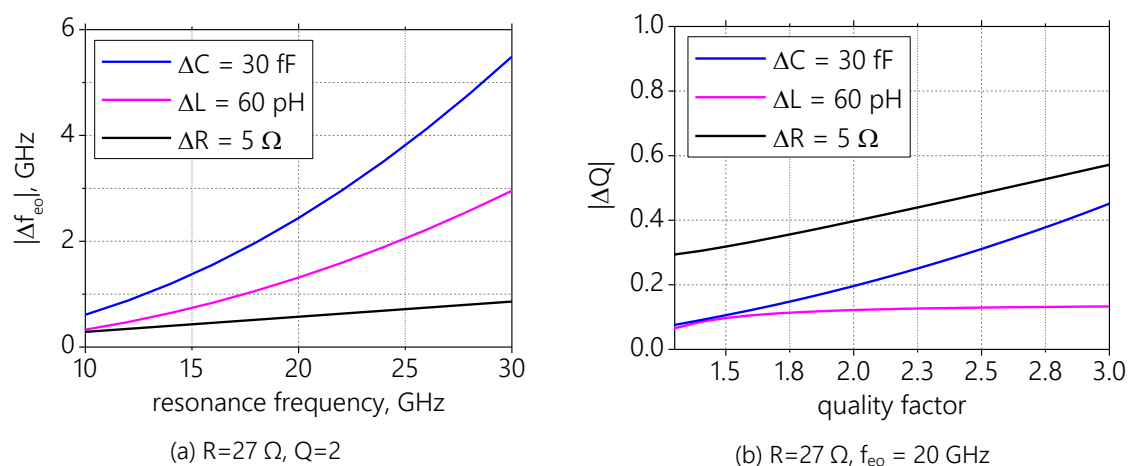


**Figure 3-9:** Expected contribution of the individual RLC uncertainties on the segment's resonance frequency and quality factor for a case study segment.

Corner resonators, i.e. those for which the measured parameter values differ the most from the expected ones, are obtained when the different error contributions sum with the same sign. In these cases, the uncertainty for the resonator properties can be as large as 30 % of the target values. However, after a prototyping phase, the systematic errors can be minimized and random errors, which are significantly smaller in amplitude, distribute in a

Gaussian way around the target values, reducing the impact of error propagation for large production volumes.

Of the several sources of uncertainty, the wirebonding process represents a particularly critical one. Because of the difficulty in the realization of bondwires of precise length and the consequent low reproducibility, the circuit inductance contributes the most to the deviation of resonator properties.

### 3.2.2. EM simulations

The analytical formulation and analysis of resonator properties provides the necessary theoretical understanding for the design process of the segment and delivers the desired resonators' parameters. Once these are selected, the calculated RLC parameters must be implemented in the physical layer. 3D electro-magnetic (EM) simulations offer the link between these two steps. Through EM simulations, different segment structures are investigated and their equivalent RLC values are extracted. Although they are a powerful tool, EM models do not include all the aspects that come from the SEMZM optical domain. Waveguide width  $w_w$ , electrodes length  $l_e$ , and intrinsic region thickness IRT are representative degrees of freedom of the design that are strictly related to the optical domain and are thus subject to specific limitations that cannot be neglected.

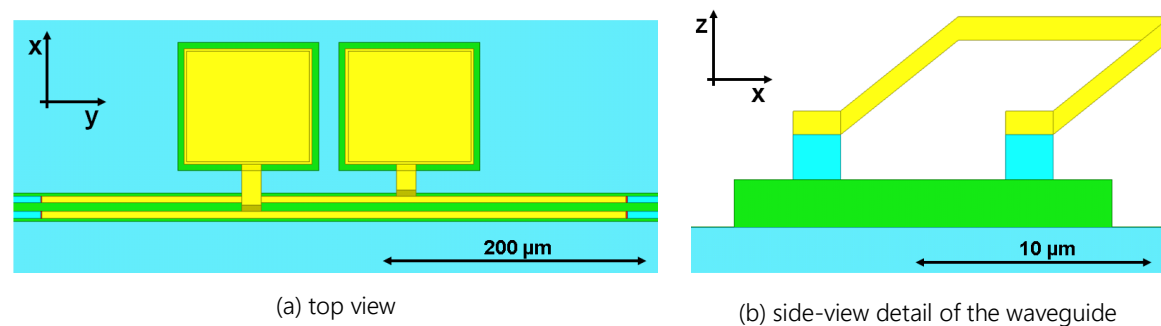


**Figure 3-10:** 3D EM model of a modulator's segment. The simulated structure is a faithful copy of the fabricated one, both in geometry and material definition.

A 3D model of a single modulator's segment is built in the EM simulator (Figure 3-10). The waveguide pin structure is faithfully reproduced both in the geometry and in the material definitions. The two gold input pads are added on one side of the metallized waveguides and are connected to them by thin gold bridges. The whole structure lies on the top of an InP substrate, wide enough to be considered, for simulation purposes, infinite in the x and y directions. Gold bondwires and a ceramic substrate must also be included in order to reproduce the fully assembled segments and include the section. However, each additional component adds complexity and constitutes a possible source of error. Furthermore, a more complex EM model makes it harder to isolate the effect of the

waveguide and electrode layouts on the RLC parameters among the others. For these reasons, the InP segments are simulated as stand-alone structures. The electrical excitation for the implemented model is provided by 2D surfaces, i.e. the ports. These ports provide two terminals each and represent an interface to the external world, in analogy with their role in network-theory. The output of the simulation is an S-parameter file, which is then taken as input in handier circuit-level investigations. The segments' models are constructed as 2-port networks. This is possible both in a purely electrical fashion (Figure 3-11-a), or with the definition of one electrical and one optical port (Figure 3-11-b). In the purely electrical setup, the two ports share a common reference and are placed in between the segment's input pads. In this way, the input signals for each segment's branch can be individually controlled. As a particular case, differential electrical signals can be applied to the segments. The electro-optical configuration is constructed by placing a single electrical port between the two input pads and an optical port in the middle of the InP waveguide, perpendicular to the pin structure. Although one pad is in this setup employed as a reference, the advantage of this configuration lies in the possibility of directly investigating the voltage  $V_C$  over the pin intrinsic region, i.e. the equivalent circuit capacitance  $C_{MZ}$ . In small-signal operation, the relationship between  $V_C$  and the induced phase shift reduces to a linear dependency, the quadratic term of equation (2-1) being negligible. In addition, in the small-signal domain the modulator's MMIs behave as linear components, under proper SEMZM bias. Thus, the simulated S-parameters at the optical port boast a 1 to 1 correlation to what is measured at the output of the real fabricated modulators. Although a 3-port simulation shows the advantages of both port configurations, it is difficult to reproduce in a lab setup and is therefore undesirable.

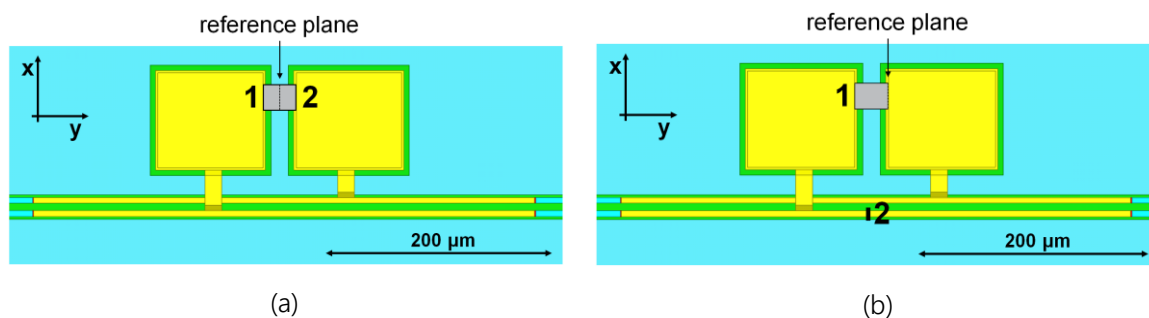


**Figure 3-11:** Different 2-port configurations for the electromagnetic model of the segment: (a) purely electrical and (b) electro-optical setups. Whereas in the former the segment's inputs can be individually set, the latter shows a direct connection to what is measurable in the fabricated structures.

The lumped circuit equivalent that best models the behavior of the EM-simulated structure is extracted by identifying the RLC triplet that minimizes the root-mean-square deviation between the two sets of simulated S-parameters. The comparison between the EM model and lumped circuit small-signal frequency response shows good agreement up

to the maximum simulated frequency of 40 GHz (Figure 3-12). The simplified lumped circuit of Figure 3-5 is proven to be a valid model for the EM-simulated geometry over the complete frequency range of interest. High frequency agreement can be further improved using the full lumped circuit, i.e. including the additional coupling capacitors. For a segment 450  $\mu\text{m}$  long and 2  $\mu\text{m}$  wide, the extracted RLC values are  $C_{MZ} \approx 230$  fF,  $L_{MZ} \approx 65$  pH and a  $R_{DC} \approx 1 \Omega$ .

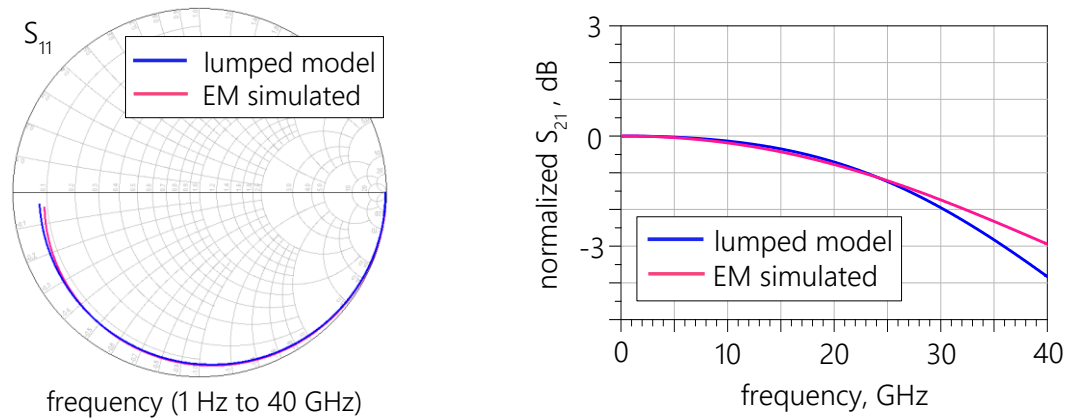


**Figure 3-12:** Comparison of EM and lumped model simulated S-parameters for a 450  $\mu\text{m}$  long segment. The agreement between the two curves proves the validity of the segment simplified model.

The 3D model is parameterized in order to ease the direct investigation of different design variations. In this way, each degree of freedom of the design is individually investigated and its effects on the RLC values are quantified. Critical quantities, for which particular care during the fabrication phase must be taken, are thus identified. Because of the high impact different IRT values show on the EO efficiency and since a single IRT must be shared between all the different segments, this parameter is here assumed to be a design constant rather than a variable. The values of the L and C parameters are extracted for different electrodes lengths  $l_e$  and widths  $w_w$ , swept over their feasibility range (Figure 3-13). Although a large variation of  $C_{MZ}$  is observed, the parasitic inductance  $L_{MZ}$  stays constant with respect to  $w_w$  and is always above 40 pH. Further reduction of the segment's inductance, pursued in chapter 4, can be obtained with the use of specific designs, but does not approach zero because of the thin gold constituting the electrodes. The electrode design, in both its length and width, can in the first approximation be thought of as a way to control  $C_{MZ}$  only. With respect to the analytical calculations from equation (3-3), the simulated segment's capacitance is larger by a constant offset but shows the expected dependencies on both the segment's length and width. This simulated offset, equal to circa 50 fF, is attributed to the fringe fields that are not considered in the parallel plate approximation. In addition, extra capacitance originates in other areas of the segments and contributes to the simulated  $C_{MZ}$ .

The EM simulator allows for the investigation of additional effects that are not related to the RLC parameters of the segment. A model with two segments side-by-side is set up and the cross talk between the two is simulated (Figure 3-14). The spacing  $d$  between the adjacent active areas is set to  $25\ \mu\text{m}$  in order to ensure no electrical connection is created between the adjacent p-doped active areas. For this distance, the simulated cross talk between the two segments stays below  $40\ \text{dB}$  for the whole frequency range.

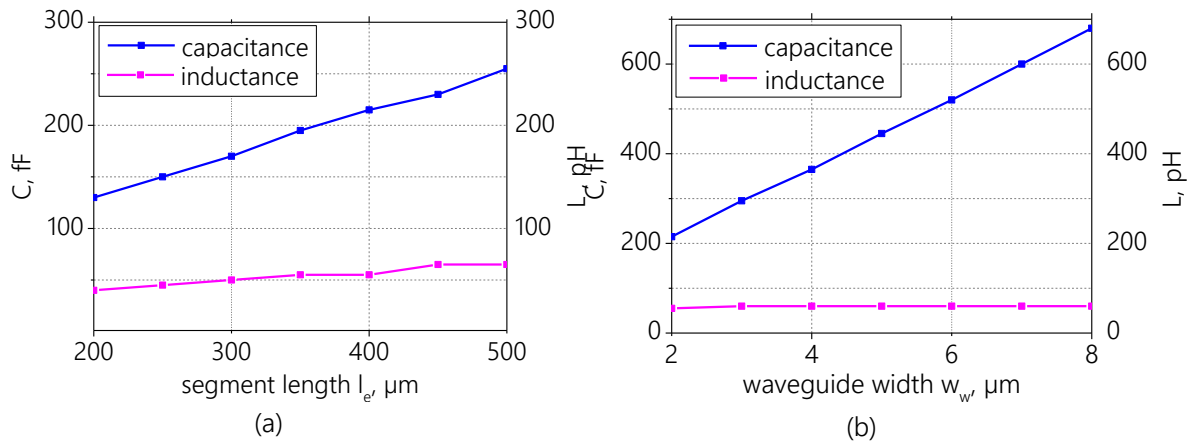


**Figure 3-13:** Lumped model capacitance and inductance for different electrode designs: (a) length variation with constant  $w_w = 2\ \mu\text{m}$  and (b) width variation for a  $400\ \mu\text{m}$  long segment. The scatter points represent the simulated steps.

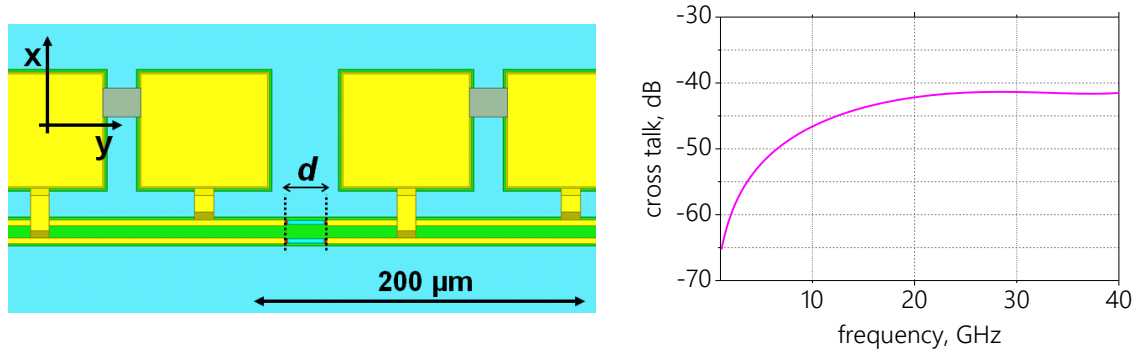


**Figure 3-14:** 3D model of two adjacent segments and simulated cross talk between them for a distance of  $25\ \mu\text{m}$ . This distance is compatible with the used technology and ensures no electrical connection is created between the different p-doped waveguide areas.

## 3.2.3. Analytical model

The analytical description and the electrical modeling of the SEMZM segments discussed above constitute the core of the resonant SEMZM design process. However, full understanding of the modulator requires a more general mathematical model that includes all the effects that do not originate in the electrical domain. A large-signal time and frequency domain model of the complete SEMZM is developed for this purpose. The complete SEMZM is not a time-independent linear system and must therefore be modeled as dynamic and non-linear. However, the modulator can be decomposed into discrete sub-systems, which can be modeled independently, allowing for a simplification of the problem [53], [54].

Starting from the individual resonator transfer functions, the implemented model calculates the overall induced phase shift. In addition, the model takes into account the MMIs transfer functions, including their non-linearity. Thus, the total SEMZM frequency response is calculated and the time domain waveform at the output is simulated. Advantages of this complete analytical model include the possibility of investigating the effects that come into play when more than a single segment is driven, i.e. when multiple resonators with different geometries are implemented in the same SEMZM. The impact of timing inaccuracy between the electrical and the optical wave can also be investigated and its impact on the modulation performance can be predicted. A schematic representation of the model algorithm is shown in Figure 3-15.

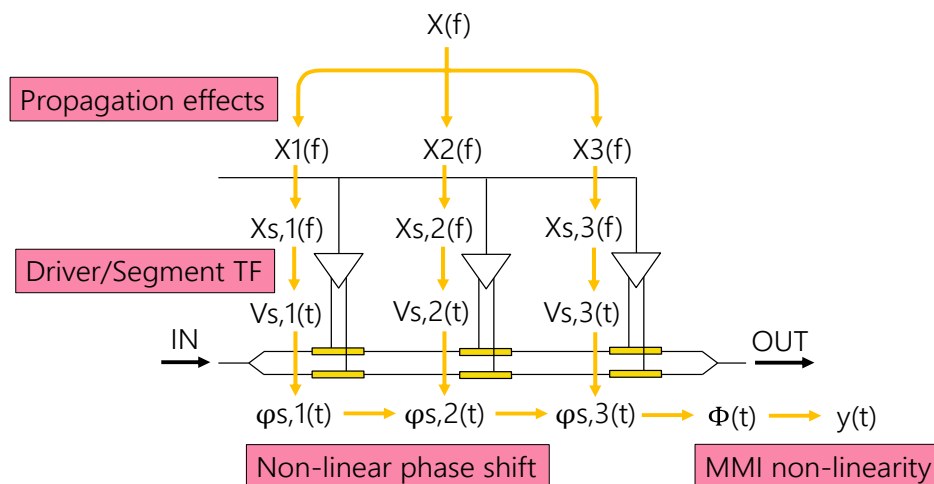


**Figure 3-15:** Schematic representation of the analytical model for a 3-segment SEMZM. The model is used to predict the large signal EO response of the modulator and extract the required RLC parameters for a target spectrum.

Multiple time-frequency transformations are performed in order to easily introduce and analyze the different effects that take place at different points in the modulator. The input

signal  $x(t)$  is moved into frequency space and copied as many times as the number of active segments  $N$ . In this way, each copy  $X_i(f)$  is individually modified in both amplitude and phase to implement frequency dependent propagation effects that take place during the transmission of the electrical signal within the IC chip, the most relevant of which are velocity mismatch and propagation losses. The different spectra are fed to the segments where they are shaped by the resonator transfer functions. The electrical signals  $X_{s,i}(f)$  are then brought into the time domain where the non-linear induced phase shifts are calculated according to a modified version of equation (2-1):

$$\varphi_{s,i}(t) = p_A V_{s,i}(t) + p_B V_{s,i}(t)^2 \quad . \quad (3-12)$$

In this equation, the time dependency of both  $\varphi$  and  $V$  is considered. The calculated phase shifts  $\varphi_{s,i}$  are summed up and associated with the optical wave that travels in the corresponding interferometer arm. The two optical waves are simultaneously fed to the input of the recombining 2x2-MMI. Finally, the signal at the selected modulator's output is plotted and once more brought into the frequency domain where the various  $Y(f)$  frequency components are visualized. The calculated resonators are placed and visualized in RLC space. The outputs of the large signal model include different quantities at different calculation steps, both in the time and frequency domains. Typical quantities of interest are the output eye diagram with the associated spectrum, and the corresponding RLC set (Figure 3-16).

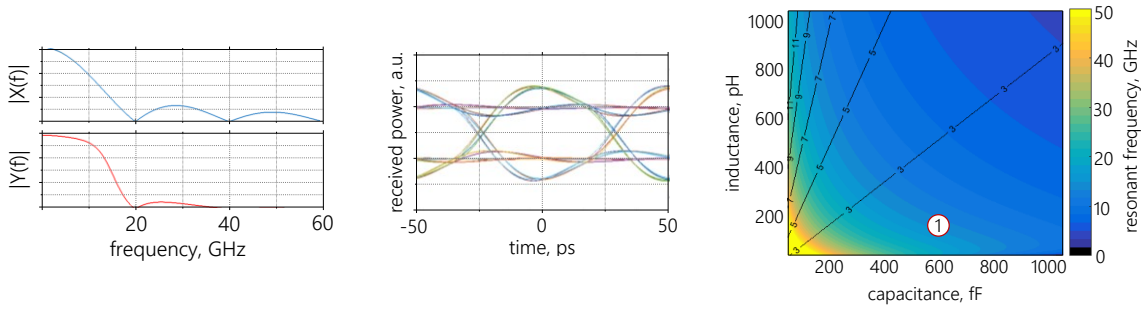


**Figure 3-16:** Single-resonator SEMZM model outputs. The 20 GBd PRBS input signal  $X(f)$  is shaped by a resonator with  $f_{e0} = 15$  GHz. The effect of the resonance is visible in the output signal spectrum  $Y(f)$  and the associated eye diagram. The resonator is placed in LC space, calculated, in this case, with  $R=10$  Ohm.

Rather than predicting the SEMZM output, the analytical model of the modulator is exploited to extract the RLC parameters of the individual segments, which, when combined, lead to the desired modulator's transfer function. For this purpose, the desired number of resonating segments and the applied voltage amplitudes are provided as model input. In Chapters 3.3 and 3.4, this model is used in the above sense while targeting different applications.

## 3.2.4. Optical Design

The need for segment's capacitances of different values translates to electrodes of different lengths and widths. As the electrode lengths are directly connected to the phase-shift induced in each section, the waveguide width  $w_w$  becomes an important degree of freedom for the design. Although wider waveguides correspond to larger capacitance values, the employed InP deeply-etched ridge waveguide allows for the propagation of high-order modes above the critical width of  $1.8 \mu\text{m}$ . The integration of different waveguide widths in the same modulator entails the need for tapering structures in between consequent active sections and along the individual interferometer arms. An abrupt transition in the propagation layer not only causes optical power losses and reflections, but also causes energy to be transferred to different guided modes [55]. The energy of non-fundamental modes is later lost in the recombining MMIs and should for this reason be minimized [56].

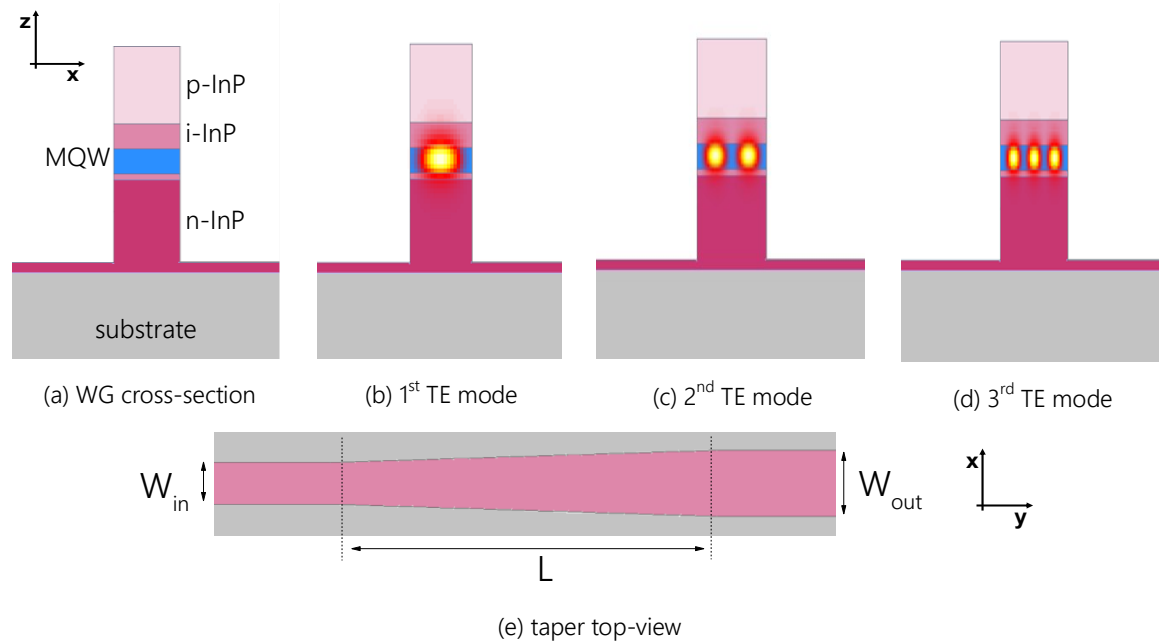


**Figure 3-17:** Simulated InP WG cross-section with its first guided TE optical modes (a-d) and tapering structure (e). The vertical center of the optical modes is aligned with the MQW. The 1<sup>st</sup> and 3<sup>rd</sup> TE modes are symmetric in the X-direction, whereas the 2<sup>nd</sup> is anti-symmetric.

The deeply-etched InP waveguide layer stack is implemented in the optical simulator. Each waveguide element is defined by its geometry and refractive index and faithfully reproduces the fabricated structures. The first guided transverse-electric (TE) modes position themselves in the MQW region because of the higher refractive index (Figure 3-17).

The tapered waveguide is symmetric in the X direction. The mode conversion is thus expected to involve the third guided mode, rather than the second. This conversion is

quantified as the ratio between the optical power in the third mode and the one in the first mode, expressed in dB. This is investigated for a taper with input width of  $2\ \mu\text{m}$ . Both the structure length and its fanning, i.e.  $\Delta W = W_{\text{out}} - W_{\text{in}}$ , are varied (Figure 3-18). The simulation results show that a longer taper is required for larger width increases. An arbitrary design threshold of  $-20\ \text{dB}$  of energy in the high-order mode, i.e. 1% of energy lost in the fundamental one, is considered here. If the modulator's chip area is not a limiting-factor, a taper of length of  $200\ \mu\text{m}$  ensures the mode conversion is well below this threshold for any of the simulated  $\Delta W$  values.

Together with the segment's lumped circuit model, its EM simulations, and the analytical modeling of the complete SEMZM, the optical level simulations presented here above constitutes the last step required for the development of spectral shaping modulators.

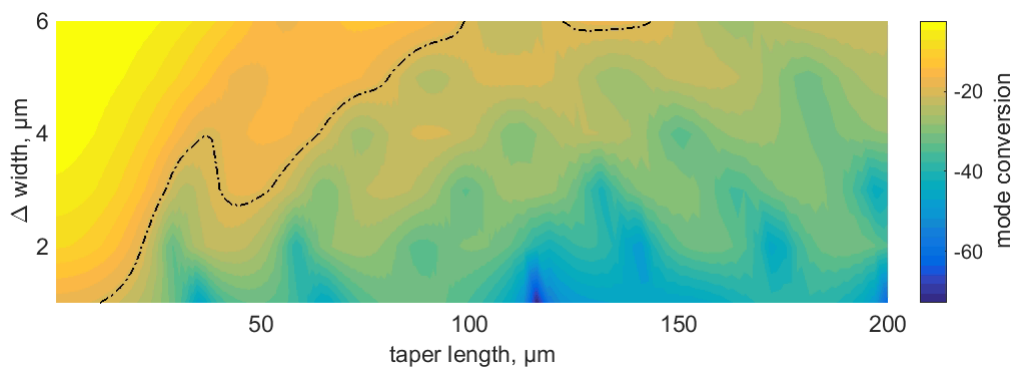


**Figure 3-18:** Mode conversion for tapers of different length and width increase  $\Delta W$ . The energy transfer to the 3<sup>rd</sup> mode increases quickly when the taper is short enough to make the transition abrupt. The contour line highlights the arbitrary threshold of  $-20\ \text{dB}$ .

### 3.2.5.Characterization

The segmented modulators are fabricated at the Fraunhofer Heinrich-Hertz-Institut (HHI) facility in Berlin, where an InP fabrication line that includes epitaxial growths, lithography as well as dry and wet etching processes is employed. After dicing and coating, the modulators are ready to be measured (Figure 3-19).

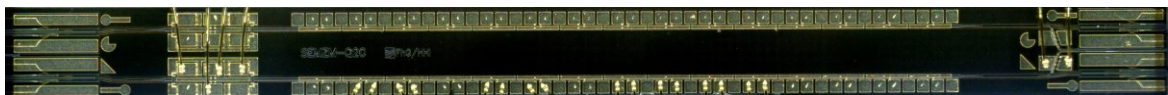


**Figure 3-19:** Micrograph of two fabricated SEMZM side by side. SSC are visible at the modulators' inputs and outputs. Biasing sections and metallized segments occupy most of the chip's length.

The SEMZM characterization starts with DC measurements. The goal of these measurements is to test which components are functional, both in the electrical and in the

optical domain. The electrical tests consist of the measurement of the various I-V characteristics for the pin diodes of the chips. This includes the active areas of the segments, the modulator's biasing sections and monitoring diodes, if present. The optical test consists of applying a voltage to the segments, which are shorted together. A voltage sweep is performed, and the light intensity at the output of the modulator is measured. In this way, the so-called DC-matrix of the modulator is obtained (Figure 3-20-a). This matrix provides information on the modulator's performance and allows for the extraction of extinction ratio, the minimum optical insertion loss and the switching voltage for different SEMZM operating points. A diagonal cut of the matrix represents the SEMZM high-frequency operation. This cut is called the RF-cut and is obtained at a specific modulator's bias (Figure 3-20-b).

The measured switching voltage is dependent on the specific design, in particular on the length of the active area. However, the modulation efficiency is renormalized to the active length and therefore becomes independent from it. For Fraunhofer InP SEMZMs, the measured ( $V_{\pi} \cdot L_a$ ) is around 0.3 V·cm at 8 V biasing voltage with a fiber-to-fiber IL below 10 dB for the whole C-band, depending on the specific chip design.

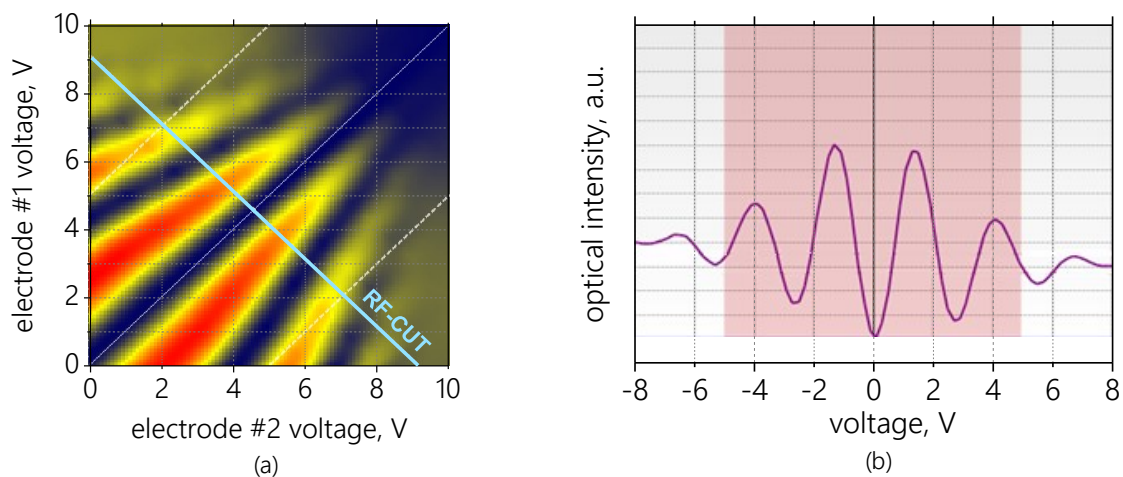


**Figure 3-20:** Characterization of the fabricated SEMZM: (a) DC-matrix and (b) RF-cut, i.e. a diagonal section of the DC-matrix representing a specific MZM working point.

The InP chips are employed for small-signal RF measurements. The single segments are characterized in a 2-port electro-optical setup, consistent with what was simulated in section 3.2.2. A Lightwave Component Analyzer (Keysight LCA-N4373B) is used. The individual SEMZM sections are put in contact with a single-ended signal-ground (SG) probe and are driven electrically. A 1550 nm external cavity laser (ECL) is used as the light source. The optical output of the modulator is simultaneously probed with the use of a lensed fiber that routes the light down to the optical port of the LCA (Figure 3-21). To maximize the EO energy conversion, the modulator is biased in the 3-dB point during the measurements. With setup calibration, the influence of the electrical and optical interconnections is de-

embedded and the individual segments of the resonant modulators are characterized. The measured  $S$ -parameters for a reference segment  $450\ \mu\text{m}$  long and  $2\ \mu\text{m}$  wide are plotted together with the corresponding simulated ones, extracted from fitting the equivalent circuit (Figure 3-22). The EO  $S_{21}$  phase is not reported, as it was not possible to de-embed the optical path outside the device under test (DUT).

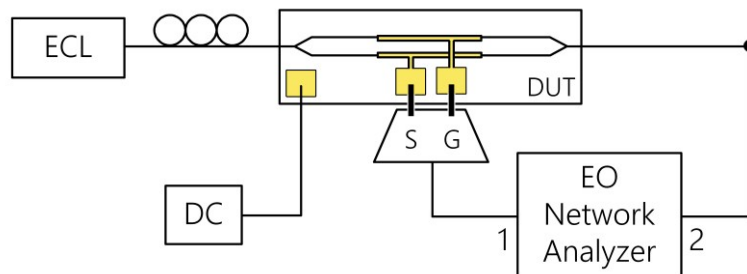


**Figure 3-21:** EO  $S$ -parameters measurements setup for the SEMZM segments. An EO network analyzer is employed to stimulate the segments' electrical inputs and probe the modulator's optical output.

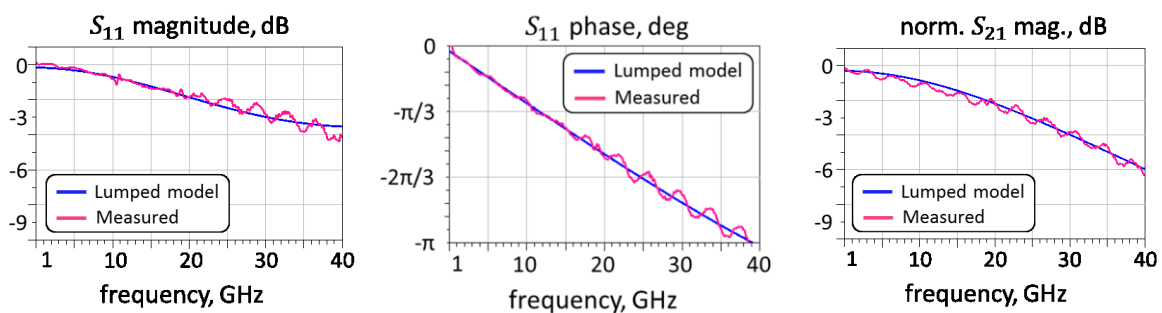


**Figure 3-22:** Comparison of measured and simulated EO  $S$ -parameters for the reference segment. The good agreement of both  $S_{11}$  and the magnitude of  $S_{21}$  prove the lumped model to be valid.

The lumped circuit curves are in very good agreement with the measured ones, with a maximum disagreement of less than 1 dB for the entire frequency range. This proves the circuit to be a valid tool to faithfully model the segments' EO behavior up to 40 GHz. For the reference segment, the RLC parameters extracted out of the measured small-signal curves are  $C_{MZ} \approx 250\ \text{fF}$ ,  $L_{MZ} \approx 65\ \text{pH}$  and a  $R_{DC} \approx 4\ \Omega$ . The relative difference with the simulated parameters ( $C_{MZ} \approx 230\ \text{fF}$ ,  $L_{MZ} \approx 65\ \text{pH}$ ,  $R_{DC} \approx 1\ \Omega$ ) is very small, except for the DC resistance value. This can be explained by the non-precise modeling of the conductor and interface resistance in the EM simulator. In addition, the de-embedding of the electrical cables and the RF probe introduces a non-negligible uncertainty for the measured values.

The EO peaking of the resonating structure is not visible in the magnitude of the reported  $S_{21}$  since the contribution to inductance from the assembly interconnections is not included. For spectral shaping purposes, the resonance must be moved into the working frequency range and this extra inductance is required. To investigate the resonance, a

segmented MZM comprising 15 identical segments with  $C_{MZ} \approx 200$  fF is assembled on a PCB and gold wires with a  $17 \mu\text{m}$  diameter, but different lengths are employed to connect the individual sections to landing pads for the RF probe (Figure 3-23).

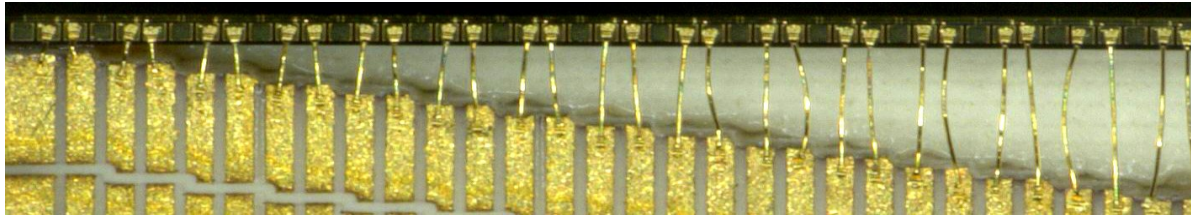


**Figure 3-23:** Top-view detail of a 15-segment SEMZM. The segments are bonded to a PCB with gold wire pairs of different lengths, from  $160 \mu\text{m}$  to  $860 \mu\text{m}$ . The InP chip segments are identical.

The S-Parameters of the different segments are measured again, but this time probing the PCB, rather than directly the segments' pads. The EO S-parameter magnitude shows a clear resonance peak, as expected from the simulations (Figure 3-24). Different resonance frequencies and quality factors are measured, depending on the bondwires' length. The highest measured resonance frequency is  $19 \text{ GHz}$  with a  $Q = 1.2 \text{ dB}$  for a bondwire length of  $360 \mu\text{m}$ . Shorter bondwires result in over-damped resonators with  $Q < 1$ . The longest bondwire,  $860 \mu\text{m}$ , achieves the lowest  $f_{e0} = 14.5 \text{ GHz}$  with  $Q = 4.3 \text{ dB}$ . The measured values are consistent with a vertical movement in the calculated LC space.

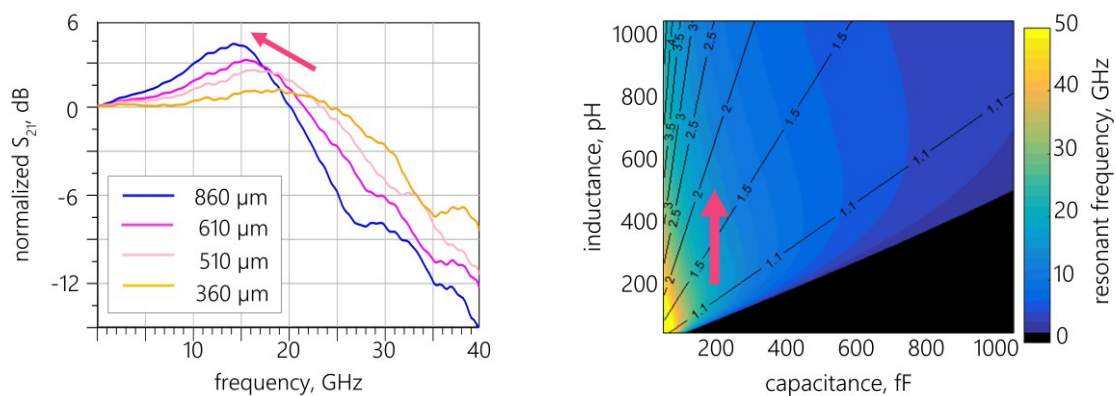


**Figure 3-24:** Normalized measured EO transmission S-Parameter for 4 segments with different bondwire length and the correspondent movement in the calculated LC space. The resonance frequency and the Q factor both depend on the bondwires length.

With the small-signal EO measurements and the proven consistency between the various design steps, the whole design process is validated. The characterized modulators are ready for field-testing, i.e. large signal measurements. However, depending on the foreseen application, specific design choices need to be taken. For this reason, the following sections

present specific design decisions for specific applications before discussing the large signal measurements.

#### 3.3. Bandwidth Enhancement by Frequency Equalization

The resonance of the SEMZM is exploited to enhance the bandwidth of the entire electro-optical system: the modulator itself, along with the electronics employed to drive it, e.g. data sources, DACs, and driver amplifiers. As introduced in section 3.1, the target application is the transmission of a 56G OOK signal using driving electronics whose 3 dB cut-off frequency is lower than half the symbol rate. The resonance peak of the SEMZM is thus designed to be at 28 GHz. The quality factor of the resonance is ideally such as to exactly compensate for the losses of the surrounding components. Since these losses are unknown, a quality factor appropriate for a flat transfer function at the electronics' cut-off frequency, here half the baud rate, is selected.

When the segment is driven in a  $50 \Omega$  environment, each modulator's arm is loaded with half the source resistance. An additional  $5 \Omega$  must be added in order to account for the additional series resistance of the SEMZM. The total damping resistance is thus  $30 \Omega$ . With such a load, the region of interest in LC space regions of interest are pushed to areas with small capacitive loads of about 100 fF (Figure 3-25-a).

As discussed in Chapter 3.2.1, this capacitance is a function of the segment's length and therefore connected to the modulation efficiency. A larger  $C_{MZ}$  is thus advisable in order to lower the segment's drive voltage. For this reason, a high-frequency resistor  $R_p$  is placed in parallel with the source resistance, at the segment's input. The effect of this resistor is to lower the resonator loading resistance. Therefore, the region of interest is shifted towards the right, i.e. towards regions associated with larger capacitance values (Figure 3-25-b).

With known target RLC parameters, the development of the SEMZM continues as already discussed. A segmented modulator with 16 identical sections of length  $225 \mu\text{m}$  is designed and fabricated. The number of segments is maximized in order to achieve lowest possible switching voltage. DC characterization is performed and the fiber-to-fiber insertion loss is measured to be 8.5 dB at 1550 nm. When all the segments are connected together, a  $V_\pi = 1 \text{ V}$  is measured, resulting in a modulation efficiency of  $0.36 \text{ V}\cdot\text{cm}$  and a  $(V_\pi \cdot \text{IL})$  product as low as 11.6 V·dB at the best biasing condition. The working SEMZMs are assembled on a PCB where four segments are provided the necessary additional inductance by means of  $175 \mu\text{m}$  long gold bondwires. Supplementary  $50 \Omega$  tapers are designed in order to fit the  $39 \Omega$  RF resistors and match the pitch of the available 4 x SG RF probe (Figure 3-26). The number of assembled segments is equal to four only because that was the number of RF data lines that could be provided to the modulator with the correct time delay.

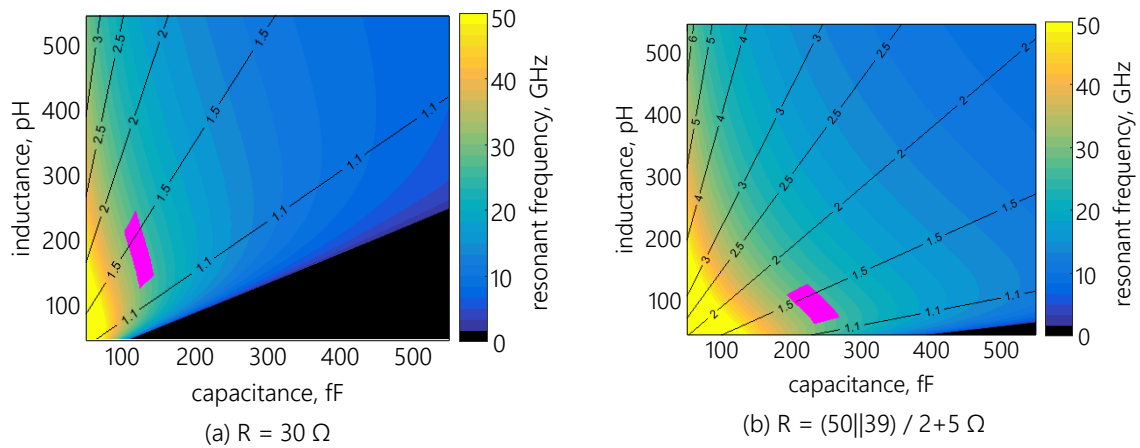


**Figure 3-25:** Resonators in LC space for two different loading resistances: (a)  $30 \Omega$  and (b)  $16 \Omega$ . The areas of interest for the 56G OOK bandwidth enhancing application are highlighted in magenta.

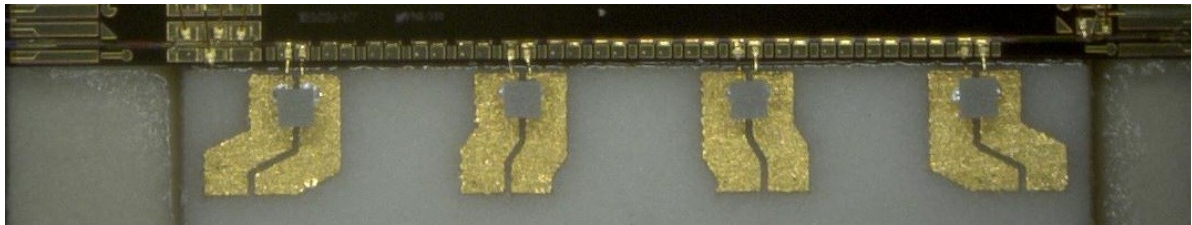


**Figure 3-26:** Bandwidth enhancing SEMZM with 4 assembled segments. The segments are  $225 \mu\text{m}$  long and are provided with the required additional inductance with a pair of  $175 \mu\text{m}$  long gold wires. Small-size RF resistors are employed to lower the source loading impedance.

The equivalent circuit of the assembled single-ended segment's branch with a RF resistor in parallel is depicted in Figure 3-27-a. The small-signal EO parameters are measured for each of the four segments in the same setup as shown in Figure 3-21. The comparison between the simulated transfer function and the measured one shows good agreement (Figure 3-27-b). The measured resonance frequency is  $32 \text{ GHz}$  with a quality factor  $Q = 4.5 \text{ dB}$ . The difference from the desired value is attributed to difficulties in controlling the bondwire inductance value and an imprecise estimation of the  $R$  and  $C$  parameters. Despite this, the obtained transfer function serves well for the foreseen application, since the peak at  $28 \text{ GHz}$  is not far from  $3 \text{ dB}$ .

Large-signal measurements are performed by simultaneously driving three segments of the SEMZM (Figure 3-29). Only three segments are driven because of the limited availability of RF filters. A  $56 \text{ Gb/s}$  OOK PRBS signal is generated with a four-channel bit pattern generator (BPG) whose outputs are fed to high bandwidth SHF drivers through the Bessel-Thomson filters. The drivers are then connected to the segments of the modulator.

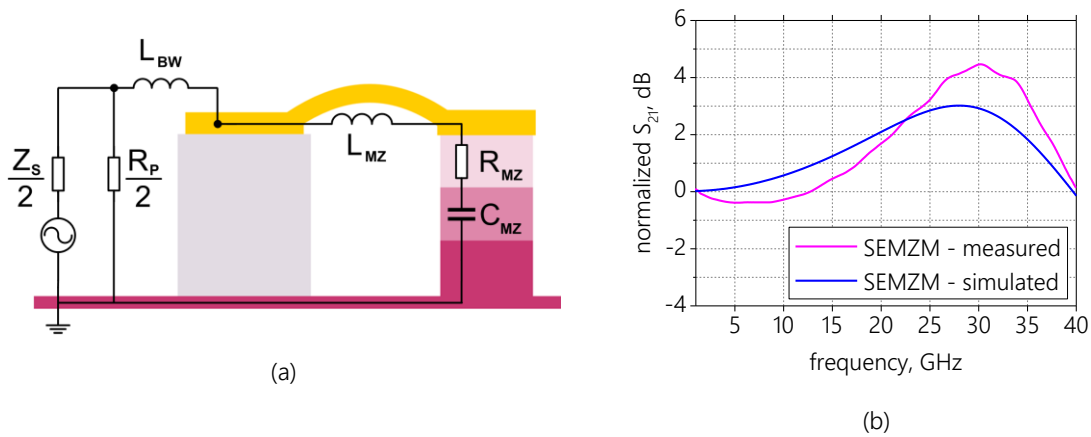


**Figure 3-27:** (a) Equivalent lumped model of the assembled segment's branch including the parallel resistor  $R_P$  and (b) comparison of the small-signal measured and simulated EO parameters' amplitude.

As the three sections are independently driven, the signal path is repeated three times. Electrical delay lines are also included before the modulator to synchronize the signal on the different segments with the optical wave. The optical path starts with a 1550.1 nm ECL whose output is fed directly into the SEMZM through a lensed fiber. The optical output of the MZM is then amplified with an erbium-doped fiber amplifier (EDFA) and sampled with an optical oscilloscope.

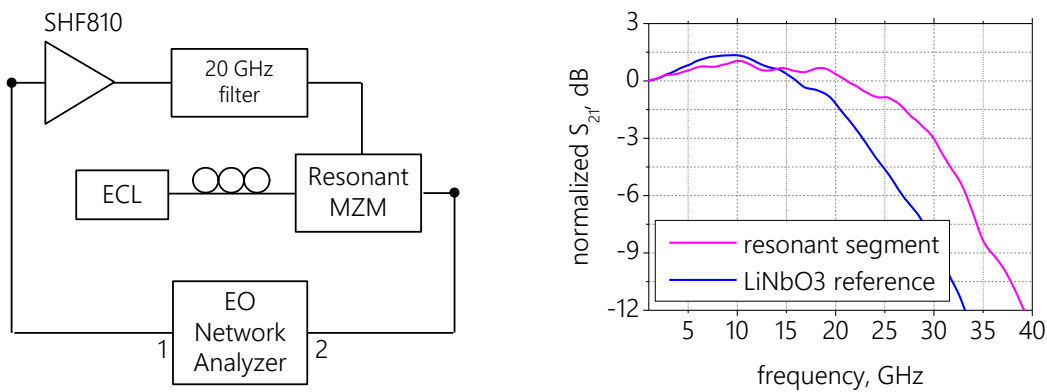


**Figure 3-28:** Small-signal measurement setup for the bandwidth enhancing SEMZM. Slow electronics is emulated using a Bessel-Thomson filter with 3 dB bandwidth of 20 GHz. The normalized  $S_{21}$  amplitude shows the 7 GHz bandwidth gain with respect to a LiNbO3 MZM reference.

The obtained 56 Gbd eye diagram shows a clear opening at the measured data rate despite the bandwidth limitation of the driving electronics (Figure 3-30). The measured ER is 8.6 dB, limited by the short modulation length equal to only 675  $\mu\text{m}$ . Driving a higher number of segments, a higher ER is to be obtained. As a comparison, the resonant SEMZM is replaced once again with the LiNbO3 reference and an open, but noisier eye diagram with ER = 10.7 dB is obtained.

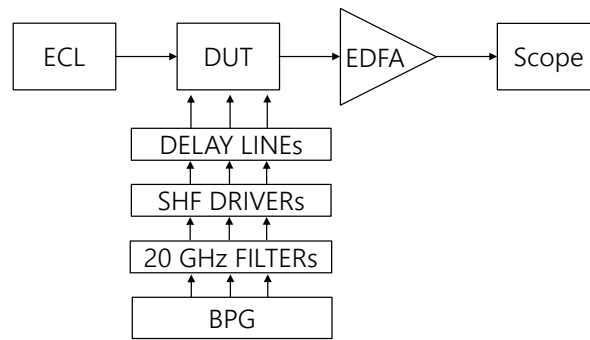


**Figure 3-29:** Large-signal measurements setup for the 56 Gbd bandwidth enhancement experiment. Three segments are simultaneously driven with a properly timed OOK signal.

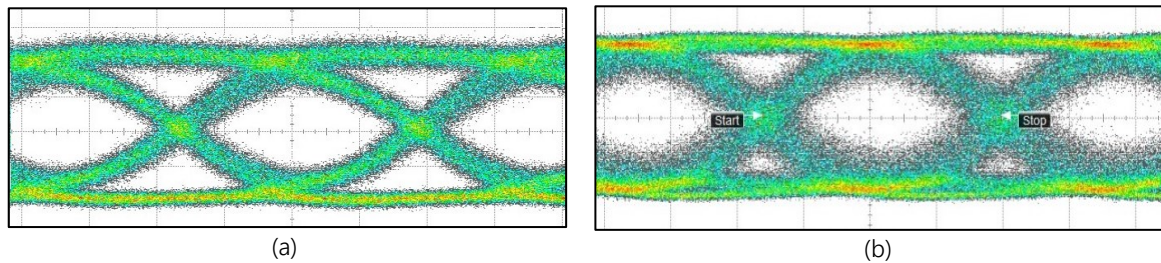


**Figure 3-30:** Measured 56 Gbd OOK optical eye diagrams for (a) the resonant SEMZM and (b) the Sumitomo LiNbO3 MZM reference when driven by 22 GHz bandwidth electronics.

Bit error ratio is measured over channel-induced dispersion. The dispersion is introduced in the setup with a tuneable dispersion compensator, inserted before the optical receiver. The BER curves are measured for both the InP SEMZM and the LiNbO3 MZM (Figure 3-31). The InP resonant modulator transmits the 56 Gbd OOK signal with a BER lower than  $10^{-9}$  over the equivalent of more than 2 km of fiber. The measured BER is below the hard-decision forward error correction (HD-FEC) threshold, i.e.  $3.8 \cdot 10^{-3}$  with 7% overhead, up to 4.5 km of channel length, assuming a dispersion per kilometre of single mode fiber of 17 ps/nm [57]. The BER curves are also measured versus optical signal-to-noise ratio (OSNR) to evaluate the impact of noise over the modulated signal. The OSNR is varied with the usage of an EDFA and a variable optical attenuator (VOA) inserted directly after the modulator. The measured BER is below the HD-FEC threshold for OSNR larger than 27 dB, whereas the LiNbO3 reference system never reaches this threshold. The higher noise-floor visible in the BER vs OSNR measurements is to be attributed to the different setup including the extra noise loading stage. In both comparisons, the resonating SEMZM performs better since the reference system does not have the bandwidth to transmit the signal error-free.

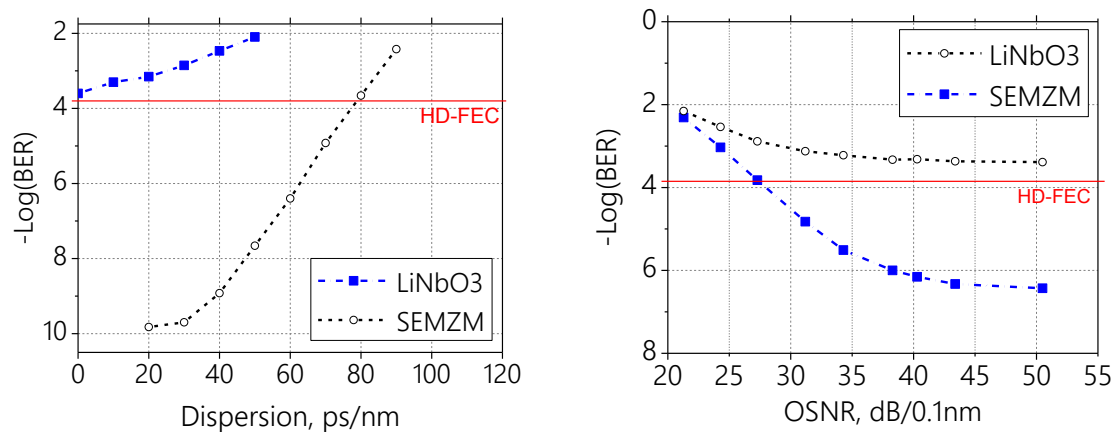


**Figure 3-31:** 56 GBd BER measurements for the resonating InP SEMZM and the LiNbO3 reference when driven by 20 GHz bandwidth electronics. Scatter points represent the measured values.

### 3.4. Nyquist-space Spectral Shaping

Together with the transfer function peaking, the steep attenuation edge above the resonance frequency offers the possibility to attenuate specific signal components. As introduced at the beginning of the chapter, this spectral shaping performed by the SEMZM is employed to reduce the spectral width of the modulated signal and minimize the ICI. The goal is to obtain a Nyquist shaped signal at the modulator's output without the usage of any DAC or DSP on the transmitter side. The baseband spectrum of a 40 GBd PRBS signal has its first zero at 40 GHz. However, the corresponding ideal 40 GBd Nyquist shaped signal exhibits a rectangular power spectrum with a width of only 20 GHz, when the shaping roll-off  $\beta$  is equal to zero (Figure 3-32). With this target, the SEMZM transfer function (TF)  $H(f)$  is not only required to cut off spectral components above half the baud rate frequency, but also to enhance those components just below it, resulting in the peculiar shape of Figure 3-32-b. The envelope of the magnitude spectrum of a PRBS equals  $2/\pi$  at half the baud rate and the required TF peak is thus  $\pi/2$  at this frequency. However, when multiple segments work together, this peak must be reached as an overall value so the individual Q factors may differ. The attenuation edge above the resonance is a function of the segments' Q factor. Resonators with a larger Q show a steeper edge, at the cost of a narrower resonance bandwidth. Aiming for a specific shape of the transfer function over frequency makes it somewhat more complicated to design the spectral shaping SEMZM with respect to its bandwidth-enhancing counterpart. The solution comes from the simultaneous driving of multiple segments that resonate at different frequencies and with different quality factors. The output signal spectrum is dependent on these resonator properties and their number. The required resonator RLC parameters are calculated with the SEMZM analytical model, starting from the aimed target function (Figure 3-33).

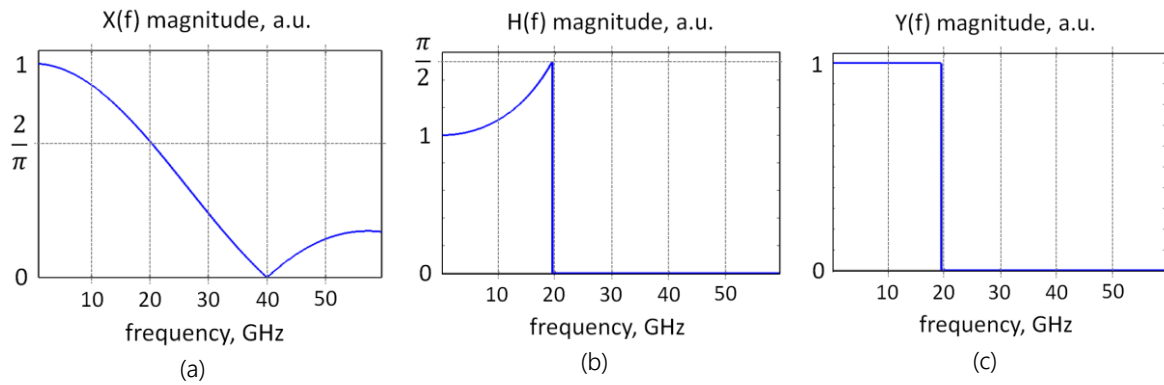


**Figure 3-32:** Simulated spectrum of the 40 Gb/s PRBS input signal (a), segmented modulator's transfer function (b), and simulated spectrum of the output optical signal halved and brought to baseband (c).

With this simulation tool, an optimization is performed and the ideal set of resonators is selected. Capacitance and inductance values that approach the borders of the feasibility range are avoided thanks to the series resistors of the segment  $R_{MZ}$  and parallel RF resistors  $R_p$ . These resistors may differ from one segment to another and thus add degrees of freedom in the design of the different resonators. The output signal spectrum and the corresponding eye diagram are also simulated. The difference between the simulated eye diagram and the one of a Nyquist-shaped signal is explained by the dissimilarity of the signal spectra. The attenuation edge is not as steep as that of an ideal rectangular Nyquist-shaped signal and the envelope is not precisely that of a raised-cosine function. The energy tail above the last resonance frequency degrades the quality of the output signal, broadening its spectrum, and distancing it from its ideal rectangular counterpart. Although this energy portion can be minimized with proper resonators choice, it cannot be brought to zero.

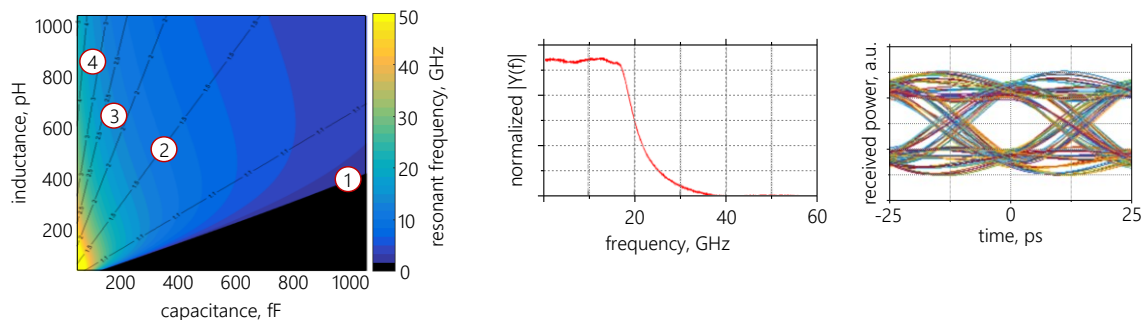


**Figure 3-33:** LC map for the 4-segment spectral-shaping resonant SEMZM with  $R = 29 \Omega$  and the corresponding output spectrum and eye diagram. The numbered points indicate the target position for the resonators, which together output the aimed spectrum.

A way to remove the resonance tail and steepen the attenuation edge consists of the usage of a short transmission line inserted in parallel with the resonating modulator's

segment (Figure 3-34-a). This transmission line, called resonant stub, is connected at only one end [58]. The unloaded stub is designed with a length equal to  $\lambda/4$  for the specific frequency  $f_{\text{stub}}$ . At the stub resonance frequency, the high impedance of the open stub end results in a low input impedance. Neglecting line losses, the impedance seen at the stub inputs is therefore ideally equal to zero. The effect of the stub is to cause a drop of the voltage over the modulator at its resonance  $f_{\text{stub}}$ , thus introducing a steep fall in the electro-optic TF of the segment (Figure 3-34-b). The total assembled SEMZM transfer function is a combination of the two resonance frequencies, the one of the modulator  $f_{\text{eo}}$  and the one of the stub. Different shapes and different corresponding roll-offs are obtained for stubs of different lengths. The tuning of the two resonance frequencies allows for the design of a wide range of different nearly rectangular output optical spectra. The assembly frequency behavior can be precisely simulated with a joint model of the modulator's segment and the associated stubs. However, for small values of loading resistance the two can be thought of as independent, allowing a low-complexity design procedure. Another important parameter is the sideband suppression ratio. This parameter expresses how much lower the magnitude of the frequency components above  $f_{\text{stub}}$  is than that of the components beneath  $f_{\text{eo}}$ . The suppression ratio is not only a function of the stub length, but of its characteristic impedance as well. Proper design ensures suppression larger than 20 dB with a steep attenuation edge. With the use of the resonant stub, an output signal spectrum close to the rectangular ideal is obtained, even with the use of a single peaking segment.

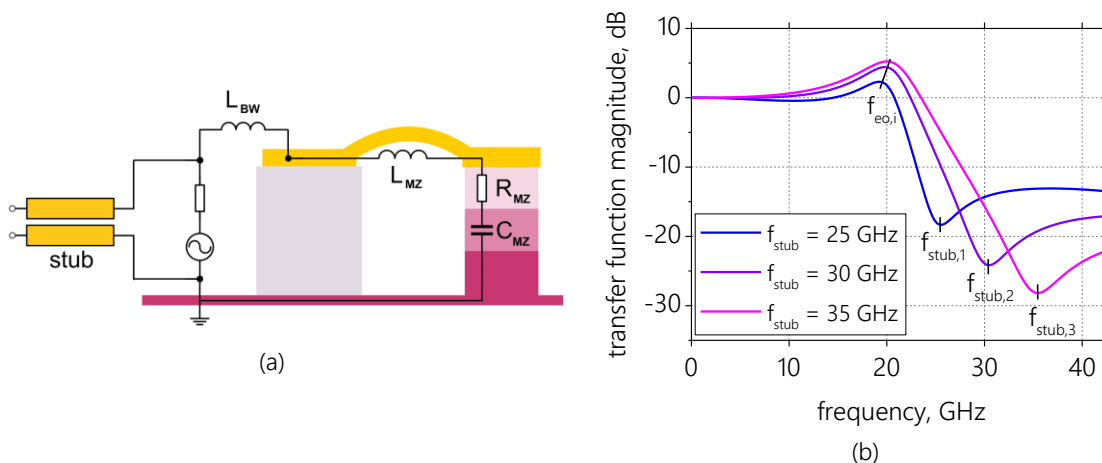


**Figure 3-34:** (a) Cross-section of the SEMZM segment and its equivalent electrical model with driving configuration and parallel resonant stubs and (b) simulated EO transfer functions for different stubs.

After fabrication in HHI, the resonant SEMZM is assembled on an AlN ceramic substrate (Figure 3-35). Two segments both 370  $\mu\text{m}$  long, one 1.4  $\mu\text{m}$  and the other 2.3  $\mu\text{m}$  wide, are bonded to the ceramic with gold wires of 950  $\mu\text{m}$  and 700  $\mu\text{m}$  length respectively. The parallel resonant stubs are realized on the ceramic in a coplanar stripline configuration. The two stubs are 1650  $\mu\text{m}$  and 1300  $\mu\text{m}$  long. The assembled structure is driven one segment

at a time with a SG probe placed at the input of the stub, close to the bondwires' landing point. In the measured EO S-parameter's magnitude, both the segment's and the stub's resonances are visible. The two segments' shaping differences result in different measured peaking amplitude and the stub resonance frequency. Consequently, different roll-off factors are obtained. The overall shape is close to the target one with a measured magnitude peak of 4.2 and 2.2 dB,  $f_{\text{stub}}$  equal to 23.3 GHz and 31 GHz, and a suppression factor larger than 10 dB for the first segment and 20 dB for the second one. Comparing the measured curves with the target modulator's TF, the first segment's small-signal response better approaches the target Q-factor and exhibits a steeper attenuation edge. However, this segment exhibits a limited suppression factor.

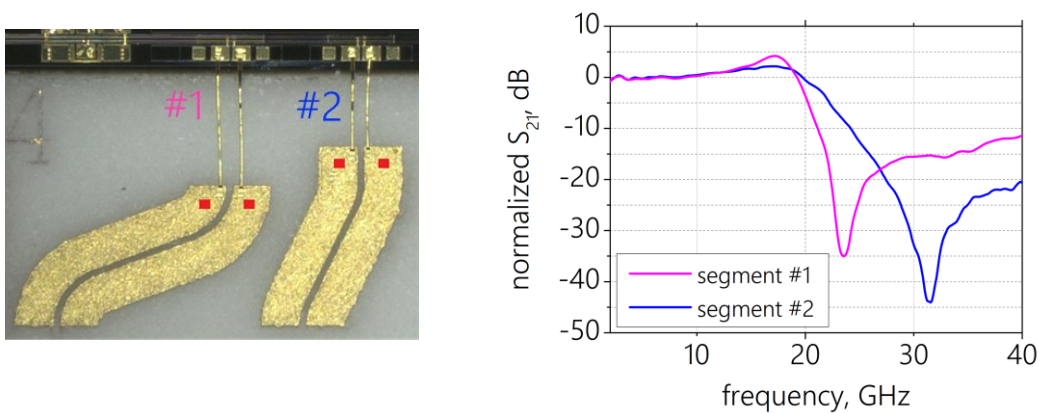


**Figure 3-35:** Resonant segments assembled on an AlN substrate where parallel resonant stubs are placed. The red dots indicate the probe landing positions. The measured EO small-signal transmission parameters incorporate both the segment's and the stub's resonances.

The two segments are driven one at a time in a large-signal setup. An OOK PRBS stream is generated with a BPG, and a broadband commercial amplifier is employed to deliver enough voltage to the sections. A 6 dB attenuator is inserted at the amplifier output in order to protect it from power reflections generated by impedance mismatch. A 1550 nm ECL is used as the optical source. The modulator's output is probed with a sampling oscilloscope and an optical spectrum analyzer. The back-to-back (B2B) eye diagrams and the correspondent optical spectra are measured in this way (Figure 3-36-a and Figure 3-36-b). The received eye diagrams show the characteristic envelope of Nyquist shaped OOK signals. Additionally, the optical spectra show clipping at half the bitrate. As expected, the segments' different TFs result in different optical spectra, with the first segment showing a steeper attenuation edge. The equivalent roll-off factors are extracted by fitting the raised-cosine function for a 40 GBd signal to the measured optical spectra. The first segment achieves the lowest roll-off, equal to just 0.15, but a frequency offset for the falling edge is visible. Because of this offset, the best eye opening is obtained when the data input is a

35 GBd signal. The second segment has a roll-off factor of 0.35 and a falling edge that is in the right position. Thus, an open eye is obtained when driving the segment at 40 GBd.

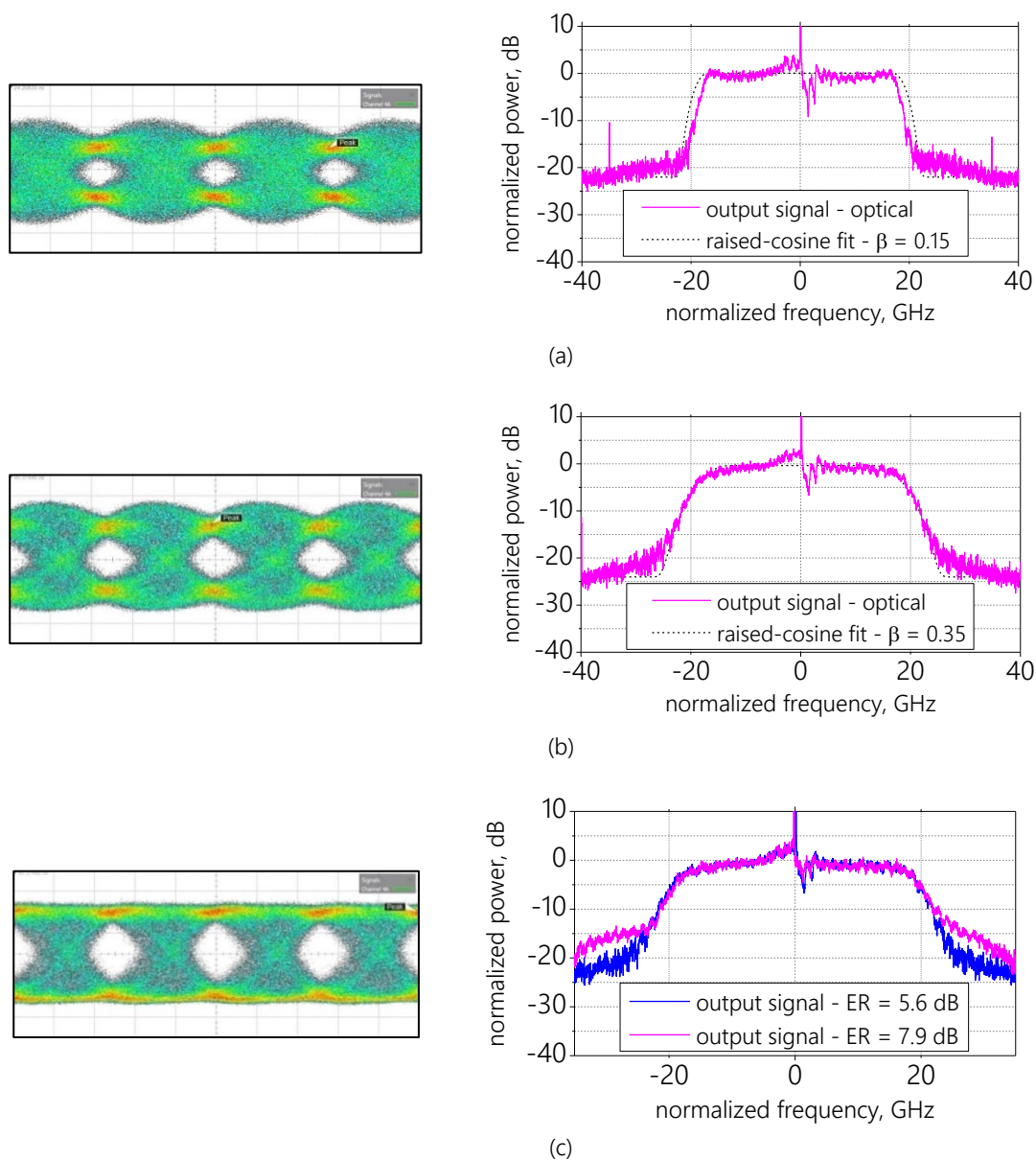


**Figure 3-36:** OOK eye diagrams and spectra of the (a) resonant segment #1 with 1650  $\mu\text{m}$  long stub driven at 35 GBd and (b) resonant segment #2 with 1300  $\mu\text{m}$  long stub at 40 GBd. The fitting roll-off factors are 0.15 and 0.35 respectively. In (c), the signal's transitions of segment #2 are compressed to maximize the ER.

A non-negligible transient chirp is observed in the modulated signal spectra as the non-symmetric feature located close to the optical carrier. The reason for this is the high voltage that is fed to the short segments in order to obtain a clear eye opening. With this high voltage, the linear approximation of equation (2-1) no longer holds, and phase-modulation of the output signal is introduced [18]. However, the impact of this chirp is dependent on the driving condition and does not constitute a limiting factor under the real operating

conditions of the SEMZM, as described in the following section. The measured eye extinction ratios are 5.6 and 3.9 dB. These values are not limited by the design of the modulator but are intrinsically constrained by the TF room that is to be left free for the Nyquist-eye overshoots. This extra space is not required for standard OOK modulation, where the non-linearity of the MZM transfer function can be exploited to reduce the intensity level noise: with proper SEMZM bias, the transition overshoots are pushed to the extremes of the TF and thus compressed. When this is performed, an enhanced ER of 7.9 dB for segment #2 is obtained, at the cost of the introduction of harmonic components that result in increased side-lobes in frequency domain (Figure 3-36-c). Whether the ER or the minimization of the out-band power should be prioritized is decided for the specific application.

The spectral shaping performed by the InP segmented modulator becomes clearly visible when the optical output spectrum is compared with the electrical input spectrum (Figure 3-37).

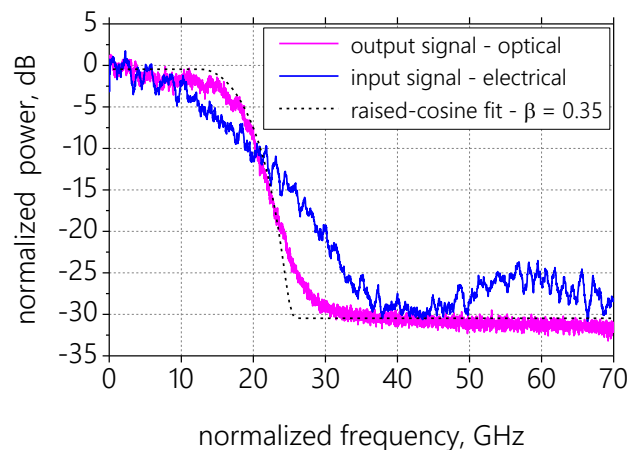


**Figure 3-37:** Comparison between the electrical 40 GBd 2-ASK-2-PSK input signal spectrum and the optical spectrum at the resonant SEMZM output, halved and brought to baseband. Both frequency emphasis and attenuation are performed by the SEMZM in the analog domain without any DAC.

In this setup, a 40 GBd 2-ASK-2-PSK signal is passively generated by combining two BPG channels, one of which is attenuated by 6 dB. Firstly, the BPG signal spectrum is detected with an electrical spectrum analyzer. Secondly, the same signal is fed to the resonant SEMZM segment and the optical output spectrum is measured. The Nyquist-like shape of the output spectrum is visible and the two effects provided by the resonant SEMZM can be seen. The resonant SEMZM pre-emphasizes the frequencies below 20 GHz, i.e. half the symbol rate, thus reducing the impact of noise on these frequency components and the consequent equalization-induced noise enhancement. In addition, it steeply attenuates frequencies above 20 GHz, narrowing the bandwidth occupied by the signal. As previously

discussed and simulated, the former effect is attributed to the segment's resonance, whereas the latter is due to the combination of both the segment and the stub itself. The optical spectrum is compared with an RC function, which fits best with a roll-off factor of 0.35. Thanks to the reduced bandwidth of the modulated signal, the SEMZM allows for dual-carrier transmission with minimized cross talk, suited to a Nyquist-WDM scenario with 50 GHz spacing. As previously mentioned, no DSP is used for spectral shaping.

#### 3.4.1. Dual-carrier Dual-polarization 40 GBd 2-ASK-2-PSK

The assembled resonant SEMZM with its stub provides a Nyquist-like spectral shaping that is suitable for WDM transmission links. In order to prove the concept and quantify the ICI between two spectrally shaped channels, a transmission experiment is here performed. For this experiment, a 40 GBd 2-ASK-2-PSK electrical signal is generated, as described in the previous section, and fed into the SEMZM (Figure 3-38). Due to the availability of only a single resonant modulator, two ECLs with a frequency spacing of 50 GHz around 1550 nm are combined with a 3 dB coupler and are fed into the SEMZM. The spectral shaping performed by the modulator suppresses the crosstalk otherwise induced by the joint modulation of the two carriers. To de-correlate the two carriers before transmission, a pair of Optoplex 100-200 GHz interleavers is used, with an additional 5 m fiber inserted in the path of one channel. Compared to using an arrayed waveguide grating, using an interleaver guarantees that no spectral component of both input wavelengths is suppressed. Subsequently, the signal travels through a polarization multiplexer (MUX), again including a 2.6 m fiber in the light path of one polarization for de-correlation. The light then goes through 80 km of standard single-mode fiber (SSMF) at a launch power set to 0 dBm by using an EDFA. The received OSNR is varied with a noise loading stage composed as previously described. The detection is performed with a polarization-diversity coherent receiver. After the signal is digitized at 80 GS/s with a real-time sampling oscilloscope with 33 GHz analog bandwidth, it is processed offline. The DSP, developed by the Photonic Networks department at Fraunhofer Heinrich-Hertz-Institut, includes frontend correction, data-aided carrier frequency recovery and channel equalization, chromatic dispersion compensation, Viterbi-Viterbi carrier-phase recovery, and bit-error counting. The received optical spectrum for one polarization of the detected signal shows the two 40 GBd carriers standing nearby with a spacing of only 50 GHz (Figure 3-39). This narrow spacing is enabled by the spectral shaping performed by the SEMZM.

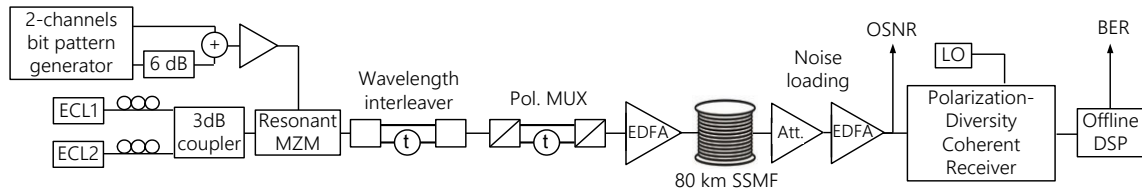


**Figure 3-38:** Experimental setup for the 40 Gbd dual-carrier dual-polarization 2-ASK-2-PSK transmission measurements. 80 km of SSMF are inserted between the transmitter and the receiver.

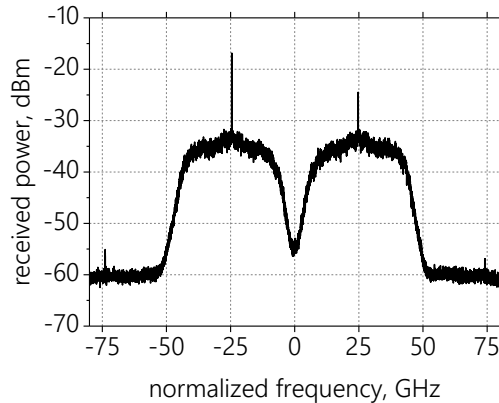


**Figure 3-39:** Measured spectra for one polarization of the two 50 GHz spaced carriers. Center is at 1550.62 nm. This close spacing is enabled by the resonant SEMZM shaping.

The BER is measured as a function of OSNR. In principle, the two carriers can be detected simultaneously with the use of a single broadband receiver. However, due to the limited bandwidth of the receiver available for this experiment, only one subcarrier at a time is detected. To investigate the cross talk between the two carriers, the BER curves are measured both with and without the adjacent 50 GHz-distant subcarrier, considered to be the aggressor (Figure 3-40).

The constellations before decision at maximum OSNR show the distinguished 2-ASK-2-PSK symbols. Thanks to the analog DAC-free spectral shaping performed by the resonating SEMZM, the cross talk between the two subcarriers is minimized. For both carriers, the influence of the adjacent subcarrier is negligible, with no significant penalty in the BER that could be measured at the chosen channel spacing of 50 GHz. For an OSNR larger than 23 dB the BER curves are below the FEC threshold (HD-FEC with 7% overhead) and can therefore be transmitted error-free. With a gross data rate of 320 Gb/s transmitted over 100 GHz bandwidth, the spectral efficiency equals 3.2 b/s/Hz.

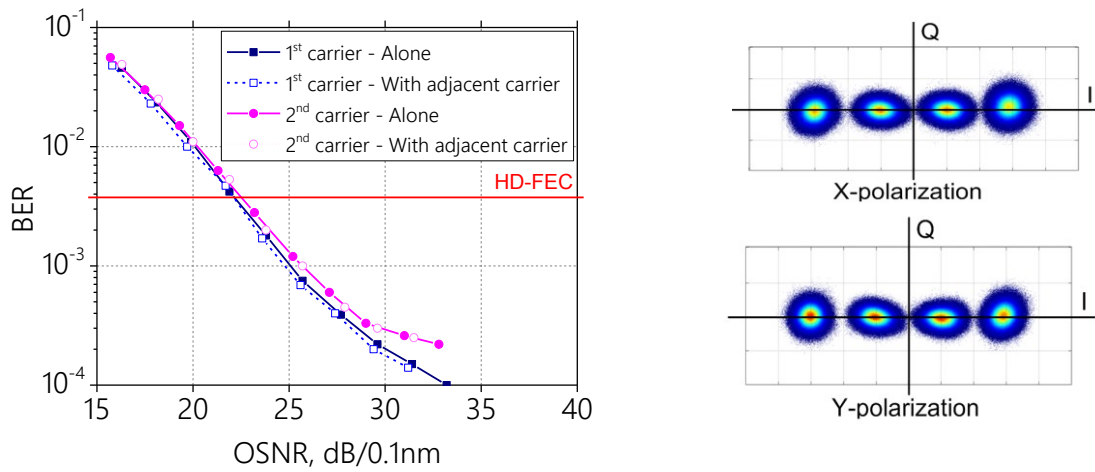


**Figure 3-40:** Measured BER versus OSNR after 80 km of SSMF for the two subcarriers, both when transmitted alone and together with the 50 GHz distant adjacent carrier and constellation diagrams of one 2-ASK-2-PSK modulated carrier at maximum OSNR. No penalty is observed when activating the adjacent carrier. Plotted points represent the measured values.

## 4. SEMZM for Optical-DAC

### 4.1. Introduction

The transmission of M-PAM or M<sup>2</sup>-QAM modulation schemes requires the children MZMs of an IQ-modulator to be driven with M-level electrical signals. In current networks, these signals are typically generated with electrical DACs. These components combine multiple bit streams into a multilevel analog signal that is first amplified by linear drivers and then fed to the MZ modulators (Figure 4-1). The concurrent modulation of the optical signal's amplitude and phase generates complex modulation formats, as discussed in chapter 2.

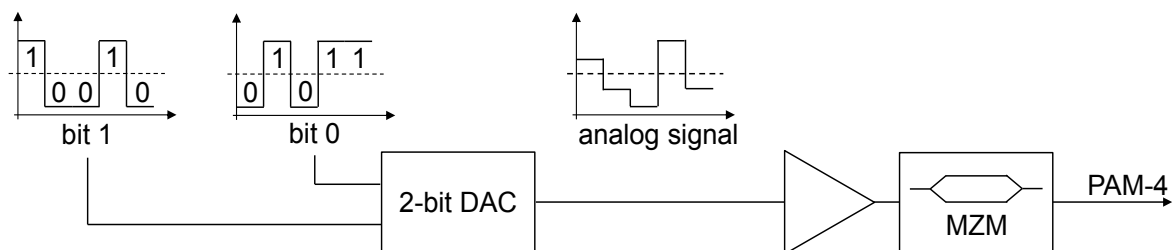


**Figure 4-1:** Digital-to-analog conversion of the MZM input signal for 4-PAM modulation. An electrical DAC is employed to generate the multilevel signal and an electrical linear driver to amplify it.

The drawbacks associated with DACs, i.e. large size and high power consumption, together with limited resolution, makes it desirable to explore alternative solutions. Segmented modulators make it possible to generate an optical signal modulated with PAM or QAM formats without the need of dedicated electrical components, in the so-called optical-DAC fashion. SEMZMs, together with their dedicated drivers, have recently been used for the generation of modulated signals with record low power consumption of below 1 W for a single intensity modulator [34]. DAC-free signal generation has been recently demonstrated for 25 GBd 4-PAM signals by using a 2-bit SiPh SEMZM as well as for 28 GBd 16-QAM signals by using two 2-bit SEMZMs in an IQ configuration with an energy per bit of 8.9 pJ/b [35], [14]. 25 GBd 4-PAM operation with a monolithically integrated CMOS driver has also been presented [36]. The optical-DAC finds its application in a broad range of real-world systems. Metro and short-reach scenarios benefit the most from the simplicity and power savings of a DAC-free transmission link. On the other hand, long distance communication channels already employ high order modulation formats and are the ones that most require high performance digital to analog conversion.

The optical-DAC generates quantized optical intensity levels at the output of the SEMZM, but requires only binary signals as inputs. This is possible due to the discretization of the induced phase shifts into as many levels as the number of implemented segments (Figure 4-2). In the SEMZM, each of the modulator's segments can individually be switched on and off. On the contrary, this is impossible in a traditional TWE-MZM, where all the active sections are connected. Depending on the number of switched on segments, a specific phase difference is induced in the interferometer arms and a precise optical intensity level is measured at the SEMZM output. Thus, the generation of a multi-level optical signal employing an IC driver whose output stages deliver only OOK stimuli becomes possible. Moreover, the driving IC is no longer required to be linear, opening the way for new energy-efficient driver topologies.

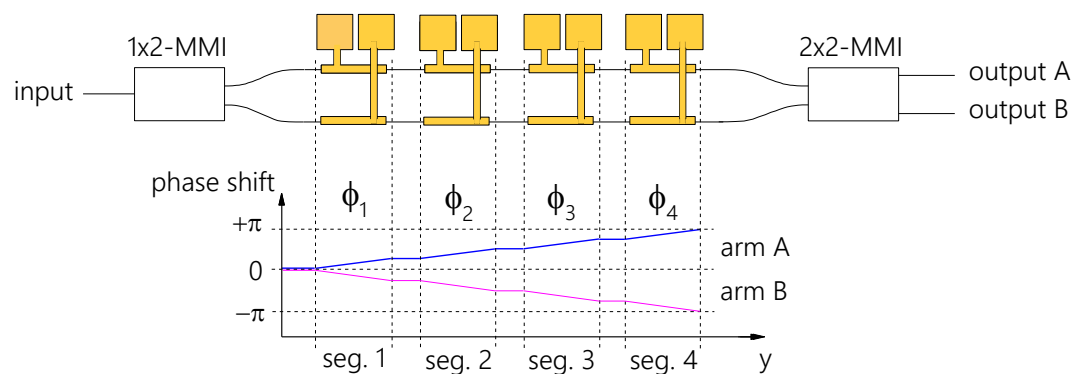


**Figure 4-2:** Quantization of the induced phase-shifts into as many levels as the number of segments. Each section is independently driven and can independently be turned on and off.

In optical digital-to-analog conversion, the available transmitter resolution is directly related to the number of segments in the modulator. As an example, to achieve an optical-DAC with 4-bit resolution,  $2^4 = 16$  levels are required. These are obtained by a SEMZM with  $2^4 - 1 = 15$  segments that are controlled in a thermometer configuration. Alternatively, the number of required segments can be reduced to  $2^4 / 2 = 8$  if the phase of the signal is also detected, at the cost of an increased drive voltage (Figure 4-3). This is the case for coherent transmission, where a coherent detector is employed to analyze both the amplitude and phase of the transmitted signal. If an IQ-SEMZM is used, 8-segment children modulators can be exploited to modulate a signal that addresses 256 points in the constellation diagram, i.e. 256-QAM. Because of the non-linearity of the MZM, the constellation symbols will not be equally spaced if the full MZM intensity swing is employed.

The position of the different optical intensity levels is instead related to the segments' induced phase shift and therefore to their lengths and the voltages applied to them, as shown in equation (2-1). Under the assumption that the same voltage swing is delivered to

all the different segments, two ways to implement the optical-DAC exist. The first optical-DAC topology is implemented by employing a SEMZM with segments of equal length. Within the driver chip, the output stages are grouped in a binary-weighted way and drive equivalent binary-weighted SEMZM active lengths. This approach simplifies the design of the modulator, but adds some complexity to the IC, as the input signals must be properly routed to the correct number of segments. The second approach instead consists of the realization of a segmented MZM with sections of different lengths. In particular, the different lengths can be made binary-weighted. In such a device, switching on a set of driver stages will result in a corresponding set of binary-weighted intensity levels. This approach allows for further reduction of the number of required segments compared to the thermometer drive and a simplification of the driver IC. Although the two approaches are not mutually exclusive, they are not mixed in the same design in literature.

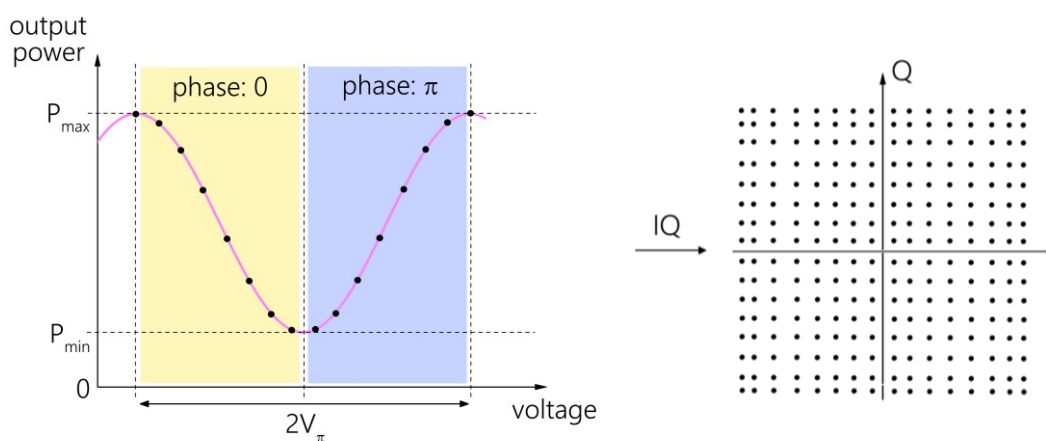


**Figure 4-3:** Single SEMZM characteristic with 16 states divided into two groups of 8 intensity levels and the corresponding constellation diagram. Eight intensity levels are required to address 256 points in the IQ plane. The constellation points are unequally spaced because of the non-linearity of the MZM.

In this chapter, these two approaches will be explored together with the implementation of different driver technologies. Firstly, a BiCMOS SiGe driver is used to drive a SEMZM with 15 segments of equal length. Secondly, a Mach-Zehnder segmented modulator with binary-weighted sections is employed together with a CMOS driver IC. The two assemblies are characterized and their in-field performance is presented and discussed. The chapter closes with a description of a segmented MZM with linearized EO transfer function obtained with a particular set of segments' lengths.

## 4.1. SEMZM driven by BiCMOS IC

The work reported in this chapter is part of the SASER project (<http://projects.celticplus.eu/saser/>). The SASER project aims to develop a highly spectral- and energy-efficient transmitter, which includes low power data conversion and DSP. It has been partially funded by the German Bundesministerium für Bildung und Forschung. The transmitter developed within the project is required to generate intensity and phase modulated signals in an  $M^2$ -QAM scheme without the need for an external dedicated DAC. The target transmitter specifications include a 4-bit resolution at a high symbol rate. For this goal, an IQ-SEMZM is developed. The chosen IC technology is the IHP Microelectronics 0.13  $\mu\text{m}$  BiCMOS SiGe:C. The targeted working speed of 56 GBd is enabled by the high transit frequency  $f_T = 250$  GHz.

The target specifications and the chosen IC technology affect both the modulator and the EO assembly design. The number of SEMZM segments is selected with a focus on high speed and low power consumption. As the implemented differential output stages of the IC consume both static and dynamic power, the number of segments is kept to a minimum in order to lower the energy requirements. However, the high 56 GBd target speed limits the maximum segment's capacitance  $C_{MZ}$ . In addition, this loading capacitance and the inductive assembly parasitics easily come into resonance within the frequency operating range. Although this resonance can be exploited as in chapter 3, an undesired and uncontrolled frequency peaking constitutes a threat for transmitter performance and is to be avoided. To push the resonance frequency of the segment  $f_{e0}$  far from the working range,  $C_{MZ}$  is kept below a certain limit. In practice, the electrodes are to be designed short and narrow, according to equation (3-3). Simultaneously, the SEMZM parasitic inductance  $L_{MZ}$  is also minimized, thanks to a specially developed multi-bridge design (Figure 4-4).

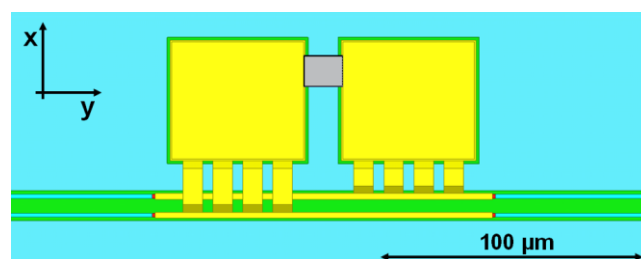


**Figure 4-4:** EM model of the segment targeting lowest parasitics: the multi-bridge design together with the short sections exhibit low inductance and capacitance, enabling 56 GBd operation.

The final design includes  $2^4 - 1 = 15$  equal segments, each 225  $\mu\text{m}$  long. The simulated  $C_{MZ}$  is 170 fF and  $L_{MZ}$  is 34 pH. The unloaded segment's resonance frequency for this structure is in this way pushed above 65 GHz and thus does not represent a problem for the operation of the modulator, provided the interconnections parasitics are kept to a minimum.

The proper weighting of the different bits is achieved thanks to the grouping of different segments within the driver IC, which includes a wired, binary to thermometer decoding scheme (Figure 4-5-a) [59]. The first group contains 8 segments, corresponding to the most significant bit (MSB), the second bit is connected to 4 segments, the third to 2 segments, and the least significant bit (LSB) goes to the last segment. Each output driver stage delivers a differential voltage output of  $2.5 V_{pp}$ , which is enough to provide the required  $2 \cdot V_{\pi}$  voltage swing to the IQ-SEMZM.

The IQ-SEMZM design is finalized at the optical level and the chips are fabricated in HHI. The measured mean optical IL of the InP device is 8 dB from fiber to fiber. The measured DC modulation efficiency is 0.33 V·cm and a  $(V_{\pi} \cdot IL) = 10.8$  V·dB is obtained at the best biasing condition. The driver IC is developed and fabricated in IHP. A modulator is assembled together with two BiCMOS drivers by Finisar Germany in an OIF-compliant module, which allows for large-signal measurements in a simpler environment compared to a chip-on-carrier solution (Figure 4-5-b).

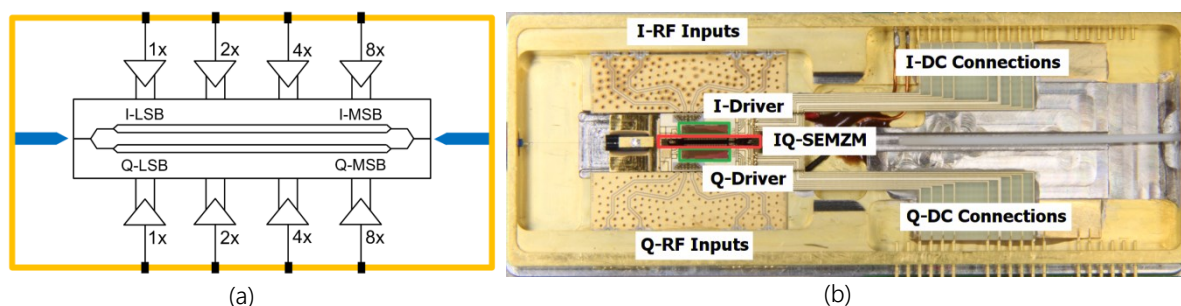


**Figure 4-5:** Schematic representation (a) and picture (b) of the packaged module. Four RF inputs are inserted on each long module side and routed in the driver to a binary-weighted number of SEMZM segments. The IQ-SEMZM is marked in red and the IC drivers in green.

The B2B measurements are performed employing a 4 differential channel BPG in order to generate the 8 required bit streams for the IQ modulator (Figure 4-6). Because of the limited number of data channels, the positive BPG outputs are directly connected to the I- inputs, whereas the Q-data is connected to the negative BPG outputs and de-correlated through electrical delay lines of sufficient length. A 1550 nm ECL is used as the continuous-wave laser source. After passing through the IQ-SEMZM+IC module, the optical signal travels through a VOA and an EDFA, employed to vary the optical signal-to-noise ratio, an additional EDFA and a polarization multiplexer. This multiplexer includes 2.6 m of fiber to de-correlate the two polarizations. The detection is performed with a polarization-diversity coherent receiver. The signal is digitized at a sampling rate of 80 GS/s with a real-time sampling oscilloscope with a 33 GHz bandwidth and digital signal processing is performed offline. The DSP algorithms, developed by the Photonic Networks department at Fraunhofer Heinrich-Hertz-Institut, include optical frontend correction, chromatic dispersion

compensation, and carrier phase recovery, along with two adaptive equalizers. Finally, a decision based on minimum Euclidean distance is made before bit errors counting. Because of the speed limitation of the data channels, the maximum achievable operating speed for this experiment is 32 GBd, although the expected operating speed is higher. A wide range of modulation formats can be implemented in the transmitter module, depending on what signal is fed to its inputs. For the 16-QAM measurements, only 2 bit streams are turned on for the I- and the Q-modulators each. The other inputs are left open. The same module is employed for the 64-QAM experiment by activating all the bit inputs for both modulators. In this case, 3 bits are employed for data transmission, whereas the last bit is used to compensate for design and fabrication mismatches and to move the constellation points closer to their ideal position on the IQ plane. The received BER curves versus OSNR for the two polarization division multiplexed (PDM) modulation schemes are measured (Figure 4-7). The 32 GBd constellations for X- and Y-polarizations at maximum OSNR after offline DSP are also shown, together with the received power spectra after analog-to-digital conversion.

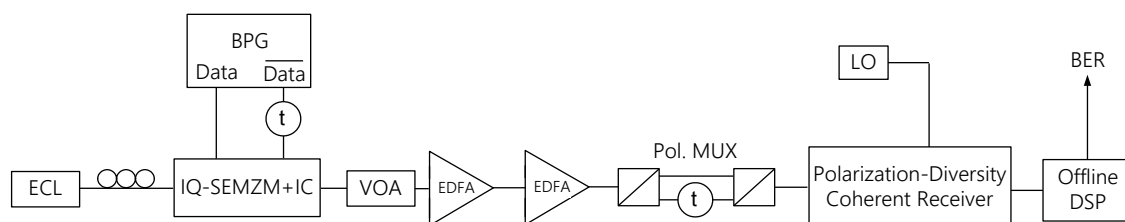


**Figure 4-6:** Experimental setup for the dual-polarization 32 GBd  $M^2$ -QAM B2B measurements.

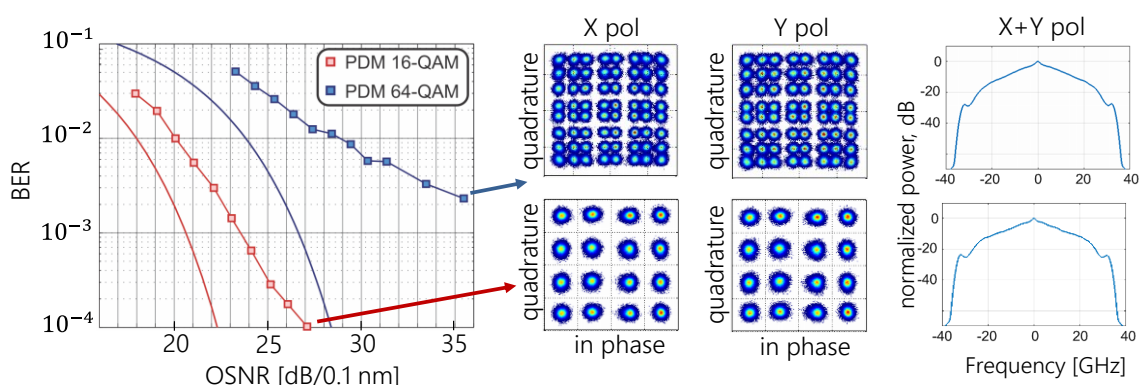


**Figure 4-7:** BER vs. OSNR curves of the PDM 16-QAM and PDM 64-QAM signals together with the theoretical limits, the correspondent IQ constellations at maximum OSNR and the received power spectra after the ADC. The points represent measured BER values and solid lines the theoretical BER in an AWGN channel.

The measured PDM-16QAM implementation penalty with respect to the theoretical OSNR requirements for an ideal additive white Gaussian noise (AWGN) channel at a BER of

$3.8 \cdot 10^{-3}$ , i.e. the HD-FEC threshold, is equal to 2.4 dB. At the soft-decision FEC (SD-FEC) threshold of  $2 \cdot 10^{-2}$  the penalty is as little as 2.2 dB. For the PDM 64-QAM signal, the implementation penalties at the HD and SD-FEC BER thresholds are 7.6 dB and 3.5 dB respectively.

The same module is employed for a transmission experiment. An SSMF 80 km long is inserted before the receiver, together with an additional EDFA to compensate for the fiber losses. The PDM 64-QAM signal is transmitted and a BER equal to  $9.1 \cdot 10^{-3}$  is measured at the receiver. This BER is well below the SD-FEC threshold and can be thus transmitted error-free with 21 % of overhead. The total power consumption for the generation of the 64-QAM modulated signal is equal to 1.5 W, which translates into a record low energy per bit of 7.8 pJ/b. This energy per bit is calculated for single polarization only.

#### 4.2. SEMZM driven by CMOS IC

The SPIRIT project (<http://www.spiritproject.eu>), co-founded by the European Commission through the Seventh Framework Program (FP7), aims to build a fully programmable transceiver, in a single package, for terabit optical networks. This extremely high data rate is transmitted on two wavelengths modulated in an  $M^2$ -QAM scheme. To generate the multilevel optical signals and implement optical-DAC functionalities, 5-bit high resolution is required for both the I- and the Q-modulator. At a symbol rate of 32 GBd, throughputs of up to 512 Gb/s on a dual-polarization wavelength are obtained. Eight bits are employed for data transmission, and the remaining two bits are used for transmitter DSP. The terabit data rate is thus achieved by modulating two wavelengths on a single device. The system level targets necessitate of a low-power high-resolution scalable solution on the transmitter side. The chosen topology is an IQ segmented MZM driven by a 40 nm CMOS driver IC. The driver is developed by the IMEC-INTEC group in Gent, Belgium. The transmitter contains a hybrid assembly of different technologies. In addition to the InP modulator and the CMOS driver, polymer waveguides are employed to route the light out of the SEMZM into a silicon platform, which contains optical multiplexing and demultiplexing stages. The developed SEMZM implements features specific to the foreseen assembly topology, both on the electrical and optical level. This section discusses the most distinctive properties of the optical-DAC, i.e. the design of the active area and the evaluation of the EO performance.

The SEMZM active area design is a compromise between different trade-offs, some of which have already been discussed in chapter 3. The chosen CMOS IC technology limits the deliverable voltage to a maximum of 1.1 V for a single segment's branch. In addition, the active length of the modulator is constrained by the size of the IC chip, which is strictly related to the fabrication costs. The two previously discussed optical-DAC implementations

are here mixed: the selected design includes 10 binary-weighted segments of different lengths that are divided into five groups within the driver IC. This arrangement allows for a concurrent reduction of the number of required sections and of the maximum segments' length, so as to not overload the IC. All the segments in one modulator's arm sum to the total active length  $L_a$  of 2945  $\mu\text{m}$ . This  $L_a$  fits well with the expected modulation efficiency and ensures the SEMZM is fully driven by the 40 nm CMOS driver. The segments are closely packed with a constant pad pitch, equal to the minimum allowed by technology (Figure 4-8).

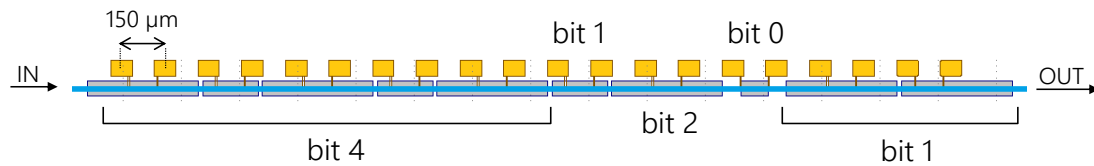


**Figure 4-8:** Final arrangement of the single SEMZM's arm designed for CMOS drive. The segments are grouped in binary-weighted overall lengths. Splitting the bits into multiple segments allows for a lower loading capacitance per IC stage and consequent higher speed operation.

EM simulations are performed to extract the equivalent segment's capacitance and investigate joint operation with the IC driver. The 380  $\mu\text{m}$  segments, i.e. the longest ones, constitute the largest capacitive load and thus represent the most interesting structures to be simulated. In particular, a high capacitive load may limit the driver bandwidth and become critical for the speed performance of the system. The segments are simulated in the configuration previously described in section 3.2.2 and the equivalent RLC parameters are extracted to be  $C_{MZ} \approx 250$  fF,  $L_{MZ} \approx 50$  pH and a variable  $R_{MZ}$  over frequency in the range of a few  $\Omega$ . Simulated eye diagrams are obtained with a joint simulation of the segment load and the IC driver performed by IMEC-INTEC, showing an open OOK eye at the data rate of 25 GBd (Figure 4-9).

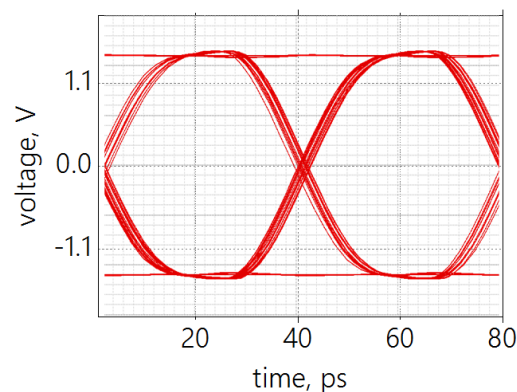


**Figure 4-9:** Simulated 25 GBd OOK differential electrical eye diagram when driving a segment 380  $\mu\text{m}$  long. The voltage is acquired on the segment's capacitances, as this is representative of the EO performance.

The IQ modulators are laid out taking into consideration all the results obtained through simulations. The final arrangement of segments is implemented in a mirrored way for the I- and the Q-arms, and the light is properly routed through them (Figure 4-10). The chip footprint is 10 mm x 820  $\mu\text{m}$  and includes some self-alignment structures that are necessary for the chosen integration approach. Phase electrodes are implemented in order to select the SEMZM working point for the parent IQ-modulator, as well as for the two children modulators. The fabricated wafers are cleaved into bars and the modulator's facets are coated with an anti-reflecting layer. The DC characterization of the different modulators is performed with two multi-needle probes that contact all the 53 pads for all the different segments and biasing points (Figure 4-11). The measured fiber-to-fiber insertion loss is equal to 9 dB at 1550 nm. With all the segments connected together a  $V_{\pi} = 0.9$  V is measured. This switching voltage is below the 1.1 V threshold and therefore full modulation is expected.



**Figure 4-10:** CAD mask layout of the InP IQ segmented modulator (1: spot-size converters, 2: parent IQ biasing electrodes, 3: grooves for vertical alignment, 4: RF segments, 5: I and Q biasing electrodes, 6: grooves for lateral alignment, 7: monitor diodes)

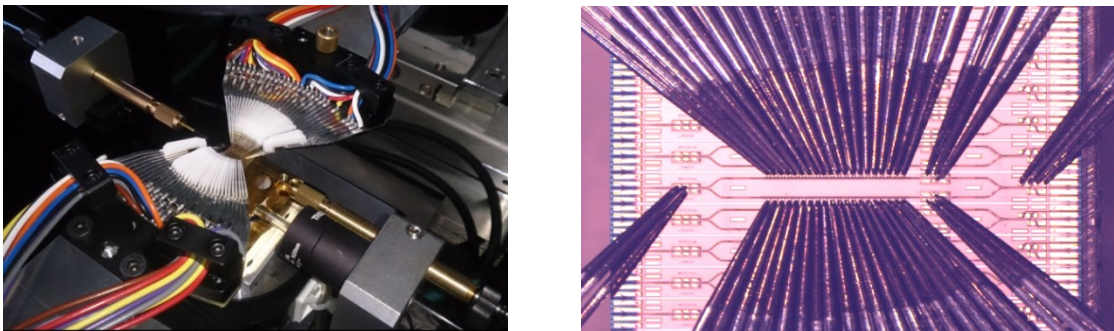


**Figure 4-11:** DC measurements setup picture and micrograph. Two multi-needles probes approach from the modulator's sides and contact 53 pads on the IQ-SEMZM. Optical fibers bring the light in and out of the InP chips.

The large-signal EO functionality of the IC and of the SEMZMs is tested with IQ chips that are assembled together with a single CMOS driver on dedicated carriers designed by IMEC-INTEC. These carriers include RF differential lines and GPPO connectors, bypass capacitors, DC connectors for the two chips, and a TEC. The RF board is employed to fan-out the several high-frequency interfaces of the driver chip. However, due to the large number of lines and the limited space, only four input bits are connected. The necessary data streams

are provided with a 4-channel BPG. A high-frequency clock signal is used to select the working speed and re-time the electrical signal inside the CMOS driver. The optical path starts with a 1550 nm ECL. After modulation, the signal is amplified and detected with an optical sampling oscilloscope.

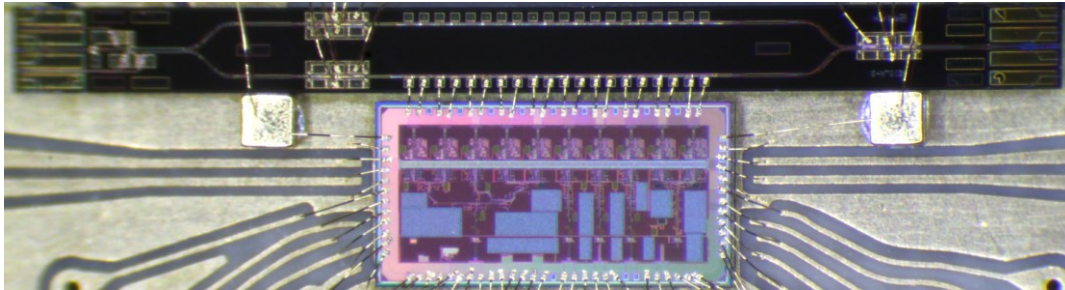


**Figure 4-12:** Chip micrograph of the IQ-SEMZM with one arm bonded to the CMOS driver IC. Because of the PCB limited space, only one SEMZM is driven and the number of RF inputs is limited to 4. Additional DC routing lines and bypass capacitors are visible.

Because of a retiming problem in the driver IC, the transmitter speed is limited to 15 GBd. This must be improved in future designs. All segments are proven operational up to this symbol rate. An open eye is obtained by feeding the same PRBS sequence to all four driver inputs (Figure 4-13-a). The optical extinction ratio is varied by turning the different segments on and off and is equal to 16.4 dB when all the segments are turned on. The 8-PAM eye diagram is obtained by feeding de-correlated data streams to three different bits, and leaving the fourth one unconnected (Figure 4-13-b). Eight intensity levels are visible, but not fully separated. The reason for this is the voltage overshoots that appear because the operating speed is only equal to half of the intended one. When the last bit is also turned on and fed an independent signal, the different levels become indistinguishable in the optical oscilloscope because of the reduced space in between them. However, the whole set of  $2^4 = 16$  levels in the optical oscilloscope is observed with the use of a synchronous trigger. In this way, a staircase-waveform is obtained and the different levels are easily counted (Figure 4-13-c). The shape of the SEMZM transfer function is visible, with the outer levels less spaced out than the inner ones, despite the equal steps in the applied voltage. The visible troughs and peaks are attributed to retiming imprecisions: these features appear when the switching of the different stages is not performed at the ideal moment.

The second phase of the measurements is performed by adding a noise loading stage followed by a coherent receiver, in place of the sampling oscilloscope. The acquired data is processed with an offline DSP, this time developed by the National Technical University of Athens, similarly to what was performed in the setup of Figure 4-6. This time, the working point of the modulator is set at the zero transmission point. The obtained modulation

formats are named in accordance with the number of states the amplitude and phase of the signal takes, in an M-ASK-N-PSK fashion. These formats are selected in order to show the potential of the  $M^2$ -QAM signal generation, when both the IQ arms are driven. The BER curves, when 2 and 3 data streams are activated, are measured versus OSNR (Figure 4-14). The implementation penalty for the 2-ASK-2-PSK signal is lower than 1 dB at the HD-FEC threshold, whereas for the 4-ASK-2-PSK signal, corresponding to a 16-QAM signal in an IQ configuration, the penalty is 1.95 dB.

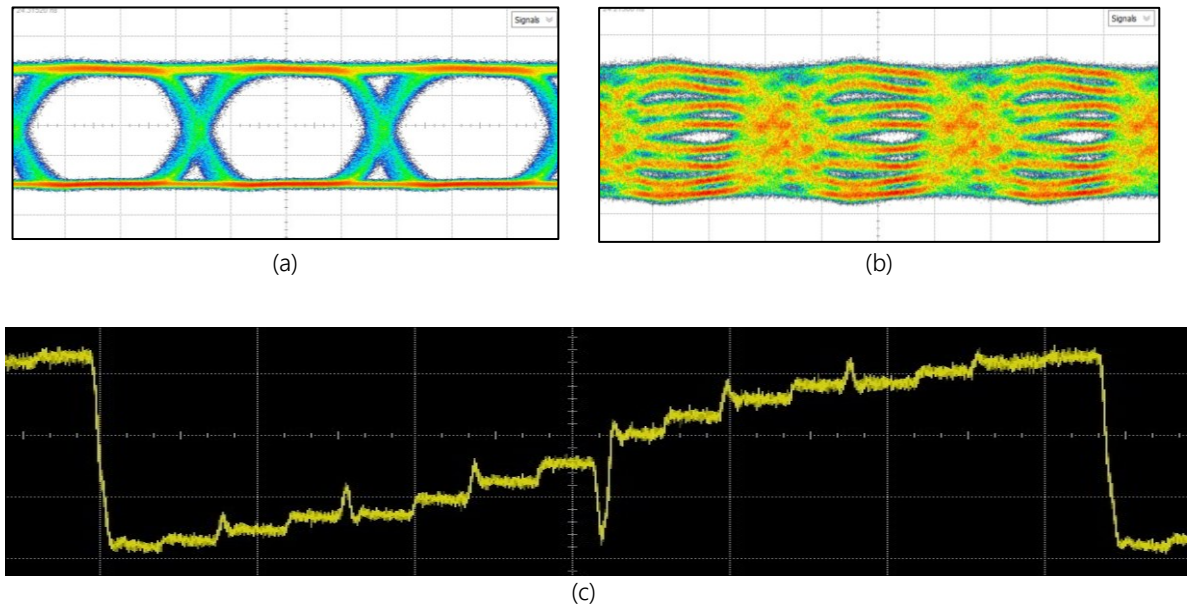


**Figure 4-13:** Received optical signals: (a) 15 Gbd eye diagram when all the segments are switched on and fed the same input sequence, (b) 15 Gbd 8-PAM eye diagram when 3 de-correlated sequences are provided at the driver inputs, (c) pattern-locked staircase when all 4 bits are de-correlated.

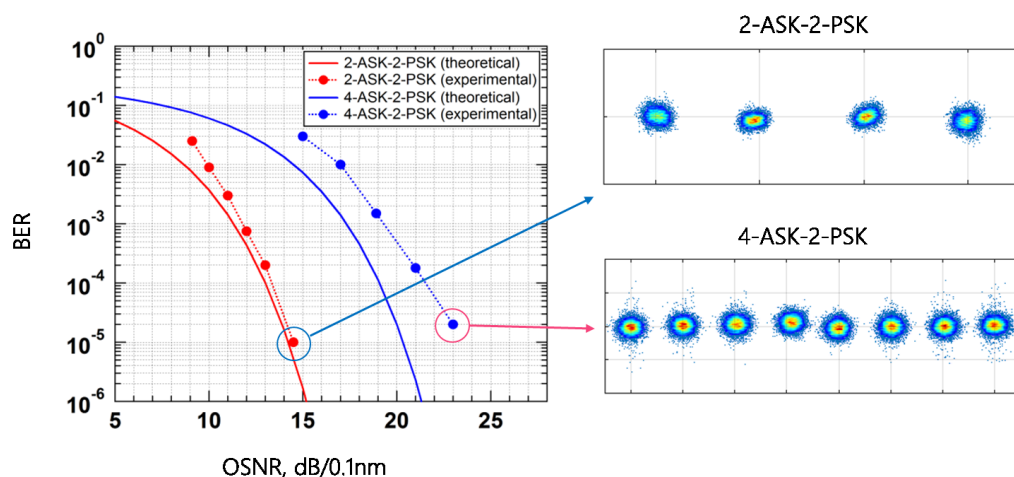


**Figure 4-14:** BER vs. OSNR curves for the 2-ASK-2-PSK and 4-ASK-2-PSK signals together with the theoretical limits and the correspondent IQ constellations at maximum OSNR. Points represent measured BER values and solid lines the theoretical BER in an AWGN channel.

## 4.3. Segmented Mach-Zehnder Linearization

As previously discussed, the introduction of binary-weighted phase-shifts represents a meaningful option, not only because of the analogy with an electrical DAC, but also because it enables the generation of equally spaced electrical levels that are employed to uniformly cover the entire available power range. In high resolution DACs, a part of the effective number of bits is used to pre-distort the drive signal and compensate for the non-linearity of the MZ modulators. The same can be done in the case of optical-DACs by selecting the desired intensity levels out of the pool of the available ones. However, this approach sacrifices part of the available resolution, reducing the number of levels that can be employed for data transmission. A way to linearize the SEMZM TF without sacrificing resolution consists of targeting specific optical intensity levels directly at the hardware level, either within the electronics or on the InP chip [60].

According to equation (2-5), the output intensity of the Mach-Zehnder modulator is nonlinear with respect to the modulation voltage. The optical power steps observed to the modulator's output are therefore not constant when regular voltage steps are applied at the MZM electrical inputs (Figure 4-15). A consequence of this is the introduction of a distortion in the modulated signal, due to harmonic components that are generated when the driving signal is of sufficient amplitude. If the chosen modulation scheme is OOK, the problem is easily bypassed by under-modulating the MZM in order to avoid the extremes. However, the cost of this solution is a loss in modulation depth that sometimes, especially for multilevel signals, cannot be compromised.

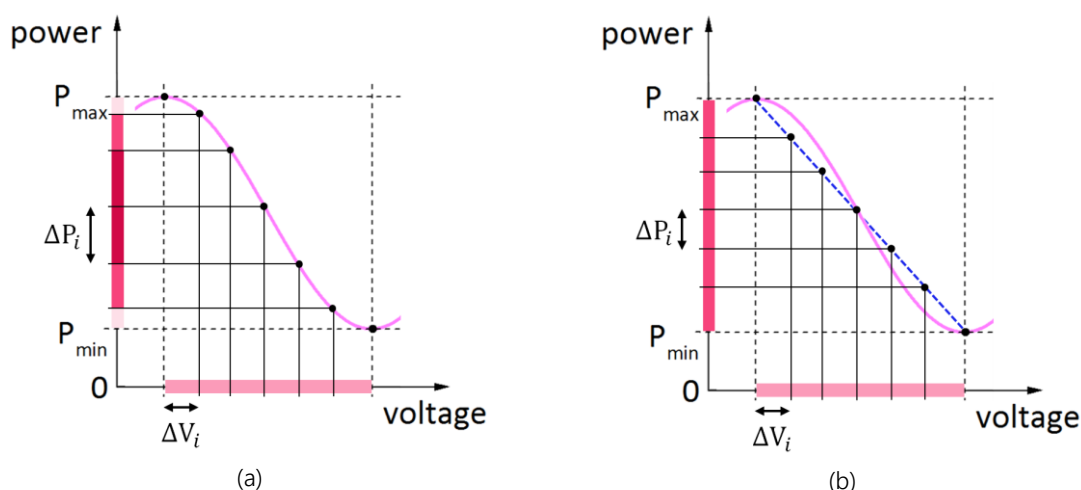


**Figure 4-15:** Transfer function of the MZM with color-coded voltage and intensity levels. (a) The non-linear TF makes equal voltage steps  $V_i$  correspond to different steps in the optical power  $P_i$ . (b) Linearized modulator's TF: equal voltage steps correspond to equal power levels.

A different way to normalize the MZM characteristic consists of the pre-distortion of the input signal in such a way so as to provide unequal steps of the induced phase-shifts. If

these levels are selected so that they correspond to equally spaced intervals of optical intensity, TF linearization is achieved. In a TWE-MZM, all the electrodes are connected together and have the same length in order to provide velocity match, making the implementation of such a solution impossible. On the contrary, in a SEMZM with  $N$  sections, the voltage applied on each segment and the corresponding induced phase-shift can be individually defined (Figure 4-16).

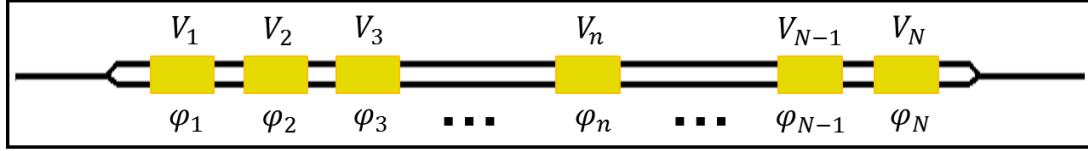


**Figure 4-16:** Schematic representation of a SEMZM with  $N$  segments. The  $i$ -th segment induces a discrete phase-shift  $\varphi_i$  when a voltage  $V_i$  is applied on it.

The overall phase difference accumulated as the optical wave travels along the waveguide is expressed as the sum of the ones induced by the individual segments pairs:

$$\Delta\varphi = \sum_{i=1}^N \varphi_i \quad . \quad (4-1)$$

The partial phase-shift  $\theta_p$  that is accumulated after the optical wave has travelled through  $p$  segments can be written as:

$$\theta_p = \sum_{i=1}^p \varphi_i \quad . \quad (4-2)$$

The corresponding optical intensity at the modulator's output is then rewritten from equation (2-5) as:

$$I_p = \frac{1}{2} + \frac{1}{2} \cos(\theta_p) \quad . \quad (4-3)$$

In the case of a linearized TF, all intensity steps  $\hat{I}_i$  are required to be equal, resulting in

$$\hat{I}_i = \frac{1}{N} \quad \text{and} \quad \hat{I}_p = \frac{p}{N} \quad . \quad (4-4)$$

Equation (4-3) can thus be rewritten for the case of the linearized transfer function solving explicitly for the corresponding  $\hat{\theta}_p$  as

$$\hat{\theta}_p = \arccos\left(2\frac{p}{N} - 1\right) \quad . \quad (4-5)$$

The phase-shift that the  $i$ -th segment needs to induce is therefore calculated from  $\hat{\theta}_p$  by subtracting the phase-shifts induced by the previous segments.

$$\hat{\varphi}_i = \hat{\theta}_p - \sum_{j=1}^{p-1} \hat{\varphi}_j = \hat{\theta}_p - \hat{\theta}_{p-1} \quad (4-6)$$

The condition on the  $i$ -th segment's length  $\hat{L}_i$  is derived from equation (2-2) by setting  $i = p$  and assuming the delivered voltage equals  $V_\pi$ :

$$\hat{L}_i = \frac{L_a}{\pi} \cdot \left[ \text{acos} \left( 2 \cdot \frac{i}{N} - 1 \right) - \text{acos} \left( 2 \cdot \frac{i-1}{N} - 1 \right) \right] \quad (4-7)$$

Similarly, for a constant segment's length, it is also possible to express the relationship over the voltage steps needed to linearize the SEMZM TF. This second solution might seem preferable, as it does not require the optical hardware to be modified. However, the design of a driver array with multiple output stages able to deliver a precise but different output voltage is not trivial, making this second approach impractical.

A segmented modulator with 15 sections of different lengths is designed and fabricated in the Fraunhofer HHI facility (Figure 4-17). The electrode lengths are calculated according to equation (4-4). In addition, a SEMZM with the same optical layout but identical segments is also developed and used as a comparison.

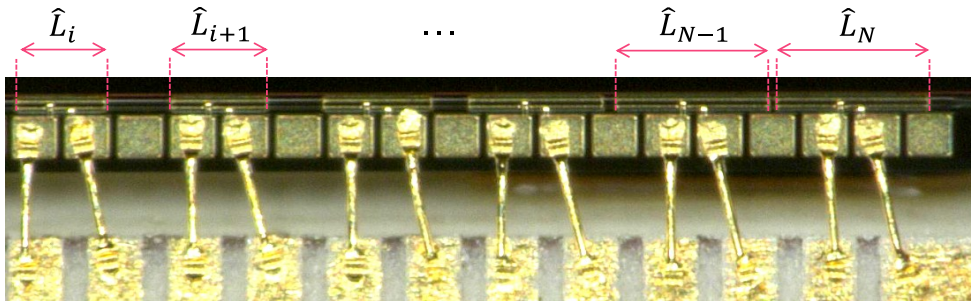


**Figure 4-17:** Segments in detail for the linearized SEMZM. The segments' lengths are calculated according to equation (4-4) in order to induce equally spaced intensity levels when switched on or off.

The spacing of the intensity levels is qualitatively evaluated with an optical oscilloscope and by switching the different segments sequentially on or off, as in a thermometer drive configuration. The images obtained with the oscilloscope in persistence mode show the difference between a normal and a linearized SEMZM (Figure 4-18). The unequal spacing of the intensity levels is clearly visible on the vertical axis: the last segments' contributions are reduced as they approach the extremes of the SEMZM TF. However, in the case of the linearized SEMZM the spacing between the different levels appears to be much closer to constant.

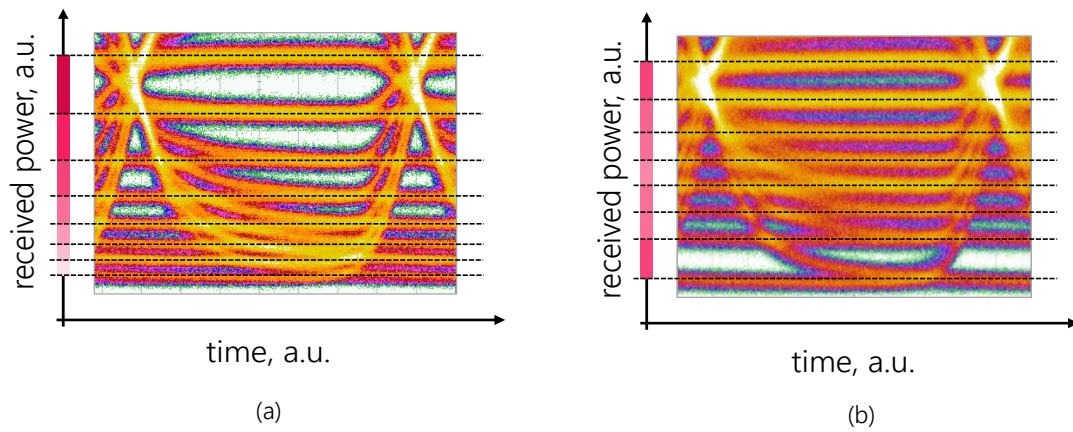


**Figure 4-18:** Lower-half detail of the measured optical intensity levels, as seen in a sampling oscilloscope in persistence mode. The SEMZM with segments of equal length (a) shows non-linear spacing, whereas the SEMZM with appropriate length (b) exhibits almost equally-spaced intensity levels.



---

## 5. Discussion and Conclusions

In this work, a segmented Mach-Zehnder modulator is presented as a way to implement today's transmitter DAC functionalities without the need of electrical components specially to these tasks. Consequently, space and power requirements can be significantly reduced without sacrificing the system performance. After an introduction to optical transmitters and Mach-Zehnder modulators, the main steps of the design of a SEMZM have been discussed in Chapter 3. A connection between the degrees of freedom of the design of the segments and their performance has been provided.

The resonant version of the SEMZM is first employed to enhance the electro-optic bandwidth of the transmitter from 22 GHz to 30 GHz. An OOK 56 GBd open eye has been obtained employing electronics limited to 22 GHz only. BER measurements prove the advantage over a commercial LiNbO<sub>3</sub> reference driven by the same setup, both versus dispersion and OSNR. Later, a resonant SEMZM that performs narrow spectral shaping and concurrent frequency equalization of an optical signal for Nyquist-WDM scenarios has been presented. Because of this shaping, no cross-talk between two neighboring subcarriers spaced at 50 GHz was observed when transmitting 320 Gb/s in a dual carrier DP PAM-4 setup over 80 km of SSMF. The measured BER curves are below the HD-FEC threshold for an OSNR greater than 23 dB. With an occupied bandwidth of 100 GHz, the overall measured gross spectral efficiency is 3.2 b/s/Hz.

In Chapter 4, the DAC-less generation of high-order modulation formats, when driving the SEMZM first with a BiCMOS and then with a CMOS dedicated driver, is demonstrated. The specific design constraints derived from the chosen IC technology have been highlighted. Up to 64-QAM modulation with a flexible transmitter module employing a 4-bit InP IQ-SEMZM and BiCMOS dedicated drivers has been presented. The record speed of 32 GBd and low power consumption of 1.5 W translate into a total gross data rate of 384 Gb/s and an energy per bit of 7.8 pJ/b. This signal is polarization multiplexed and transmitted over 80 km of standard single mode fiber (SSMF). The received BER is measured to be below the soft decision forward error correction (SD-FEC) threshold. By alternatively using a 40 nm CMOS driver, a single IQ-SEMZM has been driven and 15 GBd 2-ASK-2-PSK and 4-ASK-2PSK signals have been generated. The measured BER is well below the HD-FEC threshold. This looks promising for the generation of M<sup>2</sup>-QAM formats. With respect to the more widespread CMOS driver topologies, the use of BiCMOS technology allows for higher speed and larger output voltages, maintaining comparable power consumption well below that of a solution that includes a DAC [8]. However, the CMOS driver employed here includes extra logic in order to provide wide tuning of the time

delay between the segments, which is not included in the SiGe IC. With a different design and a smaller technology node, the CMOS IC might indeed become the best choice in terms of power consumption. The optical-DACs presented here advance the state of the art technology in the direction of high-resolution low-power transmitters (Table 5-1).

Ref.	MZM	$(V_{\pi} \cdot L_a)$ [Vcm]	IC	Datarate [GBd]	Modulation	Bits/MZM	Power [W]	Energy/bit [pJ/b]
[34]	InP	-	65 nm CMOS	10	8-PAM	3	0.95	31.6
[33]	SiPh	0.13	40 nm CMOS	10	4-PAM	2	0.45*	22.5
[14]	SiPh	0.2	40 nm CMOS	28	16-QAM	2	2 · 0.5	8.9
[36]	SiPh	1.47	90 nm CMOS	28	4-PAM	2	0.27	4.8
<b>SASER</b>	<b>InP</b>	<b>0.33</b>	<b>0.13 <math>\mu</math>m BiCMOS</b>	<b>32</b>	<b>64-QAM</b>	<b>3</b>	<b>2 · 0.75</b>	<b>7.8</b>
<b>SPIRIT</b>	<b>InP</b>	<b>0.27</b>	<b>40 nm CMOS</b>	<b>15</b>	<b>4-ASK- 2-PSK</b>	<b>3</b>	<b>1</b>	<b>22.2</b>

\*with laser

**Table 5-1:** Comparison of the state of the art optical-DACs.

In section 4.3, a SEMZM has been employed together with its dedicated IC driver to prove the linearization of the non-linear transfer function by means of hardware-coded segment's lengths. The qualitatively evaluated intensity levels at the modulator's output constitute a clear sign that the proposed approach works.

### 5.1. Outlook

The work here discussed opens a multitude of paths that can be followed when one seeks to improve the segmented modulator's performance and push the state of the art.

Although the proposed SEMZM modelling ensemble is proven valid in the frequency range of interest, some additional work must be done to improve its reliability, especially for correct prediction in the optical domain. Concerning the frequency equalization of the resonant devices, the analog approach presented here suffers from low flexibility with respect to the standard DAC-enabled one. For this reason, methods to increase the flexibility of the peaked characteristics are of great interest. Further work with the available spectral shaping devices will include the investigation of the crosstalk-induced penalty for smaller subcarriers spacing.

The optical-DAC devices presented here are functional, but they are not yet pushed to their limit. The BiCMOS driven SEMZM is expected to be able to perform at higher speeds, but the available BPG set a limit of 32 GBd. With a different source, a higher symbol rate can be targeted. In addition, extra bits are available, up to a total of 5 in the case of the CMOS-driven SEMZM. These can be used to demonstrate for the first time a DAC-free generation of a 128-QAM signal and a variety of DSP implemented algorithms.

The different SEMZM approaches discussed in this thesis are not mutually exclusive. In particular, a bandwidth-enhancing pulse-shaping optical-DAC can be realized by combining the different designs discussed. To this end however, it is mandatory that higher control and flexibility are obtained for the single segment's TFs. The realization of a multiple resonating segment SEMZM for optical-DAC PAM-4 generation and transmission of more efficient modulation schemes constitutes the first step in this direction.



---

## 6. Acknowledgments

I would like to thank a number of people that made this work possible in the very first place. I am grateful to Prof. Schell for his guidance and for giving me the possibility of working in such a good place as Fraunhofer Heinrich-Hertz-Institut. I would like to acknowledge Prof. Bogoni as well for supervising the final parts of my work.

I deeply thank all the people in the modulator group for their support and the many hours spent listening to my *few* questions and complaints. Thanks to Klemens and Karl-Otto for their trust and for first hiring me, and then not firing me. Special thanks go to Gerrit: your genuine interest in helping the people around you makes you a great person, despite the horrible language you speak! Thanks to Sophie and Braulio for proofreading my thes... ..well, for your patience and for going through the "Marchstraßenhölle" with me, every day. Merci Patrick for the funny "breaks", starting from that Glaskaste meeting with poor naïve Gerrit. Thanks to Marko, for making the lab fun... sometimes...

Many many thanks go to Dr. Venghaus and Tomasz for the correction of my work. Before you wonder: yes, I willingly did not correct this section!

Thanks to my friends, those in Berlin and those around the world - who I can't see as much as I wish - , for always making me laugh and feel loved! <3 <-- amici italiani inclusi qui!

Grazie alla mia famiglia (e Giuliana). Non esistono decolli turbolenti o misteriosi atterraggi nella nebbia che possano trattenermi dal venirvi a trovare il più possibile. Volare col sole però è meglio...

Thank you, Tom. Long story short: one of your smiles is worth a million PhDs.



---

## 7. List of Abbreviations

ADC .....	Analog-to-digital
ASIC .....	Application specific integrated circuit
ASK .....	Amplitude-shift keying
AWGN .....	Additive white Gaussian noise
B2B .....	Back-to-back
BPG .....	Bit pattern generator
CAD .....	Computer aided design
DAC .....	Digital-to-analog
DC .....	Direct-current
DML .....	Directly modulated laser
DSL .....	Digital subscriber line
DSP .....	Digital signal processing
DUT .....	Device under test
ECL .....	External cavity laser
EDFA .....	Erbium-doped fiber amplifier
EM .....	Electro-magnetic
EML .....	Electro-absorption modulated laser
EO .....	Electro-optical
ER .....	Extinction ratio
HD-FEC .....	hard-decision forward error correction
I- .....	In-phase
IC .....	Integrated circuit
ICI .....	Interchannel interference
IL .....	Insertion loss
InP .....	Indium Phosphide
ISI .....	Intersymbol interference
LiNbO <sub>3</sub> .....	Lithium niobate
LSB .....	Least significant bit
MMI .....	Multi-mode interferometer
MQW .....	Multiple quantum well
MSB .....	Most significant bit

## 7 List of Abbreviations

---

MUX .....	Multiplexer
MZM .....	Mach-Zehnder modulator
NRZ .....	Non-return to zero
OE .....	Opto-electrical
OOK .....	On-off keying
OSNR .....	Optical signal-to-noise ratio
PAM .....	Pulse-amplitude modulation
PAPR .....	Peak-to-average power ratio
PD .....	Photodetector
PDM .....	Polarization division multiplexed
PRBS .....	Pseudorandom bit sequence
PSK .....	Phase-shift keying
Q- .....	Quadrature
QAM .....	Quadrature-amplitude modulation
RC .....	Raised cosine
RF .....	Radio frequency
RRC .....	Root-raised cosine
SD-FEC .....	Soft-decision forward error correction
SEMZM .....	Segmented Mach-Zehnder modulator
SG .....	Signal-ground
SiPh .....	Silicon photonics
SSC .....	Spot-size converter
SSMF .....	Standard single-mode fiber
TE .....	Transverse-electric
TF .....	Transfer function
TWE .....	Traveling-wave electrode
VOA .....	Variable optical amplifier
WDM .....	Wavelength division multiplexing
WG .....	Waveguide

---

## 8. List of Symbols

$\varphi$	Phase shift
$\rho_{A,B}$	Electro-optical parameters
$V$	Voltage
$V_{\pi}$	Switching voltage
$L$	Length
$L_a$	Active length
$E_{in}$	Input electric field
$E_{out}$	Output electric field
$H$	Transfer function
$I_{out}$	Output intensity
$I_{in}$	Input intensity
$P$	Power
$P_{in}$	Input power
$P_{max}$	Maximum output power
$P_{min}$	Minimum output power
$l_e$	Electrode length
$N$	Number of segments
BR	Baud-rate
$T$	Bit length
$\beta$	Roll-off factor
$\lambda$	Wavelength
$\lambda_{min}$	Shortest operating wavelength
$L_c$	Critical length
$n_e$	Effective refractive index
$c$	Velocity of light in vacuum
$C_{MZ}$	Segment capacitance
$\epsilon_0$	Dielectric constant of vacuum
$\epsilon_r$	Relative dielectric constant
$w_w$	Waveguide width
$x_d$	Depletion region thickness
IRT	Intrinsic region thickness

## 8 List of Symbols

---

$R_{MZ}$	Segment resistance
$\delta$	Skin depth
$\omega$	Pulsation
$\rho$	Resistivity
$\mu$	Magnetic permeability
$f_o$	Resonance frequency
$L_{MZ}$	Segment inductance
$L_{BW}$	Bondwire inductance
$C_c$	Coupling capacitor
$Z_S$	Source impedance
$Z_{in}$	Segment input impedance
$R_{DC}$	DC segment resistance
$X_L$	Inductor reactance
$X_C$	Capacitor reactance
$V_C$	Voltage drop on the capacitor
$Q$	Quality factor
$f_{eo}$	Electro-optic resonance frequency
$V_{in}$	Segment input voltage
$R_S$	Source resistance
$X_S$	Source reactance
$w_{eo}$	Electro-optic resonance pulsation
$x$	Time-domain input electrical signal
$X$	Frequency-domain input electrical signal
$y$	Time-domain output optical signal
$Y$	Frequency-domain output optical signal
$W$	Taper width
$R_p$	Parallel resistance
$f_{stub}$	Stub resonance frequency
$f_T$	Transit frequency
$\theta_p$	Partial phase shift
$\hat{I}$	Linearized intensity
$\hat{\theta}$	Linearized partial phase shift

---

## 9. Published Work

Parts of this work have been published:

A. Aimone, I. Garcia Lopez, S. Alreesh, P. Rito, T. Brast, V. Höhns, G. Fiol, M. Gruner, J.K. Fischer, J. Honecker, A.G. Steffan, D. Kissinger, A.C. Ulusoy and M. Schell, "DAC-free Ultra-Low-Power Dual-Polarization 64-QAM Transmission with InP IQ Segmented MZM Module," in *Optical Fiber Communications Conference*, Anheim, 2016.

A. Aimone, P. W. Berenguer, C. Meuer, M. Gruner, J. K. Fischer, C. Schubert and M. Schell, "DAC-Free 320 Gb/s 2-Carrier Nyquist-Space DP PAM-4 Transmission by Resonant InP MZM," in *IEEE Photon. Technol. Lett.*, vol. 28, no. 7, pp. 775-777, 2016.

A. Aimone, G. Fiol, M. Gruner and M. Schell, "Engineered Transfer Function InP Mach-Zehnder Modulator for Bandwidth Enhancement and Nyquist Shaping," *J. Lightw. Technol.*, vol. 34, no. 8, pp. 1694-1698, 2016.

A. Aimone, G. Fiol, M. Gruner and M. Schell, "56 Gbit/s OOK transmission with 20 GHz electronics by resonating segmented electrode InP Mach-Zehnder modulator," in *Electron. Lett.*, vol. 51, no. 23, pp. 1897-1898, 2015.

A. Aimone, G. Fiol, M. Gruner and M. Schell, "InP MZ modulator with engineered transfer function for 1.5x bandwidth enhancement and Nyquist shaping," in *European Conference on Optical Communications*, Valencia, 2015.

S. Dris, M. Vanhoecke, A. Aimone, D. Apostolopoulos, I. Lazarou, P. Demeester, J. Bauwelinck, G. Gotz, T. Wahlbrink and R. Magri, "A programmable, multi-format photonic transceiver platform enabling flexible optical networks," in *International Conference on Transparent Optical Networks*, Budapest, 2015.



---

# 10. Bibliography

- [1] J. Bourne and D. Burstein, *DSL*, A Wiley Tech Brief, John Wiley & Sons, Inc., 2001.
- [2] R. B. Moares, K. Hooghe, A. Duque, J. Galaro, M. Timmers, A. J. van Wijngaarden, M. Guenach and J. Maes, "XG-FAST: Towards 10 Gb/s Copper Access," in *Globecom Workshops*, Austin, 2014.
- [3] J. C. Cartledge and A. S. Karar, "Breakthroughs in Photonics 2012: Generation of Modulated Optical Signals for Optical Fiber Communications," *IEEE Photonics J.*, vol. 5, no. 2, 2013.
- [4] P. W. Berenguer, M. Nölle, T. Raman, A. Napoli, C. Schubert and J. K. Fischer, "Nonlinear Digital Pre-Distortion of Transmitter Components," *J. Lightw. Technol.*, vol. 34, no. 8, pp. 1739-1745, 2015.
- [5] B. Gomez Saavedra, N. Wolf, L. Yan, C. Meuer, J. H. Choi, K.-O. Velthaus, M. Gruner, C. Schubert, H.-G. Bach and M. Schell, "First 105 Gb/s Low Power, Small Footprint PAM-8 Impedance-engineered TOSA with InP MZ-Modulator and Customized Driver IC using Predistortion," in *Optical Fiber Communications Conference, Th4E4*, Los Angeles, 2015.
- [6] J. McNicol, M. O'Sullivan, K. Roberts, A. Comeau, D. McGhan and L. Strawczynski, "Electrical Domain Compensation of Optical Dispersion," in *Optical Fiber Communications Conference, OThJ3*, Anaheim, 2005.
- [7] C. Laperle and M. O'Sullivan, "Advances in High-Speed DACs, ADCs, and DSP for Optical Coherent Transceivers," *J. Lightw. Technol.*, vol. 32, no. 4, pp. 629-643, 2014.
- [8] A. Konczykowska, J.-Y. Dupuy, F. Jorge, M. Riet, J. Moulu, V. Nodjiadjim, P. Berdaguer and J. Godin, "42 GBd 3-bit Power-DAC for Optical Communications with Advanced Modulation Formats in InP DHBT," *Electron. Lett.*, vol. 47, no. 6, pp. 389-390, 2011.

- [9] Y. Shuangyi, "D 2.2. - Investigation and Assessment of the Potential Technologies for the Flexi-Grid Optical Path-Packet Infrastructure for Ethernet Transport," Public Deliverable, The STRAUSS Project (FP7-ICT-2013- EU-Japan), 2015.
- [10] H. Chen, Development of an 80 Gbit/s InP-based Mach-Zehnder Modulator, PhD Thesis, Berlin: Technische Universität, 2007, pp. 3-15.
- [11] G. T. Reed, G. Mashanovich, F. Y. Gardes and D. J. Thomson, "Silicon Optical Modulators," *Nature Photon.*, vol. 4, pp. 518-526, 2010.
- [12] D. Petousi, L. Zimmermann, A. Gajda, M. Kroh, K. Voigt, G. Winzer, B. Tillack and K. Petermann, "Analysis of Optical and Electrical Tradeoffs of Traveling-Wave Depletion-Type Si Mach-Zehnder Modulators for High-Speed Operation," *IEEE J. Sel. Top. Quantum Electron.*, vol. 21, no. 4, 2015.
- [13] L. Chen, C. Doerr, R. Aroca, S. Y. Park, J. C. Geyer, T. Nielsen, C. Rasmussen and B. Mikkelsen, "Silicon Photonics for 100G-and-beyond Coherent Transmissions," in *Optical Fiber Communications Conference, Th1B1*, Anaheim, 2016.
- [14] A. Shastri, C. Muzio, M. Webster, G. Jeans, P. Metz, S. Sunder, B. Chattin, B. Dama and K. Shastri, "Ultra-Low-Power Single-Polarization QAM-16 Generation Without DAC Using a CMOS Photonics Based Segmented Modulator," *J. Lightw. Technol.*, vol. 33, no. 6, pp. 1255-1259, 2015.
- [15] B. E. A. Saleh and M. C. Teich, Fundamentals of Photonics, Hoboken: John Wiley & Sons, Inc., 1991.
- [16] H. Haug and S. W. Koch, Quantum Theory of the Optical and Electronic Properties of Semiconductors, Singapore: World Scientific, 2009.
- [17] H. Klein, Integrated InP Mach-Zehnder Modulators for 100 Gbit/s Ethernet Applications using QPSK Modulation, PhD Thesis, Berlin: Technische Universität, 2010.
- [18] A. Chen and E. J. Murphy, Broadband Optical Modulators, Boca Raton: CRC Press -

---

Taylor & Francis Group, 2012.

- [19] L. B. Soldano and E. C. M. Pennings, "Optical Multi-Mode Interference Devices Based on Self-Imaging: Principles and Applications," *J. Lightw. Technol.*, vol. 13, no. 4, pp. 615-627, 1995.
- [20] K.-O. Velthaus, M. Hamacher, M. Gruner, T. Brast, R. Keiser, K. Prosyk, I. Woods, D. Hoffmann and M. Schell, "High Performance InP-based Mach-Zehnder Modulators for 10 to 100 Gb/s Optical Fiber Transmission Systems," in *Conference on Indium Phosphide and Related Materials*, Berlin, 2011.
- [21] G. White and G. Chin, "Travelling Wave Electro-Optic Modulators," *Opt. Commun.*, vol. 5, no. 5, pp. 374-379, 1972.
- [22] I. Betty, M. G. Boudreau, R. A. Griffin and A. Feckes, "An Empirical Model for High Yield Manufacturing of 10Gb/s Negative Chirp InP Mach-Zehnder Modulators," in *Optical Fiber Communications Conference, OWE5*, Anaheim, 2005.
- [23] P. Bravetti, G. Ghislotti and S. Balsamo, "Chirp-Inducing Mechanisms in Mach-Zehnder Modulators and Their Effect on 10 Gb/s NRZ Transmission Studied Using Tunable-Chirp Single Drive Devices," *J. Lightw. Technol.*, vol. 22, no. 2, pp. 605-611, 2004.
- [24] J. P. Winzer and R.-J. Essiambre, "Advanced Optical Modulation Formats," *Proc. IEEE*, vol. 94, no. 5, pp. 952-985, 2006.
- [25] T. Baehr-Jones, R. Ding, Y. Liu, A. Ayazi, T. Pinguet, N. C. Harris, M. Streshinsky, P. Lee, Y. Zhang, A. Eu-Jin Lim, T.-Y. Liow, S. Hwee-Gee Teo, G.-Q. Lo and M. Hochberg, "Ultralow Drive Voltage Silicon Travelling-wave Modulator," *Opt. Express*, vol. 20, no. 11, pp. 12014-12020, 2012.
- [26] P. Rabiei, J. Ma, S. Khan, J. Chiles and S. Fathpour, "Heterogeneous Lithium-niobate Photonics on Silicon Substrates," *Opt. Express*, vol. 23, no. 21, pp. 25573-25581, 2013.
- [27] M. D. Gill, "Demonstration of a High Extinction Ratio Monolithic CMOS Integrated Nanophotonic Transmitter and 16 Gb/s Optical Link," *IEEE J. Sel. Top. Quantum*

- Electron.*, vol. 21, no. 4, 2015.
- [28] M. Seimetz, *High-Order Modulation for Optical Fiber Transmission*, Berlin: Springer, 2009.
- [29] R. G. Walker, "High-Speed III-V Semiconductor Intensity Modulators," *IEEE J. Sel. Top. Quantum Electron.*, vol. 27, no. 3, pp. 654-667, 1991.
- [30] M. Papuchon, C. Puech and A. Schnapper, "4-bits Digitally Driven Integrated Amplitude Modulator for Data Processing," *Electron. Lett.*, vol. 16, no. 4, pp. 142-144, 1980.
- [31] T. Kato, M. Sato, T. Yamase, K. Sato and H. Noguchi, "10-Gb/s - 80-km Operation of Full C-band InP MZ Modulator with Linear-accelerator-type Tiny in-line Centipede Electrode Structure Directly Driven by Logic IC of 90-nm CMOS Process," in *Optical Fiber Communications Conference, OThP4*, Los Angeles, 2011.
- [32] T. Yamase, M. Sato, H. Uchida, H. Noguchi, K. Sato and T. Kato, "10-Gb/s In-line Centipede Electrode InP MZM and Low-Power CMOS Driver with Quasi-Traveling Wave Generation," in *Opto-Electronics and Communications Conference, WK2\_3*, Taiwan, 2011.
- [33] X. Wu, B. Dama, P. Gothoskar, P. Metz, K. Shastri, S. Sunder, J. Van der Spiegel, Y. Wang, M. Webster and W. Wilson, "A 20Gb/s NRZ/PAM-4 1V Transmitter in 40nm CMOS Driving a Si-Photonic Modulator in 0.13 $\mu$ m CMOS," *ISSC*, pp. 128-129, 2013.
- [34] T. Yamase, M. Sato, H. Noguchi, K. Sato and T. Kato, "Low-Power Multi-level Modulation of InP MZM with In-line Centipede Structure Directly Driven by CMOS IC," in *Opto-Electronics and Communications Conference, Kyoto*, 2013.
- [35] M. Mazzini, M. Traverso, M. Webster, C. Muzio, S. Anderson, P. Sun, D. Siadat, D. Conti, A. Cervasio, S. Pfner, J. Stayt, M. Nyland, C. Togami, K. Yanushefski and T. Daugherty, "25GBaud PAM-4 Error Free Transmission over both Single Mode Fiber and Multimode Fiber in a QSFP form factor based on Silicon Photonics," in *Optical Fiber Communications Conference, Th5B.3*, Los Angeles, 2015.

- 
- [36] C. Xiong, D. Gill, J. Proesel, J. Orcutt, W. Haensch and W. M. J. Green, "A Monolithic 56 Gb/s CMOS Integrated Nanophotonic PAM-4 Transmitter," in *Optical Interconnects Conference, MC3*, San Diego, 2015.
- [37] C. F. Lam , H. Liu, B. Koley, X. Zhao, V. Kamalov and V. Gill, "Fiber Optic Communication Technologies: What's Needed for Datacenter Network Operations," *Communications Magazine*, vol. 48, no. 7, pp. 32-39, 2010.
- [38] S. Teotia, "Saddlepoint Approximation for Calculating Performance of Spectrum-Sliced WDM Systems," Digital Library and Archives, ETD@VT, 1999. [Online]. Available: <http://scholar.lib.vt.edu/theses/available/etd-080399-001630/>.
- [39] E. Jacobsen, "Pulse Shaping in Single-Carrier Communication Systems," DSP Related, 2008. [Online]. Available: <http://www.dsprelated.com/showarticle/60.php>.
- [40] M. S. John G. Proakis, Digital Communications, New York: McGraw-Hill, 2008, pp. 605-609.
- [41] J. R. Barry, E. A. Lee and D. G. Messerschmitt, Digital Communication, Boston: Springer Science, 2004.
- [42] N. Kikuchi and R. Hirai, "Intensity-Modulated / Direct-Detection (IM/DD) Nyquist Pulse-Amplitude Modulation (PAM) Signaling for 100-Gbit/s Optical Short-Reach Transmission," in *European Conference on Optical Communications, P.4.12*, Cannes, 2014.
- [43] R. Rudnick, A. Tolmachev, D. Sinefeld, O. Golani, S. Ben-Ezra, M. Nazarathy and D. M. Marom, "Sub-Banded/Single-Sub-Carrier Drop- Demux and Flexible Spectral Shaping with a Fine Resolution Photonic Processor," in *European Conference on Optical Communications, PD4-1*, Cannes, 2014.
- [44] L. Zhaung, C. Zhu, M. Burla, C. Roeloffzen, A. Leinse, B. Foo, B. Corcoran and A. Lowery, "Optical Generation of Nyquist spacing Super- Channel Using a Ring Resonator-Based Flat-Top Interleaver," in *European Conference on Optical Communications, We.1.6.4*,

Valencia, 2015.

- [45] B. A. Forouzan, *Data Communications and Networking*, New York: McGraw-Hill, 2007.
- [46] S. Ramo, J. R. Whinnery and T. Van Duzer, *Field and Waves in Communication Electronics*, Hoboken: John Wiley & Sons, Inc., 1994.
- [47] A. Agarwal and J. H. Lang, *Foundations of Analog and Digital Electronic Circuits*, San Francisco: Morgan Kaufmann Publishers, 2005.
- [48] K. Sahay and S. Pathak, *Basic Concepts of Electrical Engineering*, New Delhi: New Age International Publishers, 2006.
- [49] L. R. Boylestad, *Introductory Circuit Analysis*, Essex: Pearson New International Edition, 2014.
- [50] K. V. Cartwright, E. Joseph and E. J. Kaminsky, "Finding the Exact Maximum Impedance Resonant Frequency of a Practical Parallel Resonant Circuit without Calculus," *The Technology Interface International Journal*, vol. 11, no. 1, pp. 26-34, 2010.
- [51] J. Audet, "Q Calculation on L-C Circuits and Transmission Lines: A Unified Approach," *QEX*, pp. 43-51, Sep/Oct 2006.
- [52] J. R. Taylor, *An Introduction to Error Analysis: The Study of Uncertainties in Physical Measurements*, Sausalito: University Science Books, 1997.
- [53] G. Ghione, *Semiconductor Devices for High-Speed Optoelectronics*, Cambridge: University Press, 2009.
- [54] M. Pirola, F. Cappelluti, G. Giarola and G. Ghione, "Multisectional Modeling of High-Speed Electrooptic Modulators Integrated in a Microwave Circuit CAD Environment," *J. Lightw. Technol.*, vol. 21, no. 12, pp. 2989-2996, 2003.
- [55] K. De Mesel, *Spot-size converters for photonic integrated circuits*, Gent: Universiteit Gent, 2003.

- [56] J. Leuthold, R. Hess, J. Eckner, P. A. Besse and H. Melchior, "Spatial Mode Filters Realized with Multimode Interference Couplers," *Opt. Lett.*, vol. 21, no. 11, pp. 836-838, 1996.
- [57] "Coriant SMF28 Ultra datasheet," [Online]. Available: [http://www.corning.com/media/worldwide/coc/documents/Fiber/PI1424\\_11-14.pdf](http://www.corning.com/media/worldwide/coc/documents/Fiber/PI1424_11-14.pdf).
- [58] D. M. Pozar, *Microwave Engineering*, Hoboken: John Wiley & Sons, Inc., 2012.
- [59] I. García López, P. Rito, L. Zimmermann, D. Kissinger and A. C. Ulusoy, "A 40 Gbaud SiGe:C BiCMOS Driver for InP Segmented MZMs with Integrated DAC Functionality for PAM-16 Generation," in *International Microwave Symposium, Th3C-2*, San Francisco, 2016.
- [60] Y. Ehrlichmann, O. Amrani and S. Ruschin, "Photonic Digital-to-Analog Conversion and Digitally Driven Integrated Optics Modulator," in *International Conference on Microwaves, Communications, Antennas, and Electronic Systems*, Tel Aviv, 2011.